Topological internal control of the transport of colloidal particles and bipeds on non-periodic magnetic patterns

Von der Universität Bayreuth
zur Erlangung des Grades eines
Doktors der Naturwissenschaften (Dr. rer. nat.)
genehmigte Abhandlung

von

Farzaneh Farrokhzad

aus Yazd

1. Gutachter: Prof. Dr. Thomas Fischer

2. Gutachter: Prof. Dr. Werner Köhler

Tag der Einreichung: 10.12.2024

Tag des Kolloquiums: 29.04.2025

Topological internal control of the transport of colloidal particles and bipeds on non-periodic magnetic patterns

Von der Universität Bayreuth
zur Erlangung des Grades eines
Doktors der Naturwissenschaften (Dr. rer. nat.)
genehmigte Abhandlung

von

Farzaneh Farrokhzad

aus Yazd

1. Gutachter: Prof. Dr. Thomas Fischer

2. Gutachter: Prof. Dr. Werner Köhler

Tag der Einreichung: 10.12.2024

Tag des Kolloquiums: 29.04.2025

Abstract

This cumulative thesis is dedicated to the experimental study of the topological and drift transport of colloidal particles on top of non-periodic magnetic patterns. A promising approach to avoid disturbing effects of perturbations in a system, is using a topological protected transport. I will show in such system with topological protection, the transport is robust against perturbations. Magnetic particles can be transported above magnetic patterns using topologically protected transport. By applying a homogeneous external magnetic field that changes its direction along a loop, colloidal particles move on top of magnetic patterns. On top of periodic patterns one can transport all colloidal particles belonging to the same topological class along the same direction irrespective of their location on the pattern. I show how to move identical particles in different directions independently to perform different tasks using non-periodic patterns, in which the direction of the transport depends on the absolute position of the particles above the patterns. I will show which non-periodic patterns to use and which loops to apply to fulfill my desired tasks. By applying an external magnetic field, single colloidal particles self assemble into colloidal bipeds that are rods of different length formed by several single colloidal particles. I investigate how to use this control over single particles to synthesize bipeds in a specific location. In order to determine how much internal control I can have, I will show how to design a non-periodic pattern and modulation loop such that they work together in synergy to synthesize bipeds of a desired length. I will address the question how to use a single loop to give different commands to single colloidal particles and bipeds to do different tasks, simultaneously. Finally, I will show what kind of non-topological transport we can observe in superpositions of two magically twisted periodic patterns, by applying a drift force and a precessing external magnetic field.

Kurzdarstellung

Diese kumulative Arbeit widmet sich der experimentellen Untersuchung des topologischen und Drifttransports kolloidaler Partikel auf nichtperiodischen magnetischen Mustern. Ein vielversprechender Ansatz zur Vermeidung störender Effekte beim Transport ist es diesen topologisch zu schützen. Ich werde zeigen, dass topologisch geschützter Transport robust gegenüber Störungen ist. Magnetische Partikel können mithilfe eines topologisch geschützten Transports über magnetische Muster transportiert werden. Durch Anlegen eines homogenen externen Magnetfelds, das seine Richtung entlang einer Schleife ändert, bewegen sich kolloidale Partikel auf magnetischen Mustern. Auf periodischen Mustern können alle kolloidalen Partikel, die derselben topologischen Klasse angehören, entlang derselben Richtung transportiert werden, obwohl sie sich an verschiedenen Positionen befinden. Ich zeige, wie identische Partikel auf nichtperiodischen Mustern unabhängig voneinander in verschiedene Richtungen bewegt werden können, um dort unterschiedliche Aufgaben auszuführen. Die Richtung des Transports hängt dabei von der absoluten Position der Partikel über den Mustern ab. Ich werde zeigen, welche nichtperiodischen Muster zu verwenden sind und welche Schleifen anzuwenden sind, damit die kolloidalen Teilchen meine gewünschten Aufgaben erfüllen. Durch Anlegen eines externen Magnetfelds fügen sich einzelne kolloidale Partikel selbst zu kolloidalen Zweibeinern zusammen, die aus Stäben unterschiedlicher Länge bestehen, die aus mehreren einzelnen kolloidalen Partikeln bestehen. Ich untersuche, wie diese Kontrolle über einzelne Partikel genutzt werden kann, um Zweibeiner an einem bestimmten Ort zu synthetisieren. Um zu bestimmen, wie viel interne Kontrolle ich haben kann, werde ich zeigen, wie man ein nichtperiodisches Muster und eine Modulationsschleife so gestaltet, dass sie in Synergie zusammenarbeiten, um Zweibeiner einer gewünschten Länge zu synthetisieren. Ich werde die Frage behandeln, wie man eine einzelne Schleife verwendet, um einzelnen kolloidalen Partikeln und Zweibeinern verschiedene Befehle zu erteilen, damit sie gleichzeitig verschiedene Aufgaben ausführen. Abschließend werde ich zeigen, welche Art von nichttopologischem Transport wir in Überlagerungen zweier magisch verdrehter periodischer Muster beobachten können, indem wir eine Driftkraft und ein präzedierendes externes Magnetfeld anwenden.

Contents

Part I

Internal control of the transport of colloidal particles

Chapter 1

Introduction

Isn't it normal that if we give a certain command (here in the form of a loop of an external magnetic field) different magnetic particles would respond to such a command in a different way? All objects usually respond according to their material properties and if we continuously change this property from one particular magnetic object to the other, we would expect the response to be continuous as well. But it is not!! I can say that I can look at this issue from two perspectives. As a physicist and as a mother.
From the point of view of the physicist in me, this is a strange issue:
I am deeply accustomed to observing systems that respond continuously to changes in their governing parameters. The backbone of lots of classical and modern physics is formed by this continuous relationship. In many physical phenomena, small and incremental changes in a material property—such as temperature, force, or electric field—result in smooth and gradual changes in the system's behaviour. For example, thermal expansion could be a great example of a continuous response to changes in temperature [1]. As the temperature is increased, the material's dimensions increase smoothly which demonstrates a direct correlation between temperature and expansion. Or in elastic materials, the deformation is proportional to the applied force within the elastic limit, which is given by Hooke's Law [2]. As you continuously increase the force, the displacement increases continuously, reflecting a smooth, elastic response of the material.
But to be honest, as a mom, I am totally familiar with these surprises:
During the developmental stages that my daughter, Kiyana, passes through, I am experiencing different challenges in each stage. The development that I continuously try hard to improve, doesn't improve continuously with my effort. A lot of my effort seems in vain. During the stages of raising my daughter, from birth to one year old, I had challenges related to providing basic needs such as food, sleep and comfort, which suddenly changed completely after one year old. When Kiyana learned to walk and talk, she began to explore the world around her. I also had to increase my care and find a new way to communicate with my daughter while opening the way for her new experiences. Until she was

almost two years old, when I was happy that my efforts were paying off and I learned the right way of parenting. Again, all of a sudden, around the second year of her life, everything changed, and we entered a new phase of life. At the second year, Kiyana was finding herself, checking the boundaries and limits, and the world revolved around her needs. She had to do everything herself and we always heard the phrase "I do it myself". The need for social relations and visibility became stronger and I had to work harder to meet new needs, play games and make new connections. Unexpectedly, just when I thought there would be no more difficult challenges than this age, the age of three (which I call the age of opposing everything) started. So far, I think it was the most difficult and at the same time the most interesting stage. Kiyana had found herself; her demands were clear to her and it was not easy to disagree with her. Again, without warning, at this stage, we faced new obstacles to communicate with her and consider her new needs. We had to make more effort and adopted more complex and new methods.

In this project, I was able to combine these two experiences as a physicist and as a mother. In topology, a homotopy class is a family of continuous paths or functions that can be continuously transformed into one another [3]. Different homotopy classes represent fundamentally different paths that cannot be deformed smoothly into each other if there are "obstacles" in the space [4]. As a mother and a physicist, I can compare different homotopy classes with the different needs of a child at various ages. We can think of homotopy classes as representing the distinct stages or sets of needs that a child has as they grow. Each homotopy class corresponds to a family of needs or behaviors that cannot simply be transformed into another. During infancy, the primary needs of a child are basic survival needs: nourishment, sleep, and security. These needs are fundamental and non-negotiable, much like how a homotopy class that represents loops around a single, simple feature cannot change unless the underlying space changes drastically. At next stage (from 1 to 2), my daughter started to gain mobility, and suddenly from one to the next day could walk. This developmental step represents an expansion of the space the child can explore, similar to how a new homotopy class would expand to include more features. The loop that once only focused on basic survival needs now includes new points of interest, objects to touch, places to go or in another word a desire to explore and so on. By age three, her homotopy class now includes diverse "loops" that involve not just exploration, but also structured activities, peer relationships, and learning to manage emotions in more complicated ways.

In my project, I will show you, like Kiyana's growth, the response of colloids first does not change in any way with the change of the material properties and all those particles fall into the same homotopy class, robustly following the response of one representative of this class. Then suddenly without warning following a completely different response not continuously evolving from the response of the first class switching to the response of another second class of particles that again is followed by all particles continuously evolving from the particle after the switch. The response of a continuously increasing parameter of the particle is a step function with steps occurring between each set of particle properties. We might also be familiar with such non-trivial behaviour from measurements of the Hall resistivity of a quantum Hall effect material, where the transverse resistivity increases with the applied magnetic field in steps defined by natural constants h/e^2 completely independent of any material properties [5]. The quantum Hall effect has been explained by topological Chern classes [6].

Apart from that, I would love to know a unique rule that when I use it, everything works automatically and I won't have any problem in future raising my daughter or any of my future children of different ages. Do you think it is possible?

In my thesis I will show that I have found this rule for colloids. I will show how I use one driving loop to simultaneously and robustly enforce any wanted transport behaviour to each class individually. To gain this kind of control, I used inhomogeneous patterns to simultaneously induce the motion of different particles or bipeds (Colloidal rods formed from single colloids) in different locations. I will present variations of magnetic colloidal system letting the transport properties fall into topological classes. In chapter 2, I will explain topology and why transport properties are topological. I will explain how the topological properties of the driving loop directly translate to the topological properties of the particles transport. In chapter 3, I talk about internal control and I explain about position control in three different non-periodic patterns. I will show what is transcription space and how we can use different homotopy classes to have more control over transport. In the second part, I will show my publications and prior to those papers I briefly explain the questions behind them and the results. Finally, I talk about details of my setups in chapter 5 and in the end I will summarize the major finding.

Chapter 2

Defying Disruption: The Science of Topologically Protected Transport

I start this chapter by explaining briefly about topology and topological transport, as I believe to follow the subject it is important to be familiar with the concept of topological transport without repeating the papers. Although all of the details about the theory and formulas that we used exist in my publications. It is followed with the main questions that lead me to write this thesis. I show how I can have internal control in a colloidal system by controling the position and properties of the particles. This chapter is completed by a brief summary of how internal control works in my projects.

2.1 What is topology?

Stretch, Bend, but Never Break! [7] Topology is a mathematical field, describing properties of geometrical objects in space that are invariant under continuous deformations, such as stretching, bending or twisting without any breaks or tears. The number of holes, the genus, in an object is one of these topological invariants that remain unchanged if one smoothly deforms the object. In topology a coffee cup and a doughnut are topologically equivalent, because one can be deformed into the other without tearing or cutting (Fig. 2.1). Therefore, Objects with the same topological invariant are similar and belong to the same equivalence class [8].

Topology is also the field that connects local properties of differential manifolds with global properties [9]. Consider for example a smooth surface embedded into three dimensional Euclidian space. Choose a point on this surface and attach the tangent plane at this point. If the surface is curved in this point the

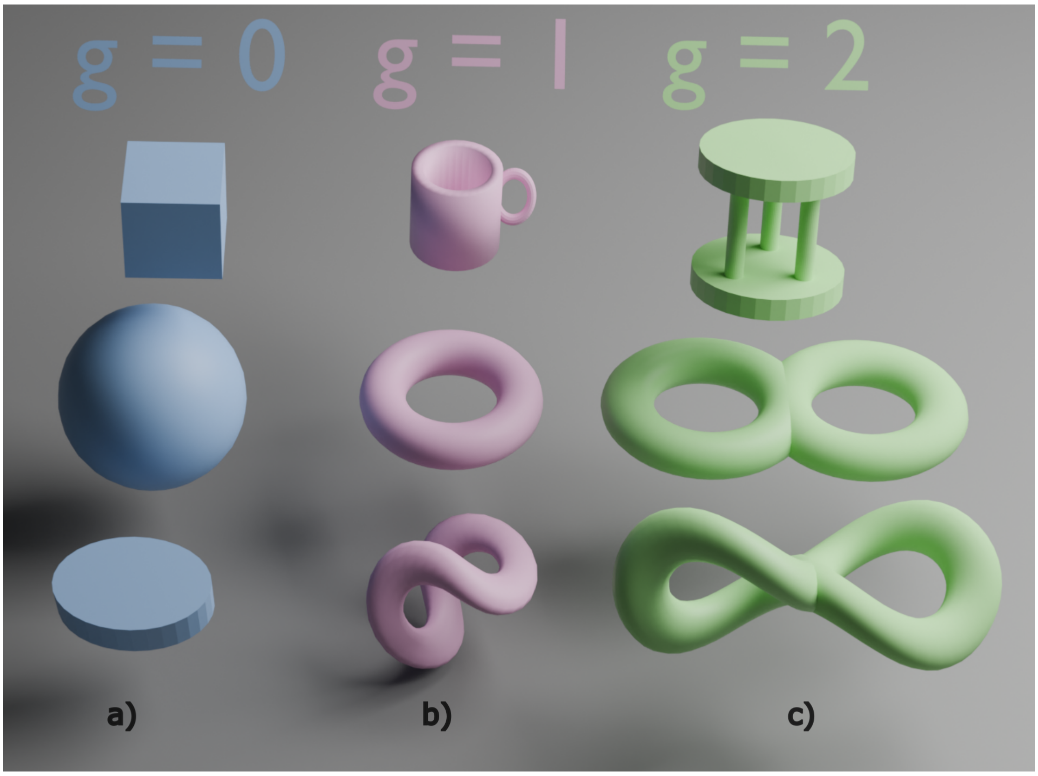

Figure 2.1: Objects with different genus. Surfaces with same colours are topologically equivalent. a) $g = 0$, b) $g = 1$, c) $g = 2$

infinitesimal surrounding on the surface will bend away from the tangent plane. We can mathematically describe the deviation of the tangent plane from the surface by a two-dimensional symmetric curvature tensor with eigenvalues κ_1 and κ_2, - the principal values of curvature. This description of a local property of the surface involves the embedded Euclidian space and therefore it is an extrinsic measurement of the property of a surface [10]. Gauss has shown that the product $K = \kappa_1 \kappa_2$, - the Gaussian curvature - is an intrinsic measure of the property of a surface that does not require an embedding space [11]. Take a flat piece of paper with $\kappa_1 = \kappa_2 = 0$ and bend it. This will change one of the principal curvatures, but not the second principal curvature which remains $\kappa_2 = 0$. The Gaussian curvature thus is invariant under how the paper is embedded into Euclidian space. An even more striking result occurs if we integrate the Gaussian curvature over the entire closed surface of the object. Gauss found that

$$\int_A K = 2\pi\chi \tag{2.1}$$

where χ is called the Euler characteristic of the surface. The Euler characteristic is an integer and it is directly related to the genus $g = (2 - \chi)/2$ that is also an integer and describes the number of holes in the surface [12]. We can smoothly deform the surface and locally change the Gaussian curvature - an intrinsic local property of the surface -, however when summed up over the surface the result is the same [13]. The genus of a surface is a robust quantity that defies disruption.

Figure 2.1 shows nine surfaces falling into three different equivalence classes, classified by the genus of the surface.

Lets put a one dimensional path on our different surfaces. Like for the surface we want the path to be closed, i.e. the path should start and end in the same point on the surface. We call such a path a loop. Lets try what we have learned about deformations of surfaces with our loop. We want to smoothly deform the loop in a way such that it stays embedded into the surface. On our surfaces of genus $g = 0$ it is always possible to shrink the loop to a point. This is not always true for loops living on a genus $g \neq 0$ surface [14]. We can classify the loops into homotopy classes. If a loop can be smoothly deformed into a point on the surface then it is said to be zero-homotopic. If not the loop encloses at least one of the holes of the surface, but notice that the hole is not part of the surface but part of the embedded space. In an intrinsic description of a surface the way to discover the existence of a hole is by looking for non-zero-homotopic loops [15]. We can shrink a non-zero-homotopic loop to a loop of

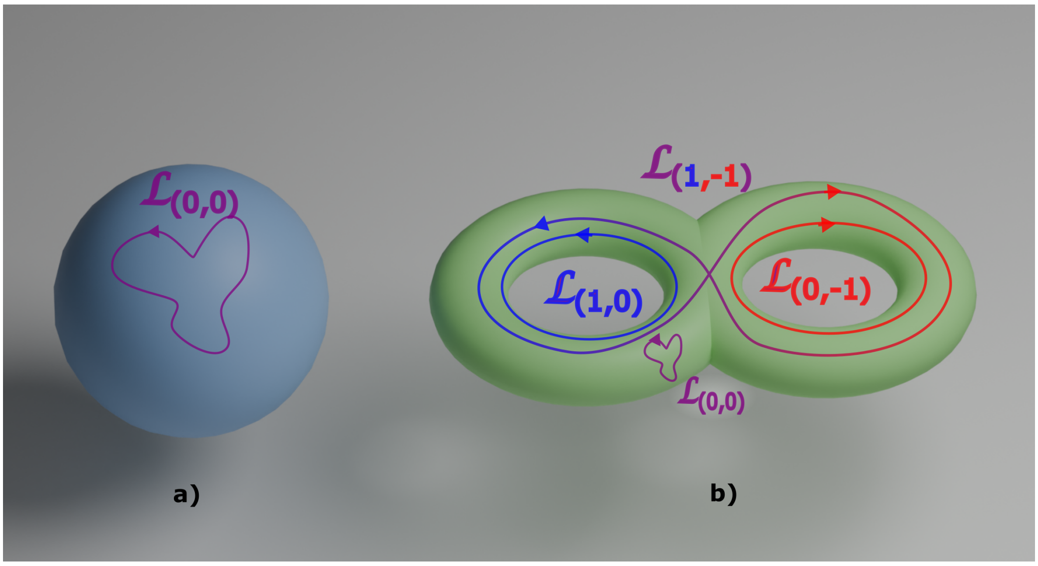

Figure 2.2: Loops on surfaces of different genus. a) A loop on a surface of genus $g = 0$ is always zero-homotopic. b) Different loops $\mathcal{L}_{(w_1,w_2)}$ with different winding numbers around the two holes.

minimal perimeter. It is blocked from shrinking further by the hole existing in the embedded space. We characterize non-zero-homotopic loops by the winding number of the loop around the g different holes. $w_1...w_g$. Again the winding numbers are topological invariants describing different equivalence classes of loops. A zero-homotopic loop is called topologically trivial and a non-zero-homotopic loop is called topologically non-trivial [16].

In Figure 2.2 we show two surfaces of genus $g = 0$ and $g = 2$ with a zero-homotopic loop on both surfaces and three non-trivial loops of winding numbers $w_1 = 1; w_2 = 0$, $w_1 = 0, w_2 = -1$, and $w_1 = 1, w_2 = -1$.

2.2 Why topology?

Repeatable and reliable control is necessary in a lot of systems. In many cases we can see how small deformations in these systems can alter a path. In such spaces, small changes can cause significant deviations, making the system sensitive to perturbations. One example could be the problem in quantum computation. Perturbations in quantum computing introduce lots of challenges, including decoherence and noise, all of which can affect the accuracy and reliability of quantum computations [17]. One promising way to face these challenges is using topological protection [18, 19].

Imagine I am walking with my daughter Kiyana on two different terrains: a flat, smooth path and a staircase. On the flat path, every step is continuous and uninterrupted. Small perturbations, like a slight change in direction, speed, or balance are immediately noticeable. If she slows down even slightly, her progress is visibly affected, and she may fall behind. My child needs to constantly adjust and keep up with the flow of movement on a flat path is analogous to navigating a space where small shifts impact the overall structure.

Now, contrast this with walking on stairs. In this case, the path is made by discrete and distinct steps. Here, small perturbations, like a brief pause or a small misstep have less of an effect. Even if she slides or shifts her weight, as long as she reaches the next step, her progress remains intact. Same as topologically robust systems that are protected from small changes, the stairs provide natural intervals that absorb minor variations [20]. In such systems, small perturbations do not change the fundamental structure, which allows the overall shape to remain in the same class. Walking on stairs, then, represents a system where the discrete nature of the steps ensures stability and robustness to small perturbations, in other words, the transport is topologically protected.

The physical properties that only depend on topological invariants are quite robust [21, 22]. That is, smooth perturbations do not change the topological quantity and therefore the physical quantity remains unchanged. The winding number around a hole of the mathematical manifold is one of the topological invariants of a curve on a manifold [23]. Hence, using the topological protection is a promising way to cover several problems in classical and quantum physics.

2.3 What is topologically protected transport in colloidal system?

As I mentioned before, the winding number is one of the topological invariants. The winding number plays a critical role in many real-world situations where the number of loops or turns an object makes around a point or another object fundamentally changes the outcome. Here, topological transport of the colloids on magnetic patterns can also be described by a set of winding numbers around special points [23, 24]. What are these special points? In my experiments, a pattern with up and down magnetization [25, 26] is exposed with an external magnetic field. All possible orientations of this external field is on a sphere named control space, $\mathcal{C}$. Our control space is not a sphere, but it is a punctured sphere. Which is from a topological point of view a very different object than a sphere. The control space has special points, the bifurcation points, that puncture the control space. The orientation of the external field varies in time, performing loops and to have topologically non-trivial protected transport, loops in control space must wind around these bifurcation points [23, 24, 27].

To transport magnetic colloids, a uniform time dependent external magnetic field of constant magnitude is superimposed to the non-uniform magnetic field generated by the pattern. The external magnetic field adiabatically (very slowly) follows a loop in control space. The particles are transported on a 2D plane parallel to the pattern, called action space $\mathcal{A}$, following the minima of the periodic colloidal potential. Different symmetry of the pattern leads to differently punctured control spaces, and different loops with different winding numbers can induce transport in different directions. The motion is topologically protected in the sense that the precise shape of the loop is irrelevant. All loops falling into the same class cause motion in the same direction, making the transport robust against internal and external perturbations.
The topologically protected transport displacement $\Delta \boldsymbol{r}(\mathcal{L})$ in action space caused by a loop $\mathcal{L}$ in control space can be summarized by the simple formula:

$$\Delta \boldsymbol{r}(\mathcal{L}) = \sum_i w_i(\mathcal{L}, \text{pattern}, \text{particle type})\, \boldsymbol{a}_i \tag{2.2}$$

where the w_i are the winding numbers around the bifurcation points and the $\boldsymbol{a}_i$ are the (local) lattice vectors of the pattern. This result was obtained already before starting my thesis [23, 24, 27]. However, the winding number is a topological invariant and one therefore expect it to be invariant or change by an integer upon deformations of either the loop, the pattern, or the colloidal particle. Previous theses have explored deformations of the loop and deforming the particle shape. In this thesis a major focus is put onto deformations of the pattern and its effect on the deformation of the other properties the winding number discontinuously depends on.

The symmetry of the pattern (e.g. square vs. hexagonal) and the particle properties (e.g. the length of colloidal bipeds) play important roles in determining the specific orientations of the external field that control the motion [23, 24, 27, 28]. I will introduce the properties of periodic patterns in section 2.3.1 and talk about the particle properties in section 2.3.2.

2.3.1 Topological transport of single colloidal particles on periodic patterns

Let us focus onto the pattern properties. In figure 2.3 I have shown a schematic overview of the transport of single colloidal particles above three periodic patterns with different symmetries. With each pattern I also show the control space with the location of the bifurcation points. Bifurcation points in control space are connected via fence segments that are also shown in figure 2.3. Fences separate regions with a different number of minima of the colloidal particles per unit cell of action space. The fences are also important because they determine whether the motion of the colloids is reversible or irreversible [24].

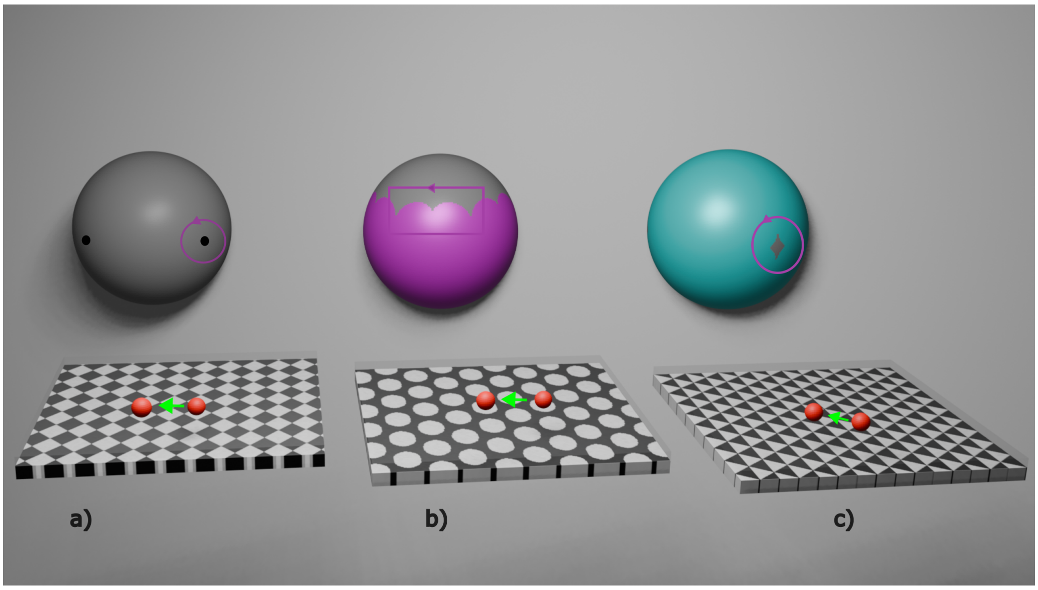

Figure 2.3: Schematic overview of control space $\mathcal{C}$ and action space $\mathcal{A}$ above three periodic patterns with different symmetries. The patterns are made of regions with up and down magnetization and are coated with a polymer coating as a spacer for the paramagnetic colloidal particles. Loops that wind around special orientations induce particle transport. These special orientations are determined by the position of the bifurcation points that are shown on control space for a) square pattern, in which the bifurcation points are four equidistant points on the equator and Hexagonal patterns with b) C_6 and c) S_6 symmetries.

2.3.2 Topological transport of colloidal bipeds

Let us now focus on the properties of our colloidal particles. Our colloidal particles are Dynabeads that are core shell particles of diameter $d = 2.8\mu$m and $d = 4.5\mu$m. The shell consists of polystyrene, and the core is filled with superparamagnetic nanoparticles made from magnetite and maghemite [29, 30]. Albeit one nanoparticle is superparamagnetic, the assembly of them inside the core makes the core paramagnetic such that the colloidal particle exhibits an induced magnetic moment when exposed to an external magnetic field. In external fields of the order of $H_{\text{ext}} \approx (1 - 4)$kA/m the resulting magnetic moments are large enough to cause sufficient dipolar interactions between nearby Dynabeads such that they assemble into dumbbells ($H_{\text{ext}} \approx (0.1 - 0.8)$kA/m) or into colloidal rods ($H_{\text{ext}} \approx (1 - 4)$kA/m) consisting of $n = 2 - 7$ Dynabeads with the rod oriented along the external field [31, 32]. In Figure 2.4a we depict a microscope image of Dynabeads on a periodic square pattern subject to an external field $\boldsymbol{H}_{\text{ext}}$ that is tilted at an angle of $\cos\vartheta = \boldsymbol{n} \cdot \boldsymbol{H}_{\text{ext}} = 0.7$ to the pattern normal vector $\boldsymbol{n}$. There are rods of different length, with the elevated Dynabeads being out of focus and the grounding Dynabead being in focus. In my publications I made those rods walk and I call them bipeds for this reason. In the scheme Figure 2.4b I show a perspective view of different bipeds on the square pattern.

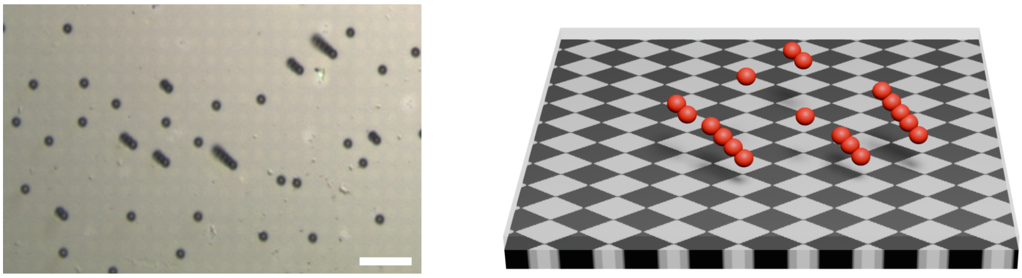

a) **b)**

Figure 2.4: Colloidal single particles and bipeds. a) Microscope image of colloidal bipeds above a square magnetic pattern and subject to an external field. Scale bar is 20μm. b) Scheme showing a perspective view of bipeds on a square pattern.

Now that I have introduced the concept of topological transport, I talk about the main achievements of my project, **internal control**.

Chapter 3

Internal control

Do you remember that I was looking for a unique rule to use and stay a side watching how everything works perfectly? In both of my roles: as a mother and as a physicist. I want Kiyana to learn something. Therefore I send her to kindergarden. She there learns to sing and If she makes a mistake the teacher will correct her. Eventually I want Kiyana to correct herself. The corrections of the teacher are external. The teacher must deviate from what he planned initially to give Kiyana the correcting feedback. Once Kiyana can correct herself no deviation from the teacher is necessary anymore. Kiyana has internal control and can correct her mistakes without external interference.

My thesis is about the topological control of colloids. There exist much simpler techniques in externally controlling the motion of colloids using for example optical tweezers. We grab a colloidal particle with the tweezers at position A and move it toward a position B [33]. However, if something goes wrong and a colloidal particle for some reason is lost while being transported by the tweezers one needs to detect the mistake via microscopic observation and correct the tweezers path to recapture the colloid. The colloid does not internally realize that it has been lost by the tweezers and does not catch up with the tweezers by itself [34, 35].

In my thesis I will present a much more complex task that I will accomplish using topological protection ensuring an internal quality control in achieving the task. The control loop will be complex, however, I do not need to change it if something goes wrong during the process of fulfilling the task. The colloids will do that by themselves.

In this chapter I will talk about different kind of control that I was looking for in my project. I give a brief overview in section 3.1 about how to achieve position control by using non-periodic patterns and in section 3.2 I show how to achieve individual control over the motion of bipeds with different length. Both types of control provides you with the major ingredients needed to simultaneously but independently control the motion of bipeds of various length at different positions on the non-periodic pattern. The exact recipe for achieving each task can only be given once you know how the bifurcation points and the fences depend on both the position and the length of the bipeds. This information will be provided in my three publications.

3.1 Position control with non-periodic patterns

When I started working with colloids, I was wondering how much control I can have on colloids. Can I tell them where to go? Well, we had the answer in equation (2.2), that I showed in section 2.3.
Is it possible to tell similar particles move in different directions? That was a good question that helped me to reach here and write this thesis. Equation (2.2) tells me the two things that play an important role in the motion are symmetry of the pattern and particle properties. In our previous papers we know how to transport particles on periodic patterns with different symmetries [23, 24, 27, 28]. In each symmetry we have differently punctured control spaces and by using the proper loop winding around the proper points we will have non-trivial transport.

What will help me to find a way to move similar colloids in different directions? what if I alter the periodicity of the pattern? Using various non-periodic patterns was one of the solutions. But how?

In sections 3.1.1 and 3.1.2 I talk about the properties of two different non-periodic patterns that I used in publication 1 and 2 in order to topologically control the position of the colloids. In section 3.1.3 I show how I can control the motion of the colloids on top of a twisted magnetic pattern, but without the help of topology.

3.1.1 Topological defect patterns

Imagine a missing piece in a puzzle or a wrinkle in a piece of fabric, these types of defects can be fixed without fundamentally changing the system. Now, imagine trying to remove a knot from a rope. It doesn't matter how much you stretch or pull the rope, the knot persists unless you cut through it. Conventional

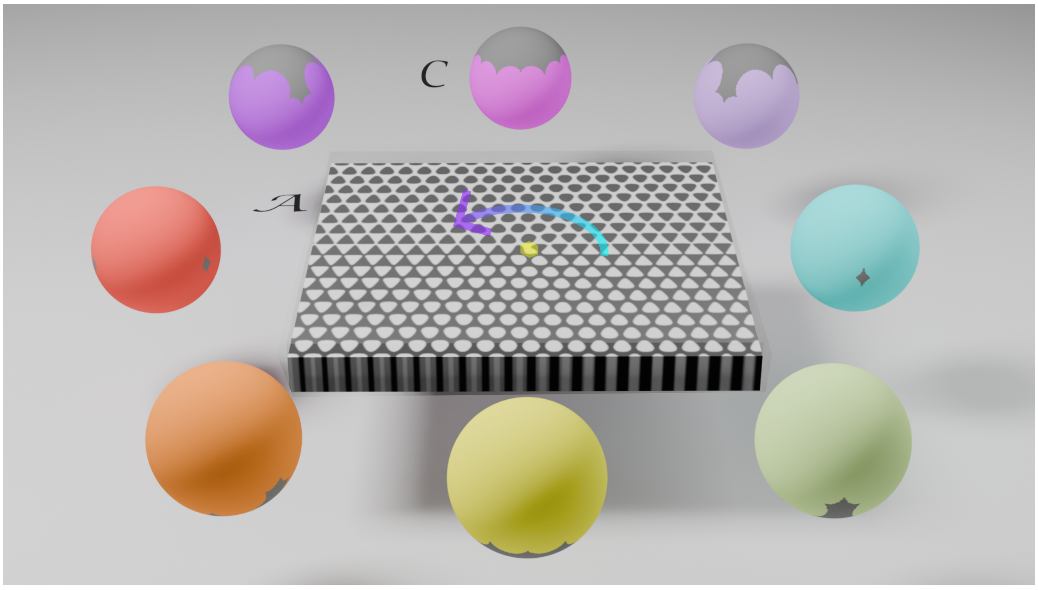

Figure 3.1: A magnetic pattern with a topological defect in the centre (shown in yellow). The symmetry phase is constant along radial directions and varies in the azimuthal direction. To each radial sector having one symmetry phase I plot the corresponding control space near. If we look at it from magenta sphere to yellow the symmetry phase change from C_6 to S_6 to $\bar{C}_6$. In the gray area of control space there are two minima of the colloidal potential per unit cell. In the colored area there is only one minimum of the colloidal potential per unit cell. Both areas are separated by the fence. The cusps of the fences are the bifurcation points. Bifurcation points of different colored control spaces are in different positions. A loop common to all of the control spaces thus will have different sets of winding numbers which according to equation (2.2) will lead to different transport displacements of the colloids.

defects can be smoothed out with a little 'material engineering', but topological defects resist to gentle fixes [36]. In my first publication, I used non-periodic threefold pattern with a topological defect at the centre shown in figure 3.1, which we call spiral pattern. In three-fold patterns $N = 3$ the symmetry and one additional parameter, the symmetry phase φ, determine the magnetic pattern and therefore the position of the bifurcation points. As you can see in figure 2.3, in the spiral pattern the symmetry phase and therefore the shape of the black domains varies with the positions. For each symmetry phase I have bifurcation points in different position of control space. Therefore, by winding around a family of bifurcation points simultaneously I could transport each particle depending on their location in a spiral trajectory to reach the defect and vice versa [37].

3.1.2 Metamorphic pattern

Quasicrystals obliterate the line between order and disorder. They have highly ordered structures in small regions, like conventional crystals. But globally, their structure never repeats periodically [38]. If you only observe a small section in a locally periodic system, the arrangement of elements looks like it might repeat. However, the overall structure is aperiodic if you zoomed out to a larger view, which means it never exactly repeats across the entire system. What makes quasicrystals fascinating is this balance between local periodicity and global aperiodicity, offering part of the simplicity of crystalline order without the restrictions of periodicity. In my second paper, I used a non-periodic three-fold pattern without topological defect but a metamorphic pattern. Just as quasicrystals defy conventional expectations by having both symmetry and aperiodicity, metamorphic magnetic patterns exhibit a similar behaviour.

In the metamorphic pattern, shown in figure 3.2, if we move along the x-direction, the lattice morphs from the $\bar{C}_6$ locally periodic pattern into an S_6 symmetric pattern and then to a local C_6-symmetry. Therefore, like in the spiral pattern, the symmetry phase changes with the location on the metamorphic pattern. As the symmetry phase changes, the position of the bifurcation points in control space are also changed for each symmetry phase. Hence, by winding around different bifurcation points I am able to transport particles in different locations in different directions simultaneously [39].

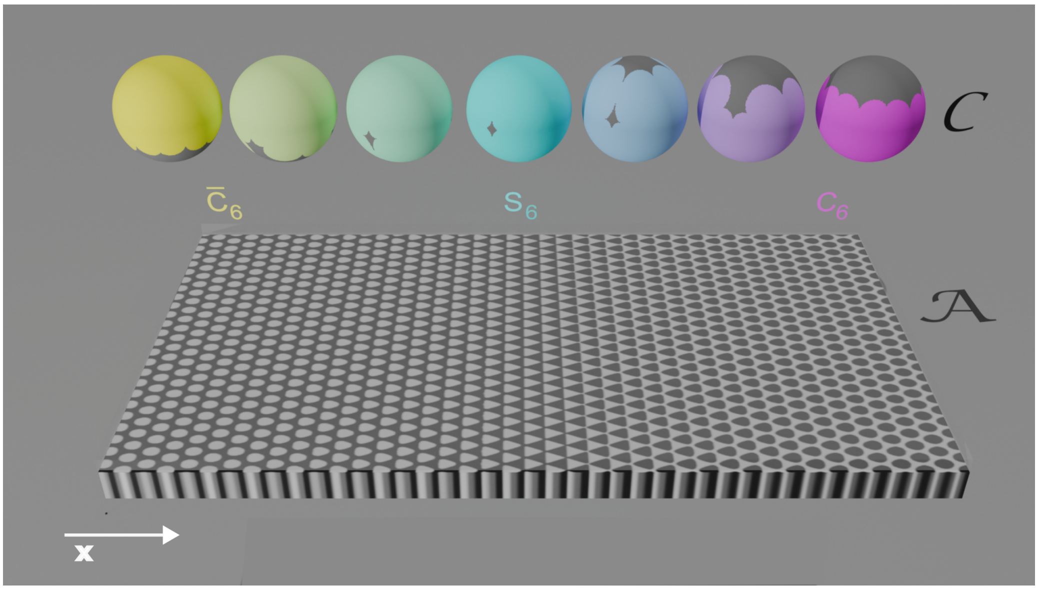

Figure 3.2: Metamorphic pattern with corresponding control spaces for each symmetry phase from C_6 to S_6 to $\bar{C}_6$. The different colored control spaces are the same as those of Figure 3.1

In both the topological defect pattern in Fig. 3.1 as well as in the metamorphic pattern of Fig. 3.2 the symmetry phase changes with the location on the pattern, therefore the position of the fences and bifurcation points in control space that we should wind around differs. Now if I have similar particles in different locations of the pattern, by applying one external magnetic loop each particle, depending on their location, knows where to go. Perfect! That´s what I was looking for. In this thesis, I will use the concept of local periodicity in non-periodic patterns to overcome the limitations of the periodic patterns and control the movements of similar particles in different locations.

3.1.3 Twisted magnetic pattern

The unconventional properties of twisted bilayer graphene are one of the most exciting recent discoveries in condensed matter physics. Twisted bilayer graphene is obtained when two layers of graphene, sheets of carbon atoms arranged in a hexagonal lattice, are stacked on top of each other and twisted at a specific angle (known as the ”magic angle” and it is particularly at around 1.1 degrees). This new structure fundamentally alters how electrons behave in

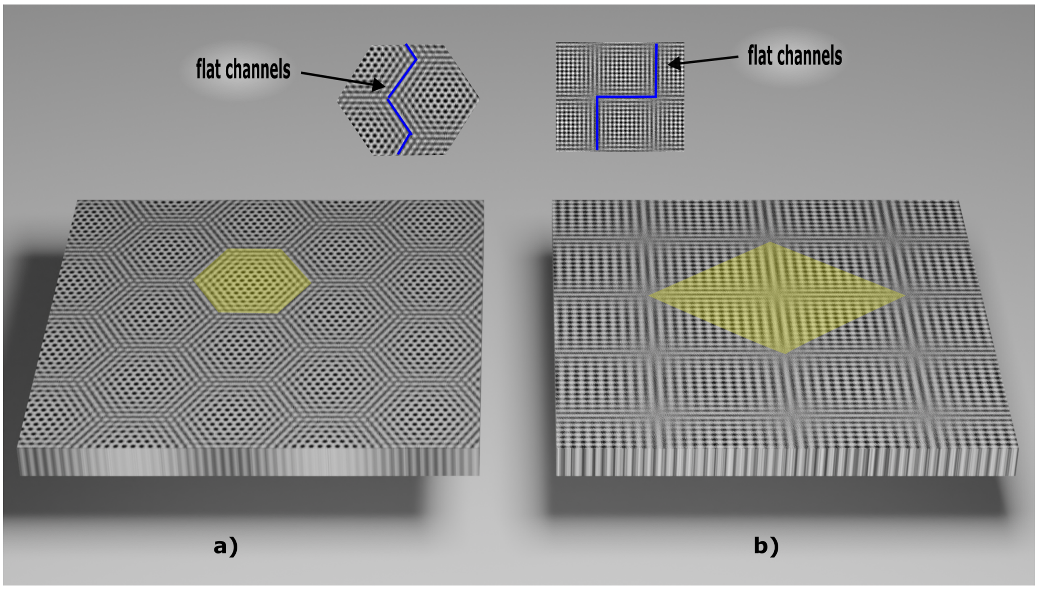

Figure 3.3: Twisted magnetic patterns. a) Hexagonal twisted pattern b) Square twisted pattern. The yellow regions are one twisted Wigner Seitz cell. Note that the twisted Wigner Seitz cells are rotated with respect to the Wigner Seitz cell of one of the single patterns. The blue lines indicate the locations of the non-generic flat channels.

the system [40]. This specific twist creates a moiré pattern, which leads to the formation of a superlattice, a periodic potential due to the interference of the two hexagonal lattices [41, 42]. This twisted bilayer graphene exhibit new and unexpected properties, such as superconductivity [43].

Similar to twisted bilayer graphene, in colloidal system, imagine two identical magnetic periodic patterns. If they are perfectly aligned, the magnetic potential is periodic with the period of the individual patterns. If we rotate one of these magnetic patterns slightly with respect to the other, the generated magnetic field between them changes, resulting in a magnetic field patterns with a period much larger than the period of an individual pattern [44]. Imagine two pieces of graph paper and lay one on top of the other. if they are perfectly aligned, everything looks neat. However, if you rotate one slightly, you'll see a complex pattern emerge and you get a new pattern that didn't exist in either grid alone. This happens because the small, regular spacing in the grids interferes with each other, producing a new, larger-scale pattern. The square and hexagonal twisted pattern are shown in Fig 3.3. In Fig 3.3 you will see that the interference of the two patterns causes a structure that resembles the original pattern in generic locations. There are however non-generic cells of negative interference connected along a zig-zag path that we call the flat channel (blue lines in Fig 3.3). A flat channel causes a colloidal potential that is flat along the channel and this is the reason of its name. The even less generic cells are at the zig-zag corners of the flat channel [45, 46].

As I wanted to do experiments with colloids in microscopic setup, it was not possible to use two patterns and rotate them. Therefore, one pattern is made in a way that shows an overlay of the potential of two twisted square or hexagonal patterns [47].

By using these patterns I was also able to control the motion of single colloids and colloidal rods, but without using topology. In my experiments on twisted moiré patterns I used gravity to drive the high density colloids through the pattern. I therefore mounted the setup, consisting of the microscope, the coils and the sample on an inclined plane. In a specific regime of the inclination angle of the inclined plane and specific regime of magnetic field strengths, I could confine the motion of the particles to the flat channels while colloids in generic locations are stuck in their cells. The transport behavior of single colloidal particles and colloidal dumbbells is the subject of my third publication.

3.2 Length control of colloidal bipeds

As I told you two important things in transporting the particles are symmetry of the pattern and particle properties. I have shown in section 2.3.2 that if the dipolar interaction of the single colloids is strong they assemble to make bipeds with different lengths. Albeit the length of a biped is quantized in multiples of a single colloidal particle diameter it can be useful to consider the length of the biped a quantity that (theoretically) could be changed continuously. During the preparation of my sample I will obtain bipeds with random length in a random position. In my second paper I showed, now that I can control similar particles in different locations of the pattern by using a non-periodic pattern, I can command single colloids to move toward an active line, i.e. a line of specific local pattern symmetry, and accumulate so many single colloids in this region such dipolar interaction assembles them into bipeds there. Of course, ”It's easy once you know the answer.” That was a big step for me and therefore the probability to get biped in that line was much higher than in other places. How can I command a biped to stop growing, leave the active line into an escape direction? The answer to this question requires me to know the position of the bifurcation points at each position of the non-periodic pattern for all different biped lengths. To understand this dependence it is useful to introduce a new space, the transcription space.

3.2.1 Homotopy classes and transcription space

Next important question that helped me to reach here is: Now that I have bipeds where I want, can I also control the lengths of them? Is it possible to make a factory for bipeds? For example, if I need a biped with only four particles can it survive before getting other particles and making longer bipeds? In this case I needed to know how the special points work for bipeds and what are homotopy classes in topology. Well, probably now you are familiar with these concepts. As discussed before, for single colloids the set of all possible orientations of $\boldsymbol{H}_{\text{ext}}$ forms a spherical surface called control space. For different symmetries, the position of the fences in control space is different and hence the modulation loop that is needed to transport particles in different positions is also different.

For bipeds, instead of control space we introduce transcription space. Let $\boldsymbol{b}_n$ denote the vector from the northern foot to the southern foot of a biped of length b_n [28]. The orientation of the (dipolar) biped is locked to that of the external field. Now we can define transcription spaces given by the surface of a sphere of radius b_n. Each point on transcription space corresponds to an orientation of a biped of length b_n. Great! Each length has different sphere. Therefore, if we have two bipeds that have different lengths and at least one length is larger than the lattice constant, they fall into different homotopy classes. Now you can imagine why I was talking about my daughter's growth and compare it with homotopy classes in introduction. Going back to the issue of length control, now that we are familiar with homotopy classes, I can use different loops for each length. Hence, for these bipeds we can find loops in $\mathcal{C}$ that is transcipted into two loops and we can transport them independently.

3.3 Conclusions

In this chapter I started with the question of internal control that lead to my thesis. In my experiments I was looking to have internal position control on colloids and bipeds and also internal length control for bipeds.

In order to have position control in my experiments, I used patterns with three fold symmetry but non-periodic. In the metamorphic pattern of section 3.1.2 and in the topological defect pattern 3.1.1 the symmetry phase changed as a function of the position on the pattern. Therefore, the bifurcation points for each symmetry phase are located in different positions of control space and by winding around each of the bifurcation points, we can have transport in different directions at different positions of action space simultaneously.

For example, in publication 1, when I put colloids on top of the topological defect pattern by applying a single magnetic loop that winds around special bifurcation points simultaneously, I am able to let the particles follow a spiral path into the topological defect irrespective of the particles initial position.

Another form of position control is achieved in my publication 3, where I am able to confine the non-topological transport of single colloidal particles and bipeds to a non generic region - the flat channels - of a twisted hexagonal or square pattern.

On the other hand, in order to have length control, I showed how different homotopy classes work. In publication 2, I have similar colloidal particles in different locations. After applying a single loop, singlets and bipeds interpret this loop differently. As bipeds with different lengths can be considered as different particles, the homotopy class and therefore the bifurcation points change with the length. Single colloids move toward the active line where they assemble into bipeds and then when the assembled biped is long enough it walks away from the active line. In this way single colloidal particles are sent to the active line and bipeds of a chosen length are emitted from the active line creating a programmable biped factory for bipeds of a specific length.

If I am the one to talk about the beauty of my project, I would say it the internal control of the whole system. I applied a single external magnetic loop and that's it! Each translate the loop differently and respond to it depending on their properties. Thats what I mean by internal control. Everything works perfectly without any external interference.

Chapter 4

Overview of the publications

4.1 Simultaneous and independent topological control of identical microparticles in non-periodic energy landscapes

In this work, I showed by using inhomogeneous patterns and simple loops or simple patterns and complex loops it is possible to control the movement of identical colloidal particles in different directions at different positions.

As I discussed in section 3.1.1, one can construct complex patterns by locally changing the symmetry phase in an originally three-fold symmetric periodic pattern. In the first part of the paper, I used patterns with a topological defect made by changing the symmetry phase. The symmetry phase varies between $\varphi = -\pi/3$ and $\pi/3$. Particles in random initial positions can be guided toward the center of the topological defect by repeating a simple loop. A slight change of the loop can change the trajectory in a way such that instead of attracting the particles the topological defect acts as a repeller. I used a more complex pattern to show that particles can follow a more complicated trajectory. I used a pattern, in which the symmetry is changed locally, such that randomly initialized particles on the pattern follow a trajectory to write the letter "*B*".

In the second part of the paper, I showed this position control is also possible with simple periodic patterns but more complex loops. I used simple square patterns which with different orientation relative to the same applied loop. because the positions of the bifurcation points depend on the rotation angle by applying the same loop, particle trajectories on four differently oriented square patterns write the letters "*A*", "*B*", "*C*" and "*D*". Thus, I can choose loops that control the motion of particles in each pattern independently and simultaneously. In the last approach, I used complex pattern together with complex loops. I first used three topological defect patterns to move randomly initialised particles to their defect center and in a second step the loop transfers the particle from the three defect centers to three square patterns with different orientation. In a third step depending on the orientation of the square patterns, the particles either draw a square-, or a triangle- or a cross-trajectory on the three patterns.

In this project, I showed how much precise control I can have on single colloids with three different approaches.

4.2 Topologically controlled synthesis of active colloidal bipeds

In publication 2 2, I used the metamorphic pattern of section 3.1.2 which is a quasi-periodic pattern with symmetry phase that continuously changes as one moves along the pattern. In this work I show the ability of the internal control. I used a single loop consisting of two parts, an entry- and an exit-loop. Single colloidal particles and bipeds interpret the external magnetic loop differently. With a properly designed loop, single colloidal particles located in different positions are all transported toward one active line. This increases the density of colloids at the active line and the reaction rate of an addition reaction of two colloids or bipeds to a larger biped leads to a growth of single colloids toward longer and longer bipeds. The exit loop terminates the growth at our desired length and bipeds of the desired length are emitted from the active line. I apply six differently programmed loops to produce bipeds of the six different desired lengths $b_2 - b_7$.
I therefore designed a programmable and topologically protected lab on a chip capable to produce bipeds of any length.

4.3 Magnetic colloidal single particles and dumbbells on a tilted washboard moiré pattern in a precessing external field

In this work I studied different transport modes of colloidal particles and dumbbells on a square- and on a hexagonal magnetic moiré pattern. The pattern is inclined with respect to gravity and the single particles are driven through the pattern using gravity. An additional precessing external magnetic field exerts a magnetic torque onto the dumbbells. In the moiré pattern we can distinguish generic from non generic locations. The non generic locations form a zig-zag shaped flat channel. At sufficient external field strength the motion of the particles can be confined to these flat channels. We demonstrate one transport mode that ignores the difference between generic and non generic locations, two different modes of transport through the flat channels, as well as two non-transport modes where the single colloidal particles and dumbbells are localized.

Part II

Publications

Publication 1

Simultaneous and independent topological control of identical microparticles in nonperiodic energy landscapes

Nature Communications, 14, 7517 (2023)

Nico C. X. Stuhlmüller[a2], **Farzaneh Farrokhzad**[a1], Piotr Kuświk[b], Feliks Stobiecki[b], Maciej Urbaniak[b], Sapida Akhundzada[c], Arno Ehresmann[c], Thomas M. Fischer[a1], and Daniel de las Heras[a2]

[a1] Experimental Physics X and [a2] Theoretical Physics II, Department of Physics, University of Bayreuth, 95447 Bayreuth, Germany.
[b] Institute of Molecular Physics, Polish Academy of Sciences, 60-179 Poznań, Poland.
[c] Institure of Physics and Center for Interdisciplinary Nanostructure Science and Technology (CINSaT), University of Kassel, Germany.

This paper shows the individual and simultaneous topological transport of identical colloidal particles at different positions on the pattern.

My Contribution

Nico C. X. Stuhlmüller designed the modulation loops and performed the simulations. I performed the experiments. Nico C. X. Stuhlmüller, I, Thomas Fischer and Daniel de las Heras conceptualized the research. Piotr Kuświk, Maciej Urbaniak, and Feliks Stobiecki produced the magnetic film. Sapida Akhundzada, and Arno Ehresmann performed the fabrication of the micromagnetic domain patterns within the magnetic thin film. Nico C. X. Stuhlmüller, I, Thomas Fischer and Daniel de las Heras designed the patterns and wrote the manuscript. All authors including me contributed to the different revision stages of the manuscript.

nature communications

Article

https://doi.org/10.1038/s41467-023-43390-0

Simultaneous and independent topological control of identical microparticles in non-periodic energy landscapes

Received: 20 June 2023

Accepted: 7 November 2023

Published online: 18 November 2023

Check for updates

Nico C. X. Stuhlmüller[1], Farzaneh Farrokhzad[2], Piotr Kuświk[3], Feliks Stobiecki[3], Maciej Urbaniak[3], Sapida Akhundzada[4], Arno Ehresmann[4], Thomas M. Fischer[2] & Daniel de las Heras[1]

Topological protection ensures stability of information and particle transport against perturbations. We explore experimentally and computationally the topologically protected transport of magnetic colloids above spatially inhomogeneous magnetic patterns, revealing that transport complexity can be encoded in both the driving loop and the pattern. Complex patterns support intricate transport modes when the microparticles are subjected to simple time-periodic loops of a uniform magnetic field. We design a pattern featuring a topological defect that functions as an attractor or a repeller of microparticles, as well as a pattern that directs microparticles along a prescribed complex trajectory. Using simple patterns and complex loops, we simultaneously and independently control the motion of several identical microparticles differing only in their positions above the pattern. Combining complex patterns and complex loops we transport microparticles from unknown locations to predefined positions and then force them to follow arbitrarily complex trajectories concurrently. Our findings pave the way for new avenues in transport control and dynamic self-assembly in colloidal science.

The transport of microscopic colloidal particles suspended in fluids is relevant for a wide range of physical and biological phenomena including sedimentation[1], drug delivery[2–4], self-assembly[5–7], microfluidic devices[8–13], and active systems[14–16]. External fields are often used to control the motion of colloidal particles[17–19]. These include spatially uniform fields such as gravitational[20], electric[21], and magnetic[22–24] fields, as well as spatially inhomogeneous fields such as the manipulation of colloidal particles with optical tweezers[25]. Directed colloidal transport can be achieved via Brownian motors[26–28] that combine non-equilibrium fluctuations with spatially inhomogeneous energy landscapes[29–31].

Usually, the colloidal particles are transported along the same direction but the simultaneous transport of different particles across different directions is useful and even a requisite in systems of various length scales. For example, the transport of cargo on traffic networks requires organizing various subtasks simultaneously[32]. Sorting of microparticles driven on periodic lattices is possible because the particles travel along different directions depending on, e.g. their size[33–36]. In biology, the metabolism and structural diversity of the cell demand the regulation of a vast array of molecular traffic across intracellular and extracellular membranes.

In previous work, we have shown that robust, multidirectional, and simultaneous control of colloidal particles that differ in, e.g. their magnetic properties can be achieved with topological protection[37,38]. As illustrated in Fig. 1a, paramagnetic particles are placed above a

[1]Theoretische Physik II, Physikalisches Institut, Universität Bayreuth, D-95440 Bayreuth, Germany. [2]Experimatalphysik X, Physikalisches Institut, Universität Bayreuth, D-95440 Bayreuth, Germany. [3]Institute of Molecular Physics, Polish Academy of Sciences, 60-179 Poznań, Poland. [4]Institute of Physics and Center for Interdisciplinary Nanostructure Science and Technology (CINSaT), University of Kassel, D-34132 Kassel, Germany.
e-mail: delasheras.daniel@gmail.com

periodic magnetic pattern made of regions of positive and negative magnetizations normal to the pattern. A uniform external magnetic field of varying orientation drives the motion. The particles are transported following the minima of the periodic magnetic potential which results from the interplay between the complex but static field of the pattern and the simple but time-dependent uniform external field. The orientation of the magnetic field varies in time-performing loops. Hence, after one loop the orientation returns to its initial value. Loops that wind around specific orientations induce the transport of the colloidal particles by one unit cell of the magnetic pattern. During the loop, minima of the magnetic potential cross from one unit cell to the adjacent. Once the loop ends, the particle is in a position equivalent to the initial one but in a different unit cell. The motion is topologically protected in the sense that the precise shape of the loop is irrelevant. Only the set of winding numbers of the modulation loop around the specific orientations (the topological invariant) determines the transport direction. The motion is therefore robust against perturbations.

The specific orientations of the external field that are relevant to control the motion depend on both the symmetry of the pattern[37] (e.g. square vs. hexagonal) and the particle properties. Hence, particles with different properties, e.g. paramagnetic and diamagnetic particles above hexagonal magnetic patterns[39] as well as micro-rods of different lengths[38], can be transported in different directions independently and simultaneously using periodic patterns. However, the use of periodic patterns imposes several limitations on the transport. All particles that belong to the same topological class (e.g. identical paramagnetic particles or rods of the same length) are transported along the same direction, independently of their absolute position above the pattern as schematically represented in Fig. 1a. In addition, the location of the particles above the pattern is unknown a priori and it must be determined externally via, e.g. direct visualization via microscopy.

These limitations are overcome here using inhomogeneous (non-periodic) patterns. We make either the symmetry, Fig. 1b, or the global orientation, Fig. 1c, of the magnetic pattern dependent on the absolute position above the pattern. As a result, the specific orientations of the external field that control the motion depend also on the space coordinate. The direction of the transport can then be locally controlled by the modulation loop of the external field and also via the local symmetry of the inhomogeneous magnetic pattern. We can imprint the complexity of the transport mainly to the pattern, and then use simple loops to generate complex transport as illustrated in Fig. 1b. Following this idea we create non-periodic patterns that transport the particles to a desired position by just repeating simple modulation loops. We also create patterns in which the colloidal particles follow arbitrarily complex trajectories driven by a simple time-periodic modulation loop. Additionally, we create simple patterns and encode the complexity of the transport in the modulation loops as sketched in Fig. 1c. This allows us to simultaneously and independently control the transport of identical colloidal particles located at different positions above the pattern. We design for example a complex modulation loop that controls the transport of 18 identical colloidal particles individually and simultaneously. Beyond its fundamental interest, our work opens a new route to control the transport in colloidal systems with potential applications in reconfigurable self-assembly[40–43].

Results

The plane in which the particles move (action space) splits into allowed and forbidden regions. In the allowed (forbidden) regions the stationary points of the magnetic potential are minima (saddle points). The boundaries between allowed and forbidden regions in action space are the fences. The position of the fences in control space $\mathcal{C}$ (a sphere that represents all possible orientations of the external field) depends on the symmetry of the pattern and it determines the loops that induce colloidal transport (see Fig. 1). An extended summary of the transport in periodic patterns[37] is provided in Supplementary Note 1 and Supplementary Figs. 1 and 2.

Here we focus on transport in inhomogeneous patterns. Sophisticated transport modes can be achieved by adding complexity to either the patterns, the loops, or to both of them. We see examples of each type in the following sections. Details about the experiments and computer simulations are given in the "Methods" section.

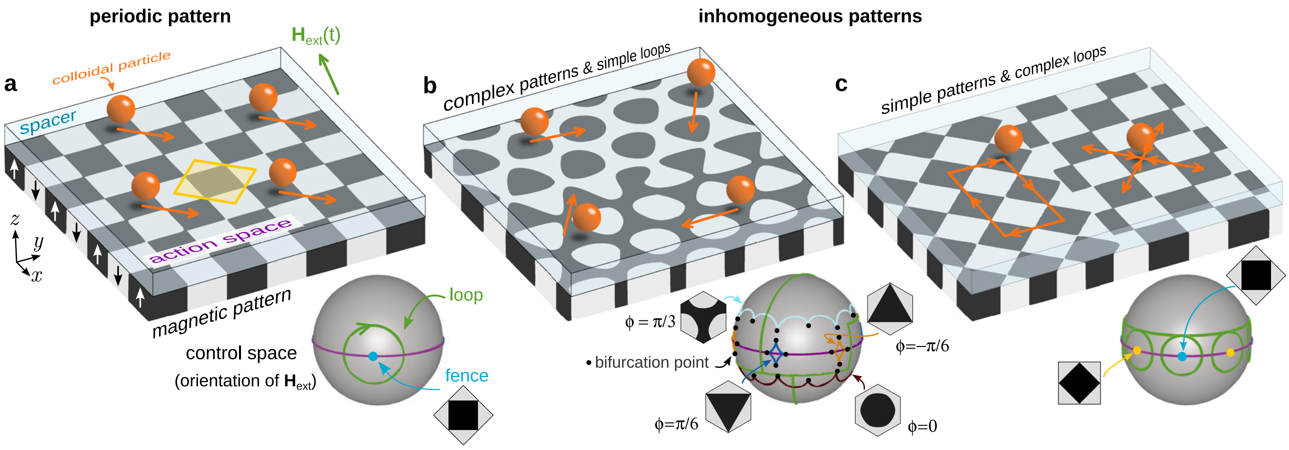

Fig. 1 | Periodic vs inhomogeneous patterns. a Periodic square pattern (a unit cell is highlighted in yellow), **b** hexagonal pattern in which the symmetry phase ϕ varies in space, and **c** a pattern made of two square patterns rotated by an angle of 45°. The patterns are made of regions with positive (black) and negative (white) magnetization normal to the pattern, see vertical arrows in (**a**). A polymer coating protects the patterns and acts as a spacer for the paramagnetic colloidal particles (orange) that are suspended in a solvent and move in a plane parallel to the pattern (action space). The motion is driven by a uniform external field (green arrow). The control space $\mathcal{C}$ (gray spheres) represents all possible orientations of the external field. The orientation of the external field varies in time performing a loop (green curves). Loops that wind around special orientations induce particle transport. These special orientations are determined by the position of the fences and bifurcation points in control space which depend on the local symmetry of the pattern. Shown are the fences of square patterns for one (**a**) and two (**c**) different orientations, as well as those of four hexagonal patterns with different symmetry phases ϕ (**b**). We also indicate the bifurcation points (black circles) in (**b**) which are those points where two fence segments meet. Next to the fences, we show the corresponding unit cell of the pattern. In periodic patterns (**a**) all the particles move in the same direction (orange arrows), independently of their position above the pattern. In inhomogeneous patterns, a single modulation loop can induce transport in different directions depending on the position of the particle above the pattern. Complex particle trajectories can be generated using complex patterns and simple loops (**b**) or simple patterns and complex loops (**c**).

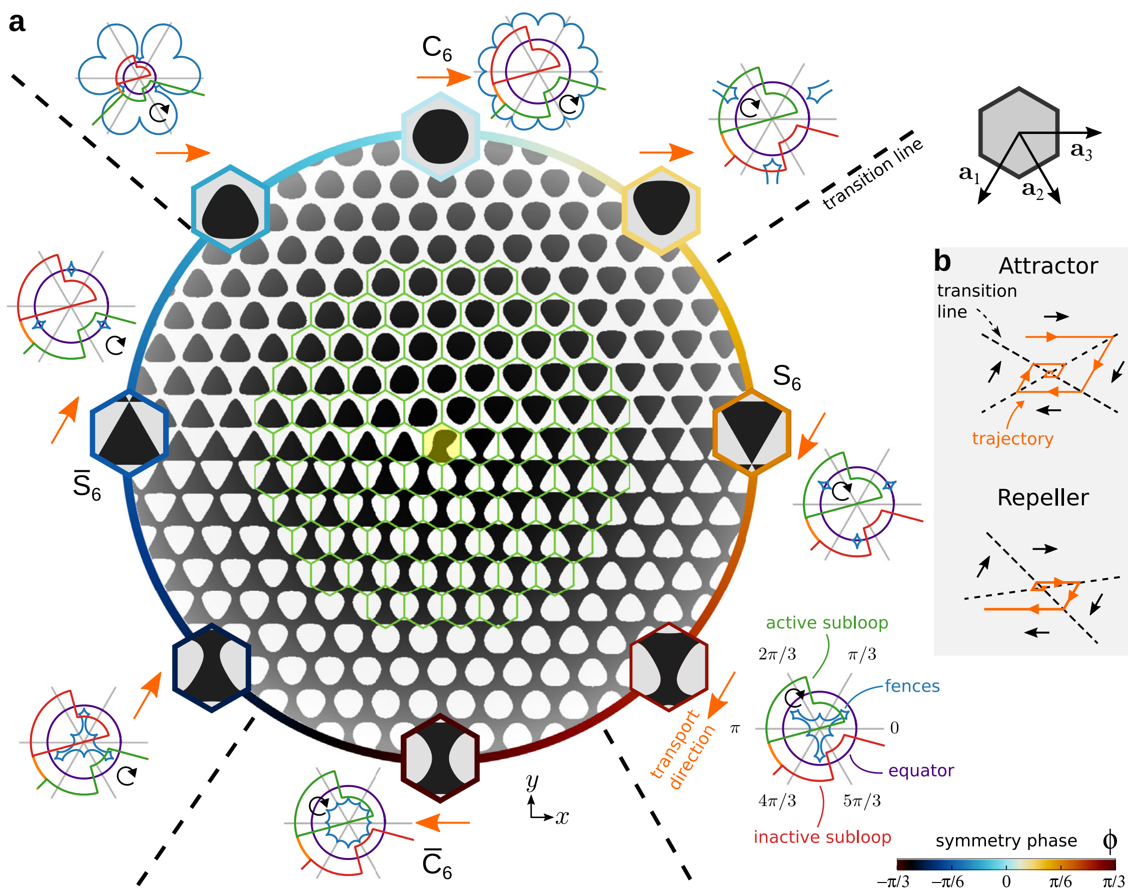

Fig. 2 | Pattern with a topological defect. a Magnetic pattern with a topological defect in the symmetry phase ϕ. The pattern is dissected into hexagonal cells (green hexagons). The central cell (yellow) contains the defect. Enlarged Wigner–Seitz cells of selected periodic hexagonal lattices with symmetry phase ϕ (see color bar) corresponding to their position in the pattern are shown. Next to each enlarged cell, we plot a stereographic projection of the corresponding control space and the modulation loop that attracts the particles toward the defect. Shown are the fences (blue), the equator (violet), and both the active (green) and the inactive (red) subloops. The loop winds as indicated by the circular black arrow. The two apparently open segments of the loop are actually joined at the south pole of the control space (not visible due to the projection). The transport direction (orange arrows) changes at the transition lines (black-dashed lines). **b** Illustrative configurations of the position of transition lines (black-dashed lines) that give rise to particle trajectories moving towards the defect (attractor) or away from it (repeller). The particle trajectories are illustrated in orange.

Complex patterns and simple loops

There is a full family of periodic hexagonal patterns characterized by the value of the symmetry phase ϕ (see the “Methods” section) and illustrative examples in Fig. 1b. We render the symmetry phase a continuous function of the position, which creates an inhomogeneous symmetry phase modulated pattern such as the example in Fig. 1b. For slow enough spatial changes of the symmetry phase, the cells of the modulated pattern deviate only weakly from the Wigner–Seitz cells of corresponding periodic patterns with fixed values of the symmetry phase. Hence, knowing how to control the transport in periodic patterns is enough to control the transport in inhomogeneous situations.

We focus first on complex inhomogeneous patterns designed to achieve locally different transport for a single specific task. Most of the complexity of the transport is embedded in the pattern and therefore the modulation loops of the external field are simple.

Topological defect in the symmetry phase

We show in Fig. 2 a symmetry phase modulated hexagonal pattern. The details to generate the pattern are given in the “Methods” section. Each time we wind around the center of the pattern we go through the full family of hexagonal patterns exactly once (including the inverse patterns with opposite magnetization) and return to the initial symmetry phase. This introduces a topological defect at the center of the pattern where the symmetry phase is not well defined.

The symmetry phase is constant along radial directions and the modulation is weak everywhere except near the defect. To illustrate this, we have dissected the pattern into hexagonal cells in Fig. 2a. We also show enlarged Wigner Seitz cells of periodic patterns with a symmetry phase corresponding to that of the radial ray of the inhomogeneous pattern. The Wigner Seitz cells of the periodic patterns resemble closely the cells of the inhomogeneous pattern, even in the proximity of the central defect. It is therefore expected that the transport in the inhomogeneous pattern can be understood in terms of the transport in periodic patterns.

The location of the fences in the control space varies substantially as we wind around the defect in the action space. (See the stereographic projections of control space for selected values of the symmetry phase in Fig. 2a and Supplementary Fig. 1.) Hence, it is possible to transport the microparticles into different directions depending on the sector of the pattern. In particular, we can construct modulation loops that use the central defect of the pattern as either an attractor or a repeller of colloidal particles.

A stereographic projection of the modulation loop that attracts the particles towards the defect is shown in Fig. 2a next to each enlarged Wigner–Seitz cell. The loop is made of two subloops. Only one of the subloops is active (green) for each value of the symmetry phase ϕ. The subloop is active in the sense that it induces net transport for those particles located in sectors of the pattern with that value of ϕ. The other subloop is inactive (red) in the sense that after one complete subloop, the particle returns to its position and hence there is no net transport. Using two subloops we control simultaneously the transport direction in sectors of the pattern with opposite magnetization (different values of the symmetry phase). Note for example how the active subloop in regions with C_6 symmetry ($\phi = 0$) becomes the inactive subloop in those regions with an inverse pattern $\overline{C_6}$ ($\phi = \pm\pi/3$) and vice versa (see Fig. 2a). To induce transport a subloop must wind around at least three bifurcation points of the fences in control space $\mathcal{C}$, as explained in the Supplementary Note 1. Recall that control space is simply the surface of a sphere in which each point corresponds to one orientation of the external magnetic field. The bifurcation points are the points in which two segments of the fences meet in $\mathcal{C}$, see examples in Supplementary Fig. 2.

The complete attractor loop, made of two subloops, induces four different transport directions (along $\pm\mathbf{a}_1$ and along $\pm\mathbf{a}_3$) depending on the value of the symmetry phase (see Fig. 2a). Here, $\mathbf{a}_i$, $i = 1, 2, 3$ are three lattice vectors of the periodic hexagonal pattern (see Fig. 2 and the “Methods” section). The transition between the different transport directions, e.g. from $+\mathbf{a}_3$ to $-\mathbf{a}_1$, occurs at specific values of the symmetry phase that can be adjusted with the loop. See the transition lines (dashed-black lines) in Fig. 2a.

By controlling the location of the transition lines we fix whether the defect acts as an attractor or a repeller of particles (see Fig. 2b). In both cases, the particles wind clockwise around the defect. Instead of changing the position of the transition lines, we could also control whether the defect attracts or repels microparticles by reversing the direction of the transport. However, this requires a complete redesign of the modulation loop. Simply reversing the direction of the modulation loop does not reverse in general the transport direction in the whole pattern due to the occurrence of non-time reversal ratchets in hexagonal patterns[37,39].

In Fig. 3a, b we show the trajectories of a colloidal particle located above the defect pattern according to Brownian dynamics simulations. The particle is randomly initialized above the pattern and then subjected to several repetitions of the attractor loop shown in Fig. 2. We also show the trajectory followed by the particle under the repetition of the repeller loop, depicted in Fig. 3c. The repeller and the attractor loops have similar shapes since they differ only in the values of ϕ at which the transport direction changes. The corresponding experimental trajectories are shown in Fig. 3d. In the experiments, there are several colloidal particles that are initially located above the pattern in random positions. If the attractor loop is repeated enough times, one colloidal particle will have reached the defect with almost certainty. Once a particle reaches the defect it stays there. In the experiments, further colloidal particles that try to enter the defect are repelled by the particle already occupying the center via dipolar repulsion. We can thus use the attractor loop to initialize one microparticle in the defect center. Whereas the location prior to the action of the attractor loop was unknown, it is known after the repeated application of the loop. The topological initialization is robust to thermal fluctuations. Brownian dynamics simulations of colloidal particles at higher temperatures still initialize the location of the defect. We briefly discuss the effect of finite temperature in the “Methods” section and Supplementary Fig. 4.

Encoding complex trajectories in the pattern

Patterns with spatial modulation of the symmetry phase can be used to encode arbitrarily complex particle trajectories. The patterns are designed to induce the desired trajectory when the particles are subjected to the repetition of a simple modulation loop of the orientation of the external field. The modulation loop transports particles along all possible directions in hexagonal patterns, i.e. along $\pm\mathbf{a}_i$ with $i = 1, 2, 3$, but in a way that only one direction is active for a given value of the symmetry phase. For example, particles on top of regions with C_6 symmetry are transported towards $-\mathbf{a}_3$. The transport direction

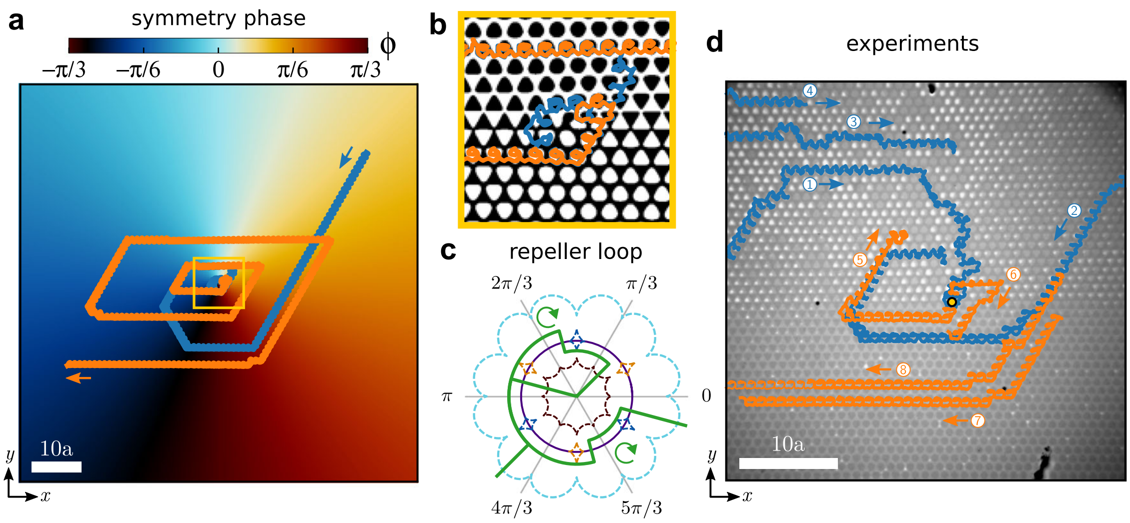

Fig. 3 | Attractor and repeller of particles. a Trajectory of a colloidal particle (randomly initialized) obtained with Brownian dynamics simulations above a pattern with a central topological defect in the symmetry phase. The blue (orange) trajectory is generated by the repetition of the attractor (repeller) modulation loop that moves particles towards (away from) the defect. The pattern is colored according to the value of the symmetry phase (color bar). The scale bar is $10a$. **b** Close-up of the region indicated by a yellow square in (**a**) and the trajectories around the central defect. The background shows the local magnetization of the pattern. **c** Stereographic projection of the repeller loop (green) in $\mathcal{C}$. The equator (violet circle) and the fences of the C_6 and S_6 patterns as well as their inverse patterns, $\overline{C_6}$ and $\overline{S_6}$, (dashed curves) are also depicted as a reference. The fences are colored according to the value of the symmetry phase. The two apparently open segments of the loop are actually joined at the south pole of the control space (not visible due to the projection). The loop is made of two subloops winding clockwise, as indicated by the circular arrows. **d** Experimental trajectories of several colloidal particles (labeled with a numbered circle) above the same pattern with a topological defect (yellow circle). The trajectories induced by the attractor (repeller) loop are colored in blue (orange). Blue and orange trajectories correspond to different experiments and have been superimposed in the figure. Note that under the microscope regions with negative magnetization appear darker than regions with positive magnetization, i.e. the opposite of our color choice in e.g. (**b**). The scale bar is $10a$ and the lattice constant of one cell is approx. 14 µm. Movies of the simulated and the experimental motion are provided in Supplementary Movie 1.

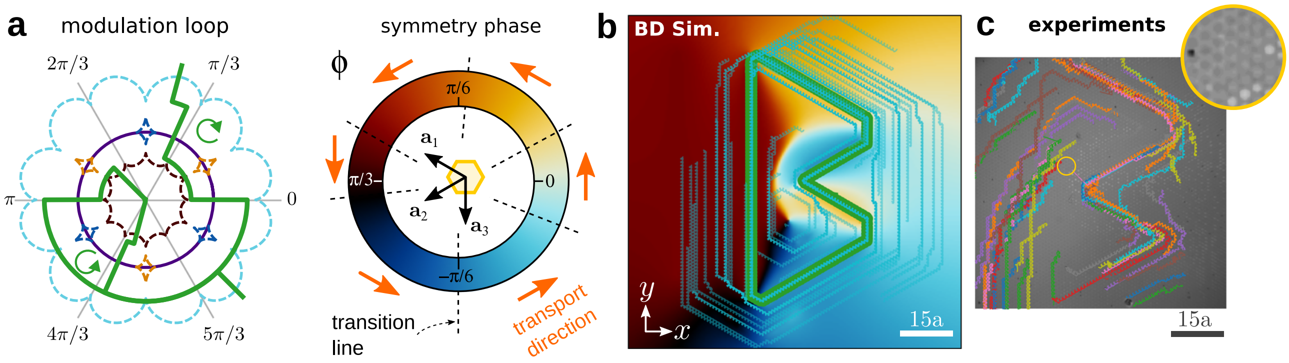

Fig. 4 | Symmetry phase modulated pattern. a Stereographic projection of control space showing the equator (violet circle), the closed modulation loop (green-solid curve), and the fences of patterns with C_6, S_6, $\overline{C}_6$ and $\overline{S}_6$ symmetries (dashed curves). The two apparently open segments of the loop are actually joined at the south pole of the control space (not visible due to the projection). The fences are colored according to the value of the symmetry phase (see the annular color bar). The transport directions induced by the loop (orange arrows) change at specific values of the symmetry phase ϕ as indicated by the transition lines (black-dashed lines). **b** Symmetry phase modulated pattern (the color indicates the value of the symmetry phase). A global rotation, $\psi = \pi/2$ in Eq. (6), makes one transport direction (lattice vector $\mathbf{a}_3$) parallel to the vertical axis. Particles above the pattern and subjected to the repetition of the modulation loop in (**a**) write the letter "B". Thin cyan lines show simulated particle trajectories for randomly initialized particles above the pattern. After several repetitions of the modulation loop, most particles enter the stable trajectory, highlighted with a thick green-solid line. **c** Experimental trajectories of colloidal particles above the pattern depicted in (**b**) and subjected to the modulation loop shown in (**a**). The region shown in the experiments (**c**) is smaller than that in simulations (**b**) due to the field of view of the microscope. The inset in (**c**) is a close view of the region indicated with a yellow circle in which we have altered the contrast of the image to better visualize the magnetization. Under the microscope regions with negative magnetization appear darker than those with positive magnetization. A colloidal particle (black dot) is also visible in the inset. A movie of the motion in simulations and experiments is provided in Supplementary Movie 2.

changes at specific values of the symmetry phase determined by the modulation loop. In Fig. 4a we show the modulation loop together with the representative fences and the resulting transport direction for each value of the symmetry phase.

The detailed procedure to generate the patterns is described in the “Methods” section and Supplementary Fig. 3. In essence, we first draw the trajectories that the particles should follow by hand. Then, at each position along the trajectory, we encode the transport direction using the value of the symmetry phase. Finally, the value of the symmetry phase at each point in the complete pattern is calculated as a spatially resolved weighted average of the symmetry phase along the trajectory. As a result, the symmetry phase varies smoothly across the pattern except for the occurrence of string-like topological defects in the symmetry phase.

Figure 4b shows a symmetry phase modulated pattern together with the corresponding simulated particle trajectories. The value of the symmetry phase is color-coded (see color bar). The pattern is designed to transport the particles along one stable trajectory that forms a closed loop resembling the letter “B”. In Fig. 4b we have highlighted the stable trajectory with a thick green line. Most particles above the pattern either enter the stable trajectory or leave the pattern. Occasionally one particle gets stuck in specific regions of the pattern. This can potentially be avoided by the introduction of random fluctuations in the modulation loop. In the presence of strong Brownian motion, the stable trajectories broaden to a width of a few unit cells, and additional stable trajectories might occur.

Corresponding experimental trajectories are shown in Fig. 4c. Even though the agreement is not perfect, the experimental trajectories follow closely the prescribed letter “B”, demonstrating, therefore, the potential of the method. Small variations in the position of the fences due to the imperfections of the pattern are likely the reason behind the deviations shown in the experiments. Fine-tuning the modulation loop and the height of the particles above the pattern would likely improve the results.

Simple patterns and complex loops

We follow now the opposite approach by encoding the complexity in the modulation loop. We create simple inhomogeneous patterns by concatenating large patches of periodic square patterns. The patches differ in the global orientation of the lattice vectors given by a global phase ψ (see the “Methods” section). Each (simple) patch allows for a rich variety of transport tasks. The task in each patch can be controlled individually and simultaneously using rather complex modulation loops in control space.

The fences of the C_4 square pattern are four equidistant points on the equator (see Supplementary Note 1). The four fence points in $\mathcal{C}$ correspond to external fields pointing along the positive and negative directions of the lattice vectors[37,44], i.e. along $\pm\mathbf{a}_1$ and $\pm\mathbf{a}_2$. Therefore, rotating the lattice vectors also rotates the position of the fences in control space. Thus, it is possible to construct loops that wind around different fences in $\mathcal{C}$, and hence induce different transport directions, depending on the orientation of the pattern ψ. An illustration is shown in Fig. 5a.

Since the fences are points in $\mathcal{C}$ it is in principle possible to concatenate an arbitrarily large number of patches with different orientations and control the motion in each of them independently. In practice, limiting factors might appear due to e.g. imperfections in the patterns that effectively make the fences in $\mathcal{C}$ extended regions, the angular resolution with which the orientation of the external field can be controlled, and the presence of Brownian motion. Due to the limiting factors, two patterns can be resolved independently if they are rotated by an angle of at least $\Delta\psi$. Hence, the maximum number of patches that can be controlled independently is $(\pi/2)/\Delta\psi$ since after a rotation of $\pi/2$ a C_4 pattern repeats itself (and so do the fences).

With a resolution $\Delta\psi = 5°$ it is then possible to control the motion in up to 18 patches independently. As an example we program a single loop in $\mathcal{C}$ that writes the first eighteen letters of the alphabet simultaneously, (see Fig. 5b and Supplementary Movie 3). Note that the letters are rotated by an angle ψ. For simplicity, we have designed an algorithm to write custom trajectories in a square pattern with global orientation $\psi = 0$. Next, we apply a global rotation to the modulation loop to control the transport in patterns with a generic orientation ψ. As a result, the trajectories are also rotated.

The loop that writes the first 18 letters of the alphabet contains 2086 simple commands. Each command is a small closed subloop that

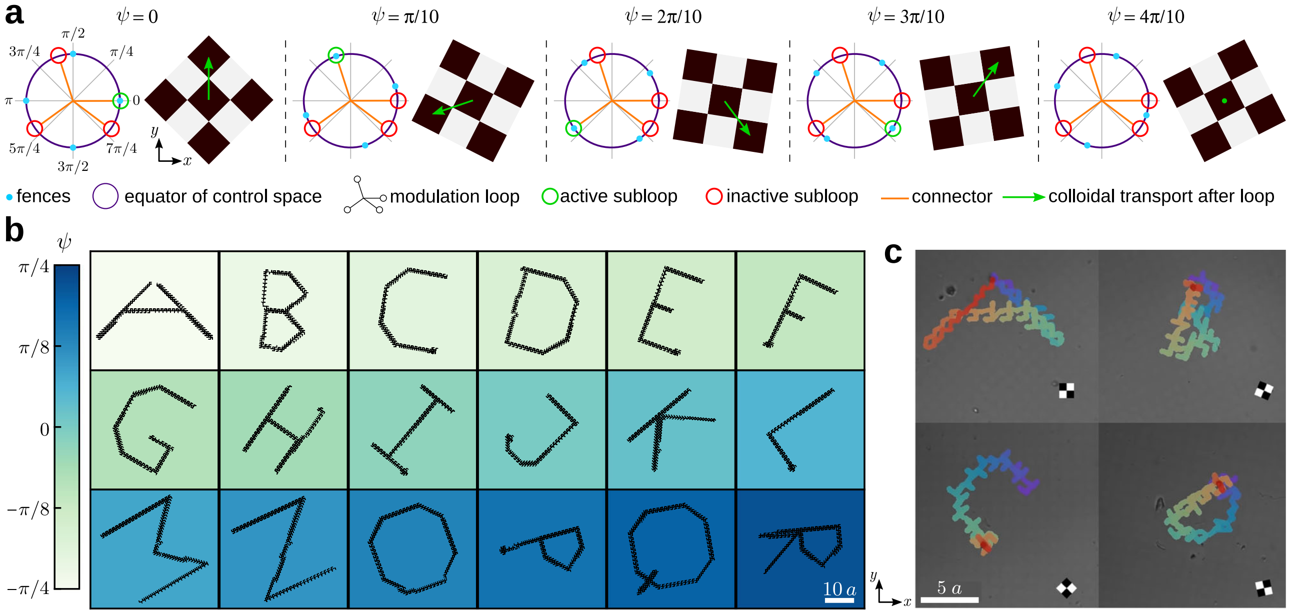

Fig. 5 | Simple patterns and complex loops. a Five square magnetic patterns (and their corresponding control spaces) with a different value of the global orientation ψ, as indicated. The fences in $\mathcal{C}$ (blue circles) are four points located on the equator (violet circle). The position of the fences depends on the value of ψ. The modulation loop consists of four interconnected subloops that wind counterclockwise. A subloop is active (green) if it winds around a fence point (blue circles) and inactive (red) otherwise. The orange segments of the modulation loop simply connect the different subloops. Depending on the value of ψ, the modulation loop induces different transport directions (green arrows) or no transport at all. **b** A pattern made of 18 patches with square symmetry and different global orientation ψ (color bar). A modulation loop controls the trajectories of particles above each patch simultaneously and independently. The particle trajectories (black) write the first 18 letters of the alphabet. The length of the scale bar is $10a$. A movie can be found in Supplementary Movie 3. **c** Experimental trajectories of colloidal particles above four square patches rotated with respect to each other. A schematic unit cell illustrating the global orientation is depicted in each patch. The length of the scale bar is $5a$ and in this case, we use patterns with $a = 7$ µm. A unique modulation loop transports the four colloidal particles simultaneously. The trajectories are colored according to the time evolution from blue (initial time) to red (final time). A movie showing the whole time evolution and a one-to-one comparison with computer simulations is available in Supplementary Movie 4.

either transports a particle in one unit cell along the four possible directions of the square lattice or leaves the particle in the same position, similar to the loops in Fig. 5a. Even though an angular resolution of $\Delta\psi = 5°$ is achievable experimentally, the number of commands required by the complete loop exceeds our current experimental capabilities. Nevertheless, we show in Fig. 5c, the experimental trajectories of a simplified loop that writes low-resolution versions of the first four letters of the alphabet. The loop is made of 96 simple commands. The agreement with computer simulations is essentially perfect, as we demonstrate in a one-to-one comparison in Supplementary Movie 4.

The simultaneous control of the transport in several patches of rotated square patterns is particularly simple due to the simplicity of the fences in $\mathcal{C}$. However, the same ideas apply to patterns with other symmetry classes.

Here, we have initialized the particles in the desired positions within their respective patches. As we discuss now, it is possible to automatize this process by combining the patches with complex patterns.

Complex patterns and complex loops

Complete control over the colloidal transport is achieved by combining complex patterns and complex loops. In Fig. 6 we combine three C_4 patches that differ in their global orientation ψ and three hexagonal patterns with a topological defect in the symmetry phase. The transition between both patterns occurs smoothly within a region of length equivalent to approximately five unit cells of the square patterns.

We first make use of the patterns with a topological defect to move randomly placed particles toward the defects. We simply repeat the attractor modulation loop shown in Fig. 2 several times such that the particles move and stay at the defects, see the blue trajectories of the particles in Fig. 6. Once this initialization stage is finished we know the precise position of the particles and can control them independently. Using two simple loops we transport the particles downwards from the defects to the square patches. We use one loop to move the particles in the defect pattern (orange trajectories) and another loop to move the particles in the transition region and the square patches (green trajectories). Then, a relatively complex loop controls the motion of the three particles independently. Each particle follows a complex trajectory drawing either a square, a triangle, or a cross depending on the value of the global orientation ψ (red trajectories). Experimentally we tested each part of the loop separately, as shown in the insets of Fig. 6. Again, the agreement between simulations and experiments is excellent. The small errors that occur in the experimental trajectories, likely due to imperfections in the pattern, do not affect the global shape of the trajectories. A movie of the whole process is shown in Supplementary Movie 5.

Discussion

We have shown that the combination of a complex static magnetic field with a simple time-dependent uniform external field of varying orientation allows us to control the motion of several identical microparticles independently and simultaneously. The transport complexity can be broken down to a finite set of special orientations of the external field. A modulation loop that winds around one of those orientations induces transport along a known direction in a known region of the pattern. The motion is topologically protected since only the winding numbers of the modulation loop around the special orientations (topological invariant) are important. Hence, it is relatively simple to generate loops and patterns that induce arbitrarily complex trajectories. Our ideas might be transferable to other systems

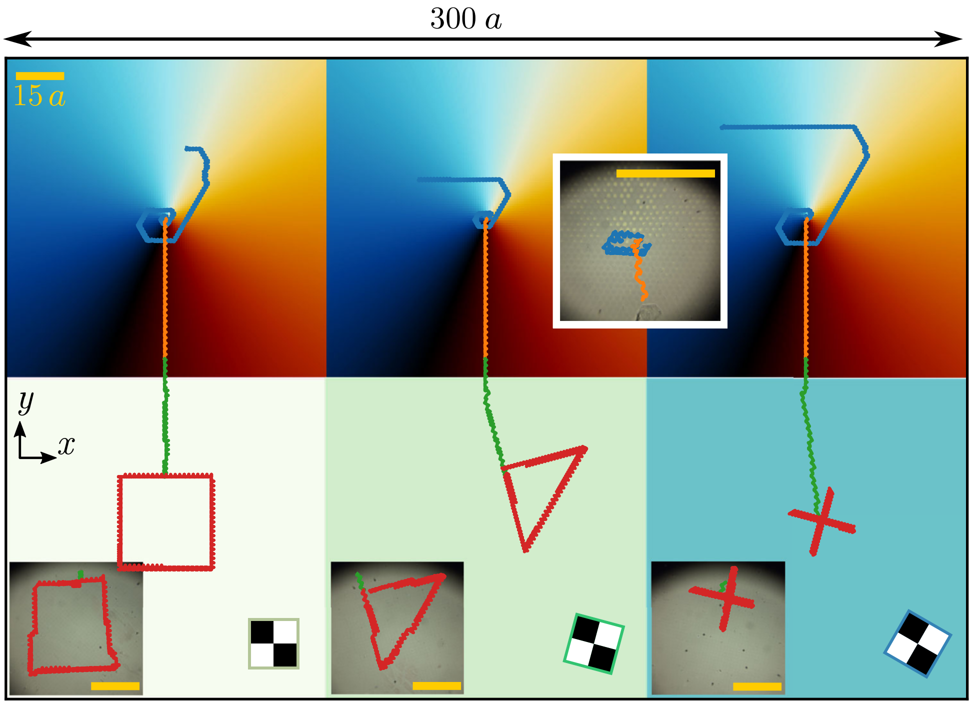

Fig. 6 | Complex patterns and complex loops. Brownian dynamics simulations of the transport of colloidal particles above a complex pattern made of three patches, each one with a topological defect in the symmetry phase (top) connected to three patches with square symmetry (down) rotated with respect to each other. The color of the patches with topological defects indicates the value of the symmetry phase ϕ. The color of the square patches indicates the global rotation ψ, illustrated with a sketch of the magnetization. A unique complex modulation loop made of four parts drives the transport in the whole system. In the first part, the repetition of the attractor loop moves the particles toward the defects (blue trajectories) and lets them wait there. The second part of the loop moves the particles downwards through the patterns with defects (orange trajectories). The third part of the loop moves the particles downwards in the square patterns (green trajectories). The last part of the loop writes a custom trajectory (square, triangle, and cross) depending on the global orientation ψ of the pattern (red trajectories). Insets show the corresponding experimental trajectories. The length of the scale bars (yellow) is 15a.

in which the transport is also based on topological protection. These include, solitons[45], nano-machines[46,47], sound waves[48,49], photons[50,51], and quantum mechanical excitations[52].

The complexity of the transport is encoded in the magnetic potential which varies in space and in time via the magnetic patterns and the modulation loops, respectively. An alternative approach that encodes the transport in the particle shape has appeared recently[53]. There, Sobolev et al. find the shape of the rigid body that traces the desired trajectory when rolling down a slope. We have restricted our study to identical isotropic paramagnetic particles. However, as discussed in the "Introduction" section, colloidal particles with different characteristics (e.g. diamagnetic and paramagnetic particles or particles with different shapes) might belong to different topological classes. The fences of particles belonging to different topological classes are located in different regions in $\mathcal{C}$. Above non-periodic patterns, the control space of particles belonging to different topological classes will also depend on the space coordinate. A precise control over the transport depending not only on the position but also on the particle characteristics is then possible. Therefore, beyond offering the possibility to control the transport of identical microparticles simultaneously, our work also opens a new route towards dynamical self-assembly in colloidal science. As an example, we have created a colloidal rod factory[54] in which identical isotropic particles are transported toward a reaction site in which they self-assemble. Only when they reach the desired aspect ratio, do the rods leave the polymerization site following the desired trajectory. The use of patchy colloids[55–58] with, e.g. hybridization of complementary DNA strands[59–61] and other shape-anisotropic particles[62,63] would offer more versatility to create complex functional structures.

We have considered transport above patterns made of identical patches rotated with respect to each other. It is also possible to combine patches of patterns with different symmetries provided that their respective fences do not overlap in control space. Moreover, a combination of both, i.e. a pattern made of patches with different symmetries, e.g. C_4 and C_6, that in addition are rotated with respect to each other would substantially increase the number of tasks that can be done simultaneously since their respective fences in control space do not overlap.

In the experiments, the Brownian motion of the colloidal particles is negligible but it might play a role in other systems with smaller colloids and/or at higher temperatures. Since the transport is topologically protected, it is robust against perturbations such as the presence of Brownian motion[44]. If we make Brownian motion more prominent (e.g. by increasing the temperature or reducing the particle size) the particles start to deviate from the expected trajectories but overall the transport is robust. An example of Brownian dynamics simulations at different temperatures is shown in Supplementary Fig. 4. The topological protection will disappear due to Brownian motion at sufficiently high temperatures and for small enough particles. A possible solution would then be to increase the magnitude of either the pattern field or the external magnetic field such that the magnetic forces dominate again the transport.

Our systems are very dilute and therefore direct interparticle interactions and hydrodynamic interactions do not play any role. However, it would be interesting to look at the effect of both superadiabatic forces[64] and long-range hydrodynamic interactions[65] in denser systems.

Methods

System setup and computer simulations

Identical paramagnetic colloidal particles immersed in a solvent are located above a magnetic pattern and are restricted to move in a plane parallel to the pattern (xy-plane), which we call action space $\mathcal{A}$ (Fig. 1a). The pattern contains regions of positive, $+m_p$, and negative, $-m_p$, uniform magnetization along the z-direction (normal to the pattern). The width of the domain walls between oppositely magnetized regions is negligible. The particles are driven by a time- and space-dependent external magnetic potential $V_{\text{mag}}(\mathbf{r}_{\mathcal{A}},t)$. The potential is generated by the static but space-dependent magnetic field of the pattern $\mathbf{H}_p(\mathbf{r}_{\mathcal{A}})$ and a time-dependent but spatially homogeneous external magnetic field $\mathbf{H}_{\text{ext}}(t)$. Here $\mathbf{r}_{\mathcal{A}}$ is the space coordinate in action space and t denotes the time. The magnitude of the external field (constant) is much larger than that of the pattern field, i.e. $H_{\text{ext}} \gg H_p(\mathbf{r}_{\mathcal{A}})$ for any position in $\mathcal{A}$. Hence, the magnetic potential, which is proportional to the square of the total magnetic field $V_{\text{mag}} \propto -(\mathbf{H}_{\text{ext}}+\mathbf{H}_p)\cdot(\mathbf{H}_{\text{ext}}+\mathbf{H}_p)$, is dominated by the coupling between the external and the pattern fields:

$$V_{\text{mag}}(\mathbf{r}_{\mathcal{A}},t) \approx -v_0\chi\mu_0\mathbf{H}_p(\mathbf{r}_{\mathcal{A}})\cdot\mathbf{H}_{\text{ext}}(t). \tag{1}$$

Here μ_0 is the vacuum permeability, χ is the magnetic susceptibility of the colloidal particle, and v_0 is the particle volume[37]. We have omitted the term proportional to $\mathbf{H}_{\text{ext}}\cdot\mathbf{H}_{\text{ext}}$ in V_{mag} since it is just a constant and therefore it does not affect the motion.

In the overdamped limit, the equation of motion of one particle reads

$$\gamma\dot{\mathbf{r}}_{\mathcal{A}} = -\nabla_{\mathcal{A}}V_{\text{mag}} + \boldsymbol{\eta}, \tag{2}$$

where γ is the friction coefficient against the implicit solvent, the overdot denotes time derivative, $\nabla_{\mathcal{A}}$ is the derivative with respect to $\mathbf{r}_{\mathcal{A}}$, and $\boldsymbol{\eta}$ is a delta-correlated Gaussian random force with zero mean that models the effect of the collisions between the molecules of the solvent and the colloidal particle (Brownian motion). We define our energy scale ε as the absolute value of the average external energy that a particle would have when the external magnetic field points normal to the pattern. Hence, absolute temperature T is given in reduced units k_BT/ε where k_B is the Boltzmann's constant. We use the magnitude of a lattice vector of the periodic pattern a as the length scale. The timescale is hence given by $\tau = \gamma a^2/\varepsilon$. We use adaptive Brownian dynamics[66] to efficiently integrate the equation of motion. In the experiments, the magnetic forces strongly dominate over the random forces. Hence, random forces do not play any role. We use Brownian dynamics simulations due to the overdamped character of the motion in the viscous aqueous solvent. The code to simulate the colloidal motion and to generate the modulation loops is available via Zenodo[67].

As the external magnetic field is homogeneous in space, it can be solely described by its orientation. The set of all possible orientations of $\mathbf{H}_{\text{ext}}$ forms a spherical surface that we call control space $\mathcal{C}$. A point in $\mathcal{C}$ indicates an orientation of $\mathbf{H}_{\text{ext}}$. We drive the colloidal motion by performing closed loops of the orientation of $\mathbf{H}_{\text{ext}}$ in $\mathcal{C}$. Loops that wind around specific points in $\mathcal{C}$ induce colloidal motion. That is, once the loop returns to its initial position, the colloidal particle has moved to a different unit cell of the pattern. The transport is topologically protected since the precise form of the loop is irrelevant. Only the winding numbers of the loop around the specific points in $\mathcal{C}$ (which are the topological invariants) determine the transport.

Experiments

The magnetic films with the desired patterns imprinted are thin Co/Au multilayers with perpendicular magnetic anisotropy[68] lithographically patterned via a home-built[69] keV-He-ion bombardment[70]. Further details about the fabrication process can be found in refs. 37,71–73. The patterns have lattice vectors of magnitude 14 µm if not stated otherwise.

To reduce the influence of lateral magnetic field fluctuations due to the fabrication procedure (which increases near the substrate) we coat the magnetic pattern with a photo-resist film (thickness 1.6 µm). The coating layer serves other two purposes: it protects the patterns and it acts as a spacer between the colloidal particles and the pattern (see Fig. 1), in order to secure the condition $|\mathbf{H}_{\text{ext}}| \gg |\mathbf{H}_p|$. We then place paramagnetic colloids of diameter 2.8 µm immersed in deionized water on top of the pattern. The microparticles sediment and are suspended roughly the Debye length above the negatively charged coating layer on the pattern. The motion above the pattern is effectively two-dimensional.

The uniform external magnetic field is generated with three coils arranged around the pattern and controlled with a computer. The magnitude of the external field is approximately 4×10^3 A/m. Standard reflection microscopy techniques are used to visualize both the colloids and the pattern.

Square and hexagonal periodic patterns

Consider magnetic periodic N-fold symmetric patterns with either $N=2$ (square patterns) or $N=3$ (hexagonal patterns). Examples of both types are shown in Supplementary Fig. 1. In the limit of an infinitely thin pattern located at $z=0$, the magnetization is

$$\mathbf{M}(\mathbf{r}) = M(\mathbf{r}_\perp)\delta(z)\hat{\mathbf{e}}_z, \tag{3}$$

with $\delta(\cdot)$ the Dirac distribution, $\hat{\mathbf{e}}_z$ the unit vector normal to the pattern, $\mathbf{r}_\perp = (x,y)$, and

$$M(\mathbf{r}_\perp) = m_p\,\text{sign}\left(\sum_{i=1}^{N}\cos(\mathbf{q}_i\cdot(\mathbf{r}_\perp-\mathbf{b})-\phi)+m_0(\phi)\right), \tag{4}$$

where m_p is the saturation magnetization of the domains. The wave vectors $\mathbf{q}_i$ in the square patterns are

$$\mathbf{q}_i = q_0\begin{pmatrix}-\sin(\pi i/2-\psi)\\ \cos(\pi i/2-\psi)\end{pmatrix},\quad i=1,2 \tag{5}$$

with magnitude $q_0 = 2\pi/a$ and a being the magnitude of a lattice vector, which in square patterns can be defined with the wave vectors being the reciprocal lattice vectors. That is, $\mathbf{a}_i\cdot\mathbf{q}_j = 2\pi\delta_{ij}$ (see Supplementary Fig. 1b). The global phase ψ sets the orientation of the lattice vectors with respect to a fixed laboratory frame.

In the hexagonal patterns, the wave vectors are

$$\mathbf{q}_i = q_0\begin{pmatrix}-\sin(2\pi i/3-\psi)\\ \cos(2\pi i/3-\psi)\end{pmatrix},\quad i=1,2,3 \tag{6}$$

with magnitude $q_0 = 4\pi/(a\sqrt{3})$. Here, the three wave vectors can be related to three (linearly dependent) lattice vectors via $\mathbf{q}_i\cdot\mathbf{a}_j = 2\pi\delta_{ij}$ for $i=1,2$ and $\mathbf{a}_3\cdot\mathbf{q}_3 = 0$ (see Supplementary Fig. 1b).

In both square and hexagonal patterns, the wave vectors point into the N different symmetry directions. The translational vector $\mathbf{b}$ in Eq. (4) plays a relevant role only in inhomogeneous patterns. In periodic patterns, we usually set $\mathbf{b}=\mathbf{0}$.

In square patterns, the symmetry phase ϕ in the magnetization (see Eq. (4)), simply causes a trivial shift of all Wigner–Seitz cells with respect to the origin of the pattern. Hence, for simplicity, we set it to zero. In hexagonal patterns however, the symmetry phase ϕ has a nontrivial effect since it determines the point symmetry of the pattern (see Supplementary Fig. 1c), and therefore the modulation loops required to transport the colloidal particles[37]. The Wigner–Seitz cell of a hexagonal pattern contains in general three symmetry points with C_3 symmetry (rotation through an angle $2\pi/3$ about the symmetry axis). For special values of the symmetry phase, one of the three-fold

 https://doi.org/10.1038/s41467-023-43390-0

symmetric points acquires a higher symmetry; either six-fold hexagonal C_6 symmetry (for $\phi = 0$ and $\phi = \pm\pi/3$) or S_6 symmetry, i.e. a C_6 followed by a perpendicular reflection (for $\phi = \pm\pi/6$).

Finally, the parameter m_0 in Eq. (4), which is actually a function of the symmetry phase ϕ, alters the area ratio between up-magnetized and down-magnetized domains. Following Loehr et al.[37], we use here $m_0(\phi) = \frac{1}{2}\cos(3\phi)\delta_{N,3}$ (therefore in square patterns $m_0 = 0$) to ensure that the average magnetization in hexagonal patterns is very small, i.e.

$$\int M(\mathbf{r}_\perp)\mathrm{d}\mathbf{r}_\perp \approx 0. \tag{7}$$

Magnetic field of the pattern

To numerically compute the magnetic field of the pattern, $\mathbf{H}_\mathrm{p}(\mathbf{r})$, at the desired position in action space we first discretize the pattern in a square grid with resolution $0.03a$ and compute the magnetization at the grid points via Eq. (4). Next, we compute the magnetic field at the grid points by convolution of the magnetization with the Green's-function of the system:

$$\mathbf{H}_\mathrm{p}(\mathbf{r}) = \mathbf{H}_\mathrm{p}(\mathbf{r}_\perp, z) = \frac{1}{4\pi}\int \mathrm{d}\mathbf{r}'_\perp \frac{\mathbf{r}_\perp - \mathbf{r}'_\perp + z\hat{\mathbf{e}}_z}{|\mathbf{r}_\perp - \mathbf{r}'_\perp + z\hat{\mathbf{e}}_z|^3} M(\mathbf{r}'_\perp). \tag{8}$$

Here $\mathbf{r}_\perp = (x, y)$ is the position coordinate in a plane parallel to the pattern. We calculate the magnetic field at an elevation above the pattern $z = 0.5a$, which is comparable to the experimental value. As usual, we perform the convolution in Fourier space.

To calculate the magnetic field at a generic, off-grid, position we simply interpolate the magnetic field using bicubic splines.

Pattern with a topological defect

For the pattern with a topological defect shown in Fig. 2, the symmetry phase varies with the position $\mathbf{r}_\perp$ as

$$\phi(\mathbf{r}_\perp) = \frac{1}{3}\left(\frac{\pi}{2} - \arctan\left(\mathbf{q}_3 \cdot \mathbf{r}_\perp, \hat{\mathbf{e}}_z \cdot (\mathbf{r}_\perp \times \mathbf{q}_3)\right)\right), \tag{9}$$

and the global orientational phase is set to $\psi = 0$ in Eq. (6). For our choice of wave vectors (see Eq. (6) and Supplementary Fig. 1b), the symmetry phase modulation is simply $\phi(\mathbf{r}_\perp) = (\pi/2 - \arctan(x, y))/3$. Here $\arctan(y, x)$ returns the four-quadrant inverse tangent of y/x. The symmetry phase varies therefore between $\phi = -\pi/3$ and $\pi/3$ as we wind once around the origin. The topological charge of the defect located at the center of the pattern ($\mathbf{r}_\perp = 0$) is $q = \Delta\phi/(2\pi/p) = 1$. Here $\Delta\phi = 2\pi/3$ is the angle that the director rotates if we wind once counter-clockwise around the defect, and $p = 3$ is the p-atic symmetry of the director field[74]. (The symmetry phase can be described with a 3-atic director field for which the local orientations are defined modulo $\pi/3$.) Varying the symmetry phase between $-\pi/3$ and $\pi/3$ also introduces a shift of the unit cell, cf. the unit cells for $\phi = \pi/3$ and $-\pi/3$ in Supplementary Fig. 1c. To rectify this shift and avoid therefore discontinuities in the magnetization of the pattern, we need to use a local shift vector in Eq. (4) given by

$$\mathbf{b}(\mathbf{r}_\perp) = -(\mathbf{a}_1 + \mathbf{a}_2)\frac{\phi(\mathbf{r}_\perp)}{2\pi}. \tag{10}$$

The shift vector can be understood as a Burgers vector since it corrects for the spatial distortion of the pattern around the defect.

Symmetry phase modulated patterns

To encode in the pattern the desired particle trajectories, we use the drawing software Krita[75]. We prescribe the stable trajectory on a square image with a side-length of 1000 pixels. In Krita, we draw the desired trajectory with a brush (thickness 1 pixel) that encodes the drawing direction in the hue of the colored pixels. The drawing direction directly translates into the transport direction that the particles will follow above the pattern. This procedure results in an image that is essentially empty except for the trajectory lines. We then map from hue to the symmetry phase ϕ. An example of the pattern at this stage is shown in Supplementary Fig. 3a. The mapping from hue to ϕ is simply a linear transformation.

Next, we give a value to the symmetry phase everywhere in the pattern. To calculate the phase at a generic position $\mathbf{r}_\perp = (x, y)$ we average over all the prescribed phases along the trajectories. Each phase along the trajectory is weighted with a weight function proportional to $1/r_\mathrm{d}^2$, with r_d the distance between $\mathbf{r}_\perp$ and a point on the trajectory. Special care needs to be taken due to the periodicity of the symmetry phase[76]. We first transform the phases along the trajectories into unit vectors, next we average the vectors, and then transform back the averaged vector into a value of the symmetry phase. An illustration of the pattern after this stage is shown in Supplementary Fig. 3b. Finally, we use the value of the symmetry phase in the whole pattern to calculate the magnetization via Eq. (4) (see Supplementary Fig. 3c).

Data availability

The code to simulate the system and to generate the modulation loops is available at Zenodo[67]. All other data supporting the findings are available from the corresponding author upon request.

Code availability

A code to perform the adaptive Brownian Dynamics simulations of the colloidal particles as well as to generate the modulation loops is available at Zenodo[67].

References

1. Royall, C. P., Dzubiella, J., Schmidt, M. & van Blaaderen, A. Nonequilibrium sedimentation of colloids on the particle scale. *Phys. Rev. Lett.* **98**, 188304 (2007).
2. Yang, L. & Alexandridis, P. Physicochemical aspects of drug delivery and release from polymer-based colloids. *Curr. Opin. Colloid Interface Sci.* **5**, 132–143 (2000).
3. Boyd, B. J. Past and future evolution in colloidal drug delivery systems. *Expert Opin. Drug Deliv.* **5**, 69–85 (2007).
4. Beija, M., Salvayre, R., de Viguerie, N. L. & Marty, J.-D. Colloidal systems for drug delivery: from design to therapy. *Trends Biotechnol.* **30**, 485–496 (2012).
5. McGorty, R., Fung, J., Kaz, D. & Manoharan, V. N. Colloidal self-assembly at an interface. *Mater. Today* **13**, 34–42 (2010).
6. Mallory, S. A., Valeriani, C. & Cacciuto, A. An active approach to colloidal self-assembly. *Annu. Rev. Phys. Chem.* **69**, 59–79 (2018).
7. Dijkstra, M. & Luijten, E. From predictive modelling to machine learning and reverse engineering of colloidal self-assembly. *Nat. Mater.* **20**, 762–773 (2021).
8. Terray, A., Oakey, J. & Marr, D. W. M. Microfluidic control using colloidal devices. *Science* **296**, 1841–1844 (2002).
9. Holzinger, D., Lengemann, D., Göllner, F., Engel, D. & Ehresmann, A. Controlled movement of superparamagnetic bead rows for microfluid mixing. *Appl. Phys. Lett.* **100**, 153504 (2012).
10. Lim, B. et al. Magnetophoretic circuits for digital control of single particles and cells. *Nat. Commun.* **5**, 3846 (2014).
11. Wang, L. & Wang, J. Self-assembly of colloids based on microfluidics. *Nanoscale* **11**, 16708–16722 (2019).
12. Shin, S. Diffusiophoretic separation of colloids in microfluidic flows. *Phys. Fluids* **32**, 101302 (2020).
13. Abedini-Nassab, R., Sadeghidelouei, N. & Shields IV, C. W. Magnetophoretic circuits: a review of device designs and implementation for precise single-cell manipulation. *Anal. Chim. Acta* **1272**, 341425 (2023).

14. Koumakis, N., Maggi, C. & Leonardo, R. D. Directed transport of active particles over asymmetric energy barriers. *Soft Matter* **10**, 5695–5701 (2014).
15. Schakenraad, K. et al. Topotaxis of active Brownian particles. *Phys. Rev. E* **101**, 032602 (2020).
16. Martinez, R., Alarcon, F., Aragones, J. L. & Valeriani, C. Trapping flocking particles with asymmetric obstacles. *Soft Matter* **16**, 4739–4745 (2020).
17. Löwen, H. Colloidal soft matter under external control. *J. Phys.: Condens. Matter* **13**, R415–R432 (2001).
18. Erbe, A., Zientara, M., Baraban, L., Kreidler, C. & Leiderer, P. Various driving mechanisms for generating motion of colloidal particles. *J. Phys.: Condens. Matter* **20**, 404215 (2008).
19. Reichhardt, C. & Reichhardt, C. J. O. Depinning and nonequilibrium dynamic phases of particle assemblies driven over random and ordered substrates: a review. *Rep. Prog. Phys.* **80**, 026501 (2016).
20. Köppl, M., Henseler, P., Erbe, A., Nielaba, P. & Leiderer, P. Layer reduction in driven 2D-colloidal systems through microchannels. *Phys. Rev. Lett.* **97**, 208302 (2006).
21. Vissers, T. et al. Lane formation in driven mixtures of oppositely charged colloids. *Soft Matter* **7**, 2352–2356 (2011).
22. Li, P., Kilinc, D., Ran, Y.-F. & Lee, G. U. Flow enhanced non-linear magnetophoretic separation of beads based on magnetic susceptibility. *Lab Chip* **13**, 4400–4408 (2013).
23. Holzinger, D., Koch, I., Burgard, S. & Ehresmann, A. Directed magnetic particle transport above artificial magnetic domains due to dynamic magnetic potential energy landscape transformation. *ACS Nano* **9**, 7323–7331 (2015).
24. Tierno, P., Golestanian, R., Pagonabarraga, I. & Sagués, F. Controlled swimming in confined fluids of magnetically actuated colloidal rotors. *Phys. Rev. Lett.* **101**, 218304 (2008).
25. Ashkin, A., Dziedzic, J. M., Bjorkholm, J. E. & Chu, S. Observation of a single-beam gradient force optical trap for dielectric particles. *Opt. Lett.* **11**, 288–290 (1986).
26. Magnasco, M. O. Forced thermal ratchets. *Phys. Rev. Lett.* **71**, 1477–1481 (1993).
27. Faucheux, L. P., Bourdieu, L. S., Kaplan, P. D. & Libchaber, A. J. Optical thermal ratchet. *Phys. Rev. Lett.* **74**, 1504–1507 (1995).
28. Hänggi, P. & Marchesoni, F. Artificial Brownian motors: controlling transport on the nanoscale. *Rev. Mod. Phys.* **81**, 387–442 (2009).
29. Matthias, S. & Müller, F. Asymmetric pores in a silicon membrane acting as massively parallel Brownian ratchets. *Nature* **424**, 53–57 (2003).
30. Lee, S.-H., Ladavac, K., Polin, M. & Grier, D. G. Observation of flux reversal in a symmetric optical thermal ratchet. *Phys. Rev. Lett.* **94**, 110601 (2005).
31. Skaug, M. J., Schwemmer, C., Fringes, S., Rawlings, C. D. & Knoll, A. W. Nanofluidic rocking Brownian motors. *Science* **359**, 1505–1508 (2018).
32. Anderluh, A., Hemmelmayr, V. C. & Nolz, P. C. Synchronizing vans and cargo bikes in a city distribution network. *Cent. Eur. J. Oper. Res.* **25**, 345–376 (2016).
33. Korda, P. T., Taylor, M. B. & Grier, D. G. Kinetically locked-in colloidal transport in an array of optical tweezers. *Phys. Rev. Lett.* **89**, 128301 (2002).
34. MacDonald, M. P., Spalding, G. C. & Dholakia, K. Microfluidic sorting in an optical lattice. *Nature* **426**, 421–424 (2003).
35. Ladavac, K., Kasza, K. & Grier, D. G. Sorting mesoscopic objects with periodic potential landscapes: optical fractionation. *Phys. Rev. E* **70**, 010901 (2004).
36. Lacasta, A. M., Sancho, J. M., Romero, A. H. & Lindenberg, K. Sorting on periodic surfaces. *Phys. Rev. Lett.* **94**, 160601 (2005).
37. Loehr, J. et al. Lattice symmetries and the topologically protected transport of colloidal particles. *Soft Matter* **13**, 5044–5075 (2017).
38. Mirzaee-Kakhki, M. et al. Simultaneous polydirectional transport of colloidal bipeds. *Nat. Commun.* **11**, 4670 (2020).
39. Loehr, J., Loenne, M., Ernst, A., de las Heras, D. & Fischer, T. M. Topological protection of multiparticle dissipative transport. *Nat. Commun.* **7**, 11745 (2016).
40. Phillips, C. L. et al. Digital colloids: reconfigurable clusters as high information density elements. *Soft Matter* **10**, 7468–7479 (2014).
41. Chakraborty, I. et al. Self-assembly dynamics of reconfigurable colloidal molecules. *ACS Nano* **16**, 2471–2480 (2022).
42. Solomon, M. J. Tools and functions of reconfigurable colloidal assembly. *Langmuir* **34**, 11205–11219 (2018).
43. Hendley, R. S., Zhang, L. & Bevan, M. A. Multistate dynamic pathways for anisotropic colloidal assembly and reconfiguration. *ACS Nano* **17**, 20512–20524 (2023).
44. de las Heras, D., Loehr, J., Loenne, M. & Fischer, T. M. Topologically protected colloidal transport above a square magnetic lattice. *New. J. Phys.* **18**, 105009 (2016).
45. ge Chen, B. G., Upadhyaya, N. & Vitelli, V. Nonlinear conduction via solitons in a topological mechanical insulator. *Proc. Natl. Acad. Sci. USA* **111**, 13004–13009 (2014).
46. Porto, M., Urbakh, M. & Klafter, J. Atomic scale engines: cars and wheels. *Phys. Rev. Lett.* **84**, 6058–6061 (2000).
47. Popov, V. L. Nanomachines: methods to induce a directed motion at nanoscale. *Phys. Rev. E* **68**, 026608 (2003).
48. Nash, L. M. et al. Topological mechanics of gyroscopic metamaterials. *Proc. Natl. Acad. Sci. USA* **112**, 14495–14500 (2015).
49. Yang, Z. et al. Topological acoustics. *Phys. Rev. Lett.* **114**, 114301 (2015).
50. Mittal, S. et al. Topologically robust transport of photons in a synthetic gauge field. *Phys. Rev. Lett.* **113**, 087403 (2014).
51. Ningyuan, J., Owens, C., Sommer, A., Schuster, D. & Simon, J. Time- and site-resolved dynamics in a topological circuit. *Phys. Rev. X* **5**, 021031 (2015).
52. Hasan, M. Z. & Kane, C. L. Colloquium: topological insulators. *Rev. Mod. Phys.* **82**, 3045–3067 (2010).
53. Sobolev, Y. I. et al. Solid-body trajectoids shaped to roll along desired pathways. *Nature* **620**, 310–315 (2023).
54. Elschner, J. et al. Topologically controlled synthesis of active colloidal bipeds (2023) (in preparation).
55. Michele, C. D., Gabrielli, S., Tartaglia, P. & Sciortino, F. Dynamics in the presence of attractive patchy interactions. *J. Phys. Chem. B* **110**, 8064–8079 (2006).
56. Bianchi, E., Blaak, R. & Likos, C. N. Patchy colloids: state of the art and perspectives. *Phys. Chem. Chem. Phys.* **13**, 6397–6410 (2011).
57. Yi, G.-R., Pine, D. J. & Sacanna, S. Recent progress on patchy colloids and their self-assembly. *J. Phys.: Condens. Matter* **25**, 193101 (2013).
58. Kim, Y.-J., Moon, J.-B., Hwang, H., Kim, Y. S. & Yi, G.-R. Advances in colloidal building blocks: toward patchy colloidal clusters. *Adv. Mater.* **35**, 2203045 (2022).
59. Geerts, N. & Eiser, E. DNA-functionalized colloids: physical properties and applications. *Soft Matter* **6**, 4647–4660 (2010).
60. Michele, L. D. et al. Multistep kinetic self-assembly of DNA-coated colloids. *Nat. Commun.* **4**, 2007 (2013).
61. Shelke, Y. et al. Flexible colloidal molecules with directional bonds and controlled flexibility. *ACS Nano* **17**, 12234–12246 (2023).
62. Hernandez, C. J. & Mason, T. G. Colloidal alphabet soup: monodisperse dispersions of shape-designed LithoParticles. *J. Phys. Chem. C* **111**, 4477–4480 (2007).
63. Sacanna, S., Pine, D. J. & Yi, G.-R. Engineering shape: the novel geometries of colloidal self-assembly. *Soft Matter* **9**, 8096–8106 (2013).
64. de las Heras, D., Zimmermann, T., Sammüller, F., Hermann, S. & Schmidt, M. Perspective: how to overcome dynamical density functional theory. *J. Phys.: Condens. Matter* **35**, 271501 (2023).

65. Leyva, S. G., Stoop, R. L., Pagonabarraga, I. & Tierno, P. Hydrodynamic synchronization and clustering in ratcheting colloidal matter. *Sci. Adv.* **8**, eabo4546 (2022).
66. Sammüller, F. & Schmidt, M. Adaptive Brownian dynamics. *J. Chem. Phys.* **155**, 134107 (2021).
67. Stuhlmüller, N. C. X. Drawing with colloids. *Zenodo* https://doi.org/10.5281/zenodo.8413928 (2023).
68. Kuświk, P. et al. Colloidal domain lithography in multilayers with perpendicular anisotropy: an experimental study and micromagnetic simulations. *Nanotechnology* **23**, 475303 (2012).
69. Lengemann, D., Engel, D. & Ehresmann, A. Plasma ion source for in situ ion bombardment in a soft x-ray magnetic scattering diffractometer. *Rev. Sci. Instrum.* **83**, 053303 (2012).
70. Chappert, C. et al. Planar patterned magnetic media obtained by ion irradiation. *Science* **280**, 1919–1922 (1998).
71. Urbaniak, M. et al. Domain-wall movement control in Co/Au multilayers by he^+-ion-bombardment-induced lateral coercivity gradients. *Phys. Rev. Lett.* **105**, 067202 (2010).
72. Kuświk, P. et al. Colloidal domain lithography for regularly arranged artificial magnetic out-of-plane monodomains in Au/Co/Au layers. *Nanotechnology* **22**, 095302 (2011).
73. Jarosz, A., Holzinger, D., Urbaniak, M., Ehresmann, A. & Stobiecki, F. Manipulation of superparamagnetic beads on patterned Au/Co/Au multilayers with perpendicular magnetic anisotropy. *J. Appl. Phys.* **120**, 084506 (2016).
74. Bowick, M. J. & Giomi, L. Two-dimensional matter: order, curvature and defects. *Adv. Phys.* **58**, 449–563 (2009).
75. Krita (Krita foundation, accessed June 2023) https://krita.org/.
76. Olson, E. On computing the average orientation of vectors and lines. In *2011 IEEE International Conference on Robotics and Automation*, 3869–3874 (IEEE, Shanghai, China, 2011). https://doi.org/10.1109/ICRA.2011.5979562.

Acknowledgements
We thank Adrian Ernst for helping us to transfer the loops from the simulations to the experiment. We acknowledge funding by the Deutsche Forschungsgemeinschaft (DFG, German Research Foundation) under project numbers 440764520 (T.M.F. and D.d.l.H.) and 531559581 (D.d.l.H. and T.M.F.).

Author contributions
N.C.X.S. designed the modulation loops and performed the computer simulations. F.F. performed the experiments. N.C.X.S., F.F., T.M.F., and D.d.l.H. conceptualized the research. P.K., F.S., and M.U. produced the magnetic film. S.A. and Ar.E. performed the fabrication of the micromagnetic domain patterns within the magnetic thin film. N.C.X.S., T.M.F., and D.d.l.H. designed the patterns and wrote the manuscript. All authors contributed to the different revision stages of the manuscript.

Funding
Open Access funding enabled and organized by Projekt DEAL.

Competing interests
The authors declare no competing interests.

Additional information
Supplementary information The online version contains supplementary material available at https://doi.org/10.1038/s41467-023-43390-0.

Correspondence and requests for materials should be addressed to Daniel de las Heras.

Peer review information *Nature Communications* thanks Pietro Tierno and the other anonymous reviewer(s) for their contribution to the peer review of this work. A peer review file is available.

Publication 1

Supporting Information

Supplementary Information
Simultaneous and independent topological control of identical microparticles in non-periodic energy landscapes

Nico C. X. Stuhlmüller,[1] Farzaneh Farrokhzad,[2] Piotr Kuświk,[3] Feliks Stobiecki,[3] Maciej Urbaniak,[3] Sapida Akhundzada,[4] Arno Ehresmann,[4] Thomas M. Fischer,[2] and Daniel de las Heras[1, *]

[1] *Theoretische Physik II, Physikalisches Institut, Universität Bayreuth, D-95440 Bayreuth, Germany*
[2] *Experimatalphysik X, Physikalisches Institut, Universität Bayreuth, D-95440 Bayreuth, Germany*
[3] *Institute of Molecular Physics, Polish Academy of Sciences, 60-179 Poznań, Poland*
[4] *Institute of Physics and Center for Interdisciplinary Nanostructure Science and Technology (CINSaT), University of Kassel, D-34132 Kassel, Germany*

(Dated: November 7, 2023)

SUPPLEMENTARY NOTE 1
SIMPLE PATTERNS AND SIMPLE LOOPS

We summarize here the topological transport control of isotropic magnetic colloidal particles above periodic magnetic patterns. A sketch of the system and the different types of periodic patterns is shown in Supplemental Fig. 1. Detailed theoretical and experimental studies can be found in Refs. [1–3]. For a given orientation of the external magnetic field, there is in general at least one minimum of the magnetic potential per Wigner-Seitz cell. During a modulation loop, the changes in the orientation of $\mathbf{H}_{\text{ext}}$ are slow enough such that the colloidal particles can follow a minimum of the magnetic potential at every time. In this sense the colloidal motion is adiabatic except if the minimum that transports a particles disappears (e.g. due to the annihilation with a saddle point). In such cases, the colloidal particle performs a ratchet motion towards a minimum nearby.

To control the colloidal transport we therefore need to understand the stationary points of the magnetic potential. The position of the minima in action space depends on the orientation of $\mathbf{H}_{\text{ext}}$ and on the symmetry of the pattern. By analysing the eigenvectors and the eigenvalues of the Hessian matrix of the magnetic potential, it turns out [1–3] that action space can be split into allowed and forbidden regions for the colloidal particles, see Supplemental Fig. 2. For each space point in an allowed region it is always possible to find an orientation of $\mathbf{H}_{\text{ext}}$ such that the magnetic potential is a minimum. Note also that a minimum of V_{mag} can be transformed into a maximum by simply inverting the external field since $V_{\text{mag}} \propto \mathbf{H}_{\text{p}} \cdot \mathbf{H}_{\text{ext}}$. Hence both minima and maxima of V_{mag} can be found in the allowed regions. For each space point in a forbidden region, there is an orientation of $\mathbf{H}_{\text{ext}}$ such that the magnetic potential is a saddle point, but never a minimum.

The boundary between the allowed and the forbidden regions are the fences. The location of the fences in both action space and control space depend on the symmetry of the pattern. In a square pattern, the fences in $\mathcal{C}$ are four equidistant points on the equator, see Supplemental Fig. 1(a). In hexagonal patterns however the fences are curves, the shape and the position of which vary with the symmetry phase ϕ, Supplemental Fig. 1(c). Crucially, in hexagonal patterns the fences of a given pattern and its corresponding inverse pattern (opposite magnetization) do not coincide in control space, cf. the top and the bottom patterns in Supplemental Fig. 1(c). As we discuss now, this means that the transport in a given pattern and its inverse pattern can be independently controlled with a single modulation loop.

The position of the fences is relevant to control the colloidal motion, which in action space occurs through the allowed regions. Two adjacent allowed regions are connected via points that we refer to as the gates, see Supplemental Fig. 2. To adiabatically transport a particle from one allowed region to an adjacent allowed region, we need to modulate $\mathbf{H}_{\text{ext}}$ in $\mathcal{C}$ such that a minimum of the potential crosses the gate that connects both regions. To induce transport between two consecutive Wigner-Seitz cells using closed modulation loops in $\mathcal{C}$, the loop in $\mathcal{C}$ needs to be such that the particle crosses two different gates once the loop returns to its initial position. In square patterns such loops are those that wind around the fence points [2, 3] in $\mathcal{C}$, see an example in Supplemental Fig. 2(a). In hexagonal patterns, the fences in $\mathcal{C}$ are curves made of twelve segments. Two fence segments in $\mathcal{C}$ meet at a bifurcation point. The loops that induce transport in hexagonal patterns are those that wind around at least three consecutive bifurcation points of the fences [1, 3] (enclosing therefore at least two consecutive fence segments). The bifurcation points are indicated

* delasheras.daniel@gmail.com; www.danieldelasheras.com

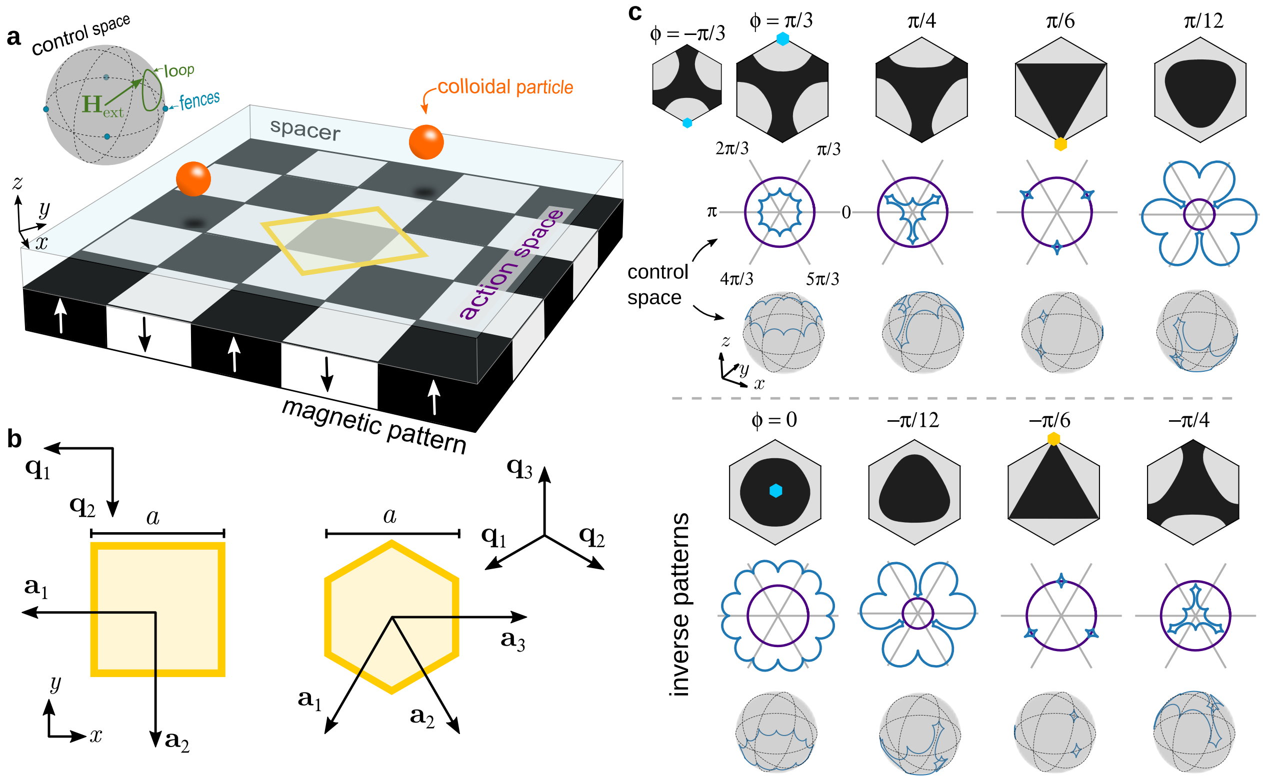

Supplementary Fig. 1. **Setup and magnetic patterns.** (a) Sketch of the system: a square magnetic pattern with domains of positive (black) and negative (white) magnetization parallel to the normal of the pattern. A Wigner-Seitz cell is highlighted in yellow. Identical colloidal particles are located above the pattern. A spacer restricts the particle motion to action space $\mathcal{A}$, a plane parallel to the pattern. An external magnetic field $\mathbf{H}_{\text{ext}}$ spatially uniform (green arrow) drives the motion via closed loops (green loop) of its orientation in control space $\mathcal{C}$ (sphere). The fences in $\mathcal{C}$ are represented in blue. (b) Wigner-Seitz cells in square and hexagonal patterns. The lattice vectors $\mathbf{a}_i$ and the wave vectors $\mathbf{q}_i$ are also shown. The magnitude of the lattice vectors is a. In the experiments $a = 14\,\mu$m. (c) Magnetization of Wigner-Seitz cells and corresponding control spaces in a family of hexagonal patterns with varying symmetry phase ϕ, as indicated. The fences are represented in blue. The control space is represented via a sphere and also using a stereographic projection in which the equator is represented as a violet circle. The patterns in the bottom row have the inverse magnetization than those in the upper row and the unit cell is also shifted. The yellow and the blue hexagons indicate the position of points with S_6 and C_6 symmetry, respectively.

in Supplemental Fig. 2(b) and Supplemental Fig. 2(c) for patterns with C_6 and S_6 symmetries, respectively, together with illustrative examples of loops that induce transport.

The simplest but non-trivial modulation loops that induce net motion are those that transport the particles along the symmetry directions of the pattern. These are given by lattice vectors $\pm\mathbf{a}_i$ with $i = 1, \ldots, N$ and $N = 2$ ($N = 3$) in square (hexagonal) patterns, see Supplemental Fig. 1. Illustrative examples of such modulation loops are shown in Supplemental Fig. 2.

The transport in square patterns is always adiabatic, and reversing the modulation loop reverses also the direction of transport [2]. In contrast, in hexagonal patterns the transport can be either adiabatic or ratchet-like [1, 3]. In the latter case, reversing the loop does not always reverse the direction of the transport. However, the direction of the transport is in all cases deterministic and topologically protected.

The set of winding numbers of the modulation loop around the fences (square patterns) and around the bifurcation points (hexagonal patterns) is the topological invariant that protects the motion. Any two loops with the same set of winding numbers (topological invariant) will transport a particle in the same direction, even though the detailed trajectories depend of course on the particular shapes of the loops.

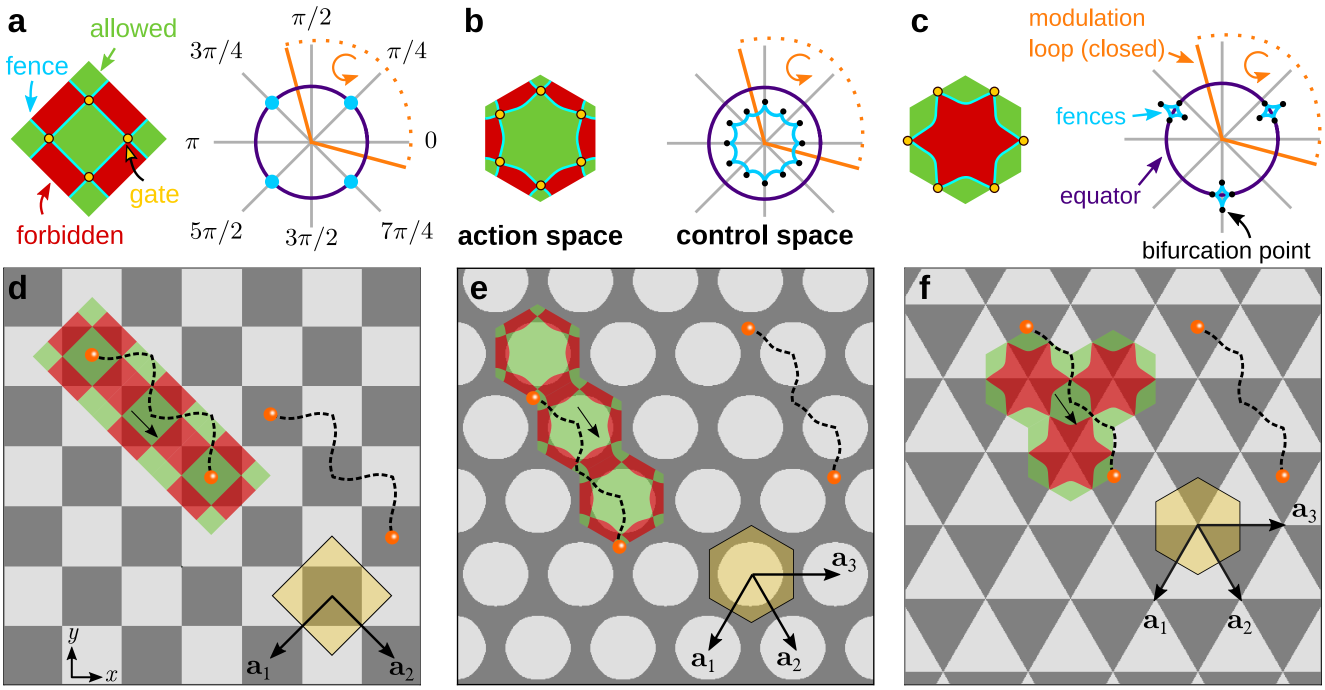

Supplementary Fig. 2. **Simple patterns and simple loops.** Action space and control space in square patterns (a) and hexagonal patterns with C_6 (b) and S_6 (c) symmetries. A unit cell illustrating the allowed (green) and forbidden (red) regions of action space, as well as the fences (blue lines) and the gates (yellow circles) is represented in each case. The control spaces (stereographic projections) show the equator (violet circle), the fences (blue), and a modulation loop (orange). The twelve bifurcation points in $\mathcal{C}$ of the fences of C_6 and S_6 patterns are also indicated with black circles. The modulation loop is the same in all cases and it is made of two segments of constant azimuthal angle joined at the north and the south poles of control space. The connection at the south pole (not visible due to the stereographic projection) is illustrated with a dotted orange segment. The loops wind anticlockwise, as indicated by the circular orange arrows. Magnetization in patterns with square (d), C_6 (e), and S_6 (f) symmetries. Black (white) regions are up (down) magnetized. The global phase is set to $\psi = \pi/4$ (d), $\psi = \pi/3$ (e), and $\psi = \pi/6$ (f). Black dashed lines are Brownian dynamics simulations of the trajectories of colloidal particles (orange circles) subjected to two consecutive modulation loops. The transport direction is indicated with black arrows. The trajectories go along the allowed regions only. A unit cell of each pattern with corresponding lattice vectors $\mathbf{a}_i$ is highlighted in yellow. For visualization purposes we have shifted the unit cells of the C_6 and the S_6 patterns with respect to those represented in Supplemental Fig. 1.

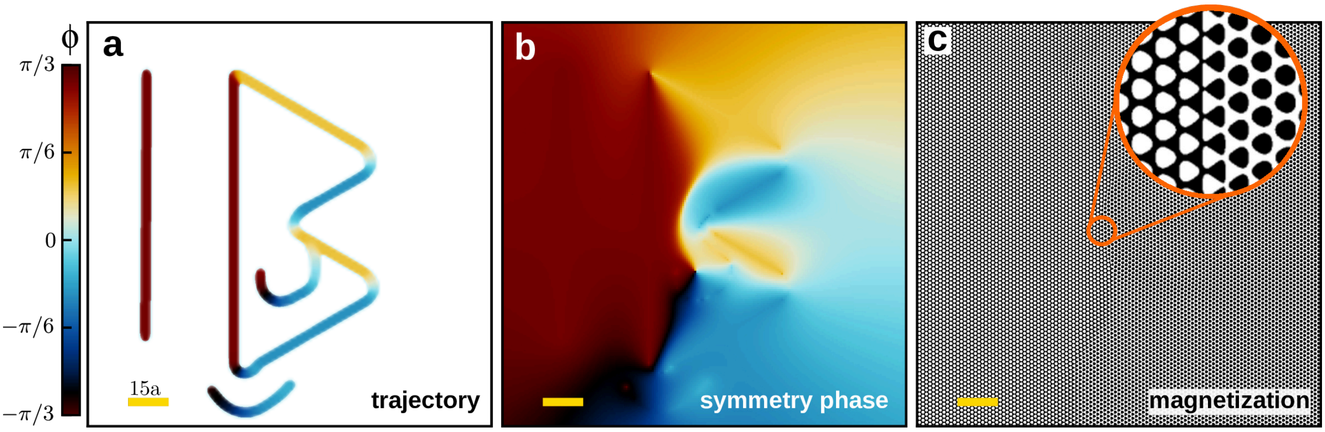

Supplementary Fig. 3. **Generation of symmetry phase modulated patterns.** (a) Trajectory drawn in Krita and colored according to the desired symmetry phase (color bar). The actual line is 1 pixel thick. Here we have made the trajectory thicker for visualization purposes. (b) Symmetry phase in the whole pattern calculated using the value of the symmetry phase along the trajectory. (c) Final magnetization of the pattern. The magnetization is positive in the black regions and negative in the white regions. The inset is a close view of a small region of the pattern, as indicated. Approximately the same region of the experimental pattern is highlighted in Fig. 4(c) of the main text. The length of the scale bars (yellow) is $15a$.

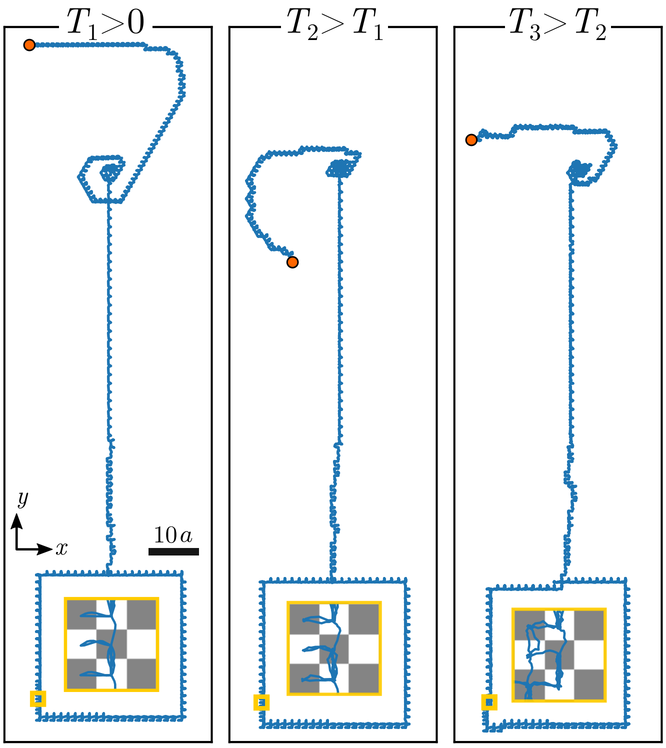

Supplementary Fig. 4. **Finite temperature effects.** Brownian dynamics simulations of colloidal particles moving above an inhomogeneous pattern at three different finite temperatures: $k_B T_1/\varepsilon \approx 3 \cdot 10^{-3}$, $k_B T_2/\varepsilon \approx 1 \cdot 10^{-2}$, and $k_B T_1/\varepsilon \approx 2 \cdot 10^{-2}$. The energy scale ϵ is the absolute value of the average external energy that a particle has when the external field points normal to the pattern. The particle trajectories are represented in blue (the starting point is indicated with an orange circle). The scale bar is $10a$. The pattern is made of two subpatterns: a top subpattern with a topological defect in the symmetry phase and a bottom subpattern with square symmetry. The insets are closed views of a small region (indicated by a yellow square) showing the trajectory (blue) and the magnetization of the pattern.

SUPPLEMENTARY REFERENCES

[1] J. Loehr, M. Loenne, A. Ernst, D. de las Heras, and T. M. Fischer, Topological protection of multiparticle dissipative transport, Nat. Commun. **7**, 11745 (2016).

[2] D. de las Heras, J. Loehr, M. Loenne, and T. M. Fischer, Topologically protected colloidal transport above a square magnetic lattice, New. J. Phys. **18**, 105009 (2016).

[3] J. Loehr, D. de las Heras, M. Loenne, J. Bugase, A. Jarosz, M. Urbaniak, F. Stobiecki, A. Tomita, R. Huhnstock, I. Koch, A. Ehresmann, D. Holzinger, and T. M. Fischer, Lattice symmetries and the topologically protected transport of colloidal particles, Soft Matter **13**, 5044 (2017).

Description of Additional Supplementary Files

Supplementary movie – Movie1.webm: A particle trap

Trajectories of colloidal particles above a pattern with a topological defect on the symmetry phase that acts as an attractor of particles.

Supplementary movie – Movie2.webm: Complex patterns and simple loops

Colloidal particles above a symmetry phase modulated pattern follow a predesigned trajectory with the shape of a B

Supplementary movie – Movie3.webm: The alphabet

Colloidal particles above rotated square patterns and subject to a complex loop follow trajectories writing the first 18 letters of the alphabet.

Supplementary movie – Movie4.webm: ABCD

A side-by-side comparison between experiments and simulations of colloidal particles above square patterns that differ in their global orientation.

Supplementary movie – Movie5.webm: Complex patterns and complex loops

Three colloidal particles at unknown positions are initialized using particle traps and from them force to follow complex trajectories.

Publication 2

Topologically controlled synthesis of active colloidal bipeds

Nature Communications, 15, 5735 (2024)

Jonas Elschner[a1], **Farzaneh Farrokhzad**[a1], Piotr Kuświk[b], Maciej Urbaniak[b], Feliks Stobiecki[b], Sapida Akhundzada[c], Arno Ehresmann[c], Daniel de las Heras[a2], and Thomas M. Fischer[a1]

[a1] Experimental Physics X and [a2] Theoretical Physics II, Department of Physics, University of Bayreuth, 95447 Bayreuth, Germany.
[b] Institute of Molecular Physics, Polish Academy of Sciences, 60-179 Poznań, Poland.
[c] Institure of Physics and Center for Interdisciplinary Nanostructure Science and Technology (CINSaT), University of Kassel, Germany.

This paper shows the internal quality control of the topologically controlled synthesis of single colloidal particles to colloidal bipeds of a programmable length.

My Contribution

Jonas Elschner, I, Daniel de las Heras, and Thomas Fischer designed and performed the experiment, computed the fences and bifurcation points and lines, and wrote the manuscript with input from all the other authors. Jonas Elschner and I contributed equally in this work. Piotr Kuświk, Maciej Urbaniak, and Feliks Stobiecki produced the magnetic film. Sapida Akhundzada and Arno Ehresmann performed the fabrication of the micromagnetic metamorphic patterns within the magnetic thin film.

nature communications

Article

https://doi.org/10.1038/s41467-024-50023-7

Topologically controlled synthesis of active colloidal bipeds

Received: 9 November 2023

Accepted: 26 June 2024

Published online: 09 July 2024

Check for updates

Jonas Elschner[1], Farzaneh Farrokhzad[1], Piotr Kuświk[2], Maciej Urbaniak[2], Feliks Stobiecki[2], Sapida Akhundzada[3], Arno Ehresmann[3], Daniel de las Heras[4] & Thomas M. Fischer[1]

Topological growth control allows to produce a narrow distribution of outgrown colloidal rods with defined and adjustable length. We use an external magnetic field to assemble paramagnetic colloidal spheres into colloidal rods of a chosen length. The rods reside above a metamorphic hexagonal magnetic pattern. The periodic repetition of specific loops of the orientation of an applied external field renders paramagnetic colloidal particles and their assemblies into active bipeds that walk on the pattern. The metamorphic patterns allow the robust and controlled polymerization of single colloids to bipeds of a desired length. The colloids are exposed to this fixed external control loop that causes multiple simultaneous responses: Small bipeds and single colloidal particles interpret the external magnetic loop as an order to walk toward the active zone, where they assemble and polymerize. Outgrown bipeds interpret the same loop as an order to walk away from the active zone. The topological transition occurs solely for the growing biped and nothing is changed in the environment nor in the magnetic control loop. As in many biological systems the decision of a biped that reached its outgrown length to walk away from the reaction site is made internally, not externally.

The length of a one-dimensional passive assembly of periodically repeated units is the most important structural quantity of the assembly that determines its physical equilibrium and non-equilibrium properties. Growth control of the assembly in order to achieve the *desired length* therefore is a scientific question of immediate technological relevance in molecular[1] and supramolecular[2] polymer chemistry, for the growth of nanotubes[3] and nanowires[4] as well as in biology for the control of the length of DNA[5], for the growth of flagella[6] or for the switching from vegetative plant growth toward reproductive growth[7]. The mechanism of length control in these different systems can be via an external feedback[1,3,7], where the environment (an inhibitor, a mask, or the daylight duration via a systemic signal, called florigen) tells the growing system that the end (of polymerization time, of the mask, or of vegetative growth) has been reached. An alternative length control occurs via a balance between the growth and the decomposition kinetics[1,2,6]. A third interesting mechanism is the use of coprime repetitions of complementary single strands of DNA[5] that leads to a stop of the growth of the forming double-stranded DNA once the single strands have bound to the double-strand product length of units of the two coprime numbers. These mechanisms for external length control share the passive role of the assembly in determining when its length is long enough. An active entity, in contrast, must not be told externally but should be able to make an internal decision when its proper length has been reached.

Here, we use a topological and, therefore, robust transition of the internal interpretation of an external magnetic control loop for the control of the length of walking magnetic multi-colloidal bipeds. The bipeds actively walk on a metamorphic magnetic pattern. A metamorphic pattern is a quasi-periodic pattern with unit cells that continuously change as one moves along the pattern. Small bipeds and

[1]Experimentalphysik X, Physikalisches Institut, Universität Bayreuth, Bayreuth, Germany. [2]Institute of Molecular Physics, Polish Academy of Sciences, Poznań, Poland. [3]Institute of Physics and Center for Interdisciplinary Nanostructure Science and Technology (CINSaT), Universität Kassel, Kassel, Germany. [4]Theoretische Physik II, Physikalisches Institut, Universität Bayreuth, Bayreuth, Germany. e-mail: Thomas.Fischer@uni-bayreuth.de

single colloidal particles interpret the external magnetic loop as an order to walk from a random initial position toward the active zone, where they assemble and polymerize, while large enough bipeds interpret the same loop as an order to walk away from the active zone. The topological transition occurs solely for the growing biped and nothing is changed in the environment nor in the magnetic control loop. Hence the decision to walk away from the reaction site is made internally, not externally.

Results

Experimental setup

Paramagnetic colloidal particles (diameter $d = 2.8\,\mu$m) immersed in water are placed on top of a two-dimensional magnetic pattern. The pattern is a metamorphic hexagonal lattice of alternating regions with positive and negative magnetization relative to the direction normal to the pattern, see Fig. 1a. A uniform time-dependent external field of constant magnitude is superimposed to the non-uniform time-independent magnetic field generated by the pattern. The external field induces strong dipolar interactions between the colloidal particles which respond by self-assembling into bipeds of n^* particles, provided sufficient single colloidal particles are available[8].

In Fig. 1b we show the orientation of the external field $\boldsymbol{H}_{\text{ext}}$ (black) of fixed magnitude that adiabatically varies along a closed loop in control space $\mathcal{C}$ – a sphere of radius H_{ext}. Despite the field returning to its initial direction, single colloidal particles can be topologically transported by one unit cell after completion of one loop[9–11]. Their transport is topologically protected but passive in the sense that they are carried along in the moving local minimum of the potential. There exist an entire family of periodic hexagonal patterns. Each pattern in this family is characterized by a specific value of a symmetry phase[12]. The transport in an unmorphed periodic hexagonal pattern occurs provided that the loop winds around specific orientations of the external field called bifurcation points that depend on the symmetry phase of the pattern. In our metamorphic pattern, the symmetry phase varies with the location on the pattern, and this allows us to use well-designed loops where single colloids are transported in different directions in different regions of the metamorphic pattern[13]. Colloidal bipeds formed by several particles can also be transported[8,14]. The biped aligns with the external field since dipolar interactions are stronger than the buoyancy. Hence, if the external field is not parallel to the pattern, one end of the biped (a foot) remains on the ground while the other one is lifted. As a result the bipeds actively walk by alternatingly grounding one of their feet. In addition, as for the single colloids, the grounded foot passively slides above the pattern[8,14,15].

To transport the bipeds, the loop also needs to wind around special orientations of the external field that depend on the length of the bipeds and on the pattern's symmetry phase. Bipeds of different lengths can fall into different topological classes such that their displacement upon completion of one loop can be different in both magnitude and direction. A sketch of the process is shown in Fig. 1. As it is the case for single colloids, the biped motion is topologically protected and hence, robust against perturbations.

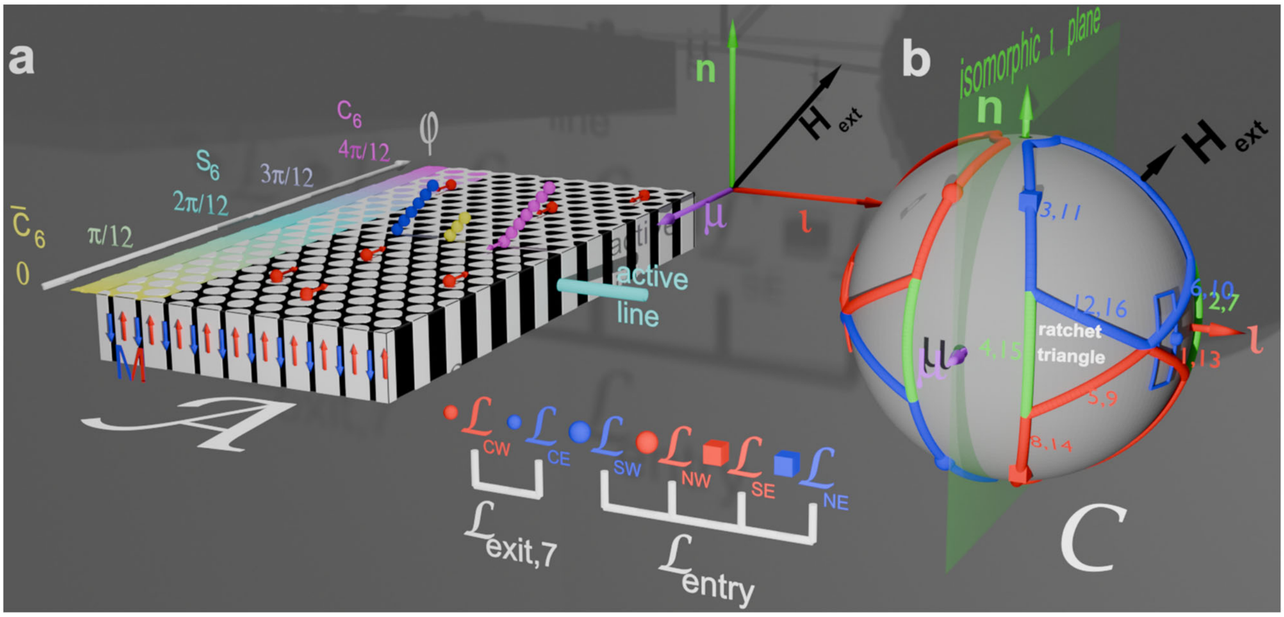

Fig. 1 | Schematic of the setup. a A metamorphic hexagonal magnetic pattern consists of domains of positive (white) and negative (black or colored) magnetization parallel to the normal vector of the pattern **n**. Along the metamorphic $\boldsymbol{\mu}$-direction the pattern morphs from a hexagonal C_6 pattern with down magnetized circular bubble domains via an improper six-fold symmetric S_6-pattern to a hexagonal $\bar{C}_6$ bubble pattern with up magnetized bubbles. Along the isomorphic $\boldsymbol{\iota}$-direction the pattern remains periodic. The vectors $\mathbf{n}, \boldsymbol{\mu}$ and $\boldsymbol{\iota}$ are not drawn to scale. Colloidal particles (red) are placed on top of the pattern immersed in water. Due to the presence of a strong homogeneous external field (black), some colloids self-assemble into bipeds of juvenile (yellow or blue) and outgrown (magenta) length. The $2d$-space where the colloids move is called the action space $\mathcal{A}$. **b** Our control space $\mathcal{C}$ is a sphere that represents all possible directions of the external field $\mathbf{H}_{\text{ext}}$ (black). The direction of the external field varies in time, performing a loop $\mathcal{L} = \mathcal{L}_{entry} * \mathcal{L}_{exit}$ (a closed path) that is a concatenation of a (thicker) entry loop $\mathcal{L}_{entry}$ and a (thinner) exit loop $\mathcal{L}_{exit}$. Both loops consist of sub-loops revolving in the mathematical positive (blue) and negative (red) sense. The sub-loops consist of segments (open paths) that connect different corners of the sub-loop where the direction of the loop changes. The time sequence of consecutive segments of the eastern part of the entry loop is indicated by numbers shown with the loop segments. The black arrow tip on the loop corresponds to the orientation of the external field depicted in (**a**). The loops are eigen loops of the σ_ι mirror operation and, therefore, suppress any net motion into the isomorphic $\boldsymbol{\iota}$-direction. At any time during the modulation the orientation of the bipeds in (**a**) is parallel to the orientation of the external magnetic field $\mathbf{H}_{\text{ext}}$. Bipeds in (**a**) and the orientation of $\mathbf{H}_{\text{ext}}$ in (**b**) are shown at the same time. We find entry loops that transport single colloids and small bipeds toward the active line (cyan) on the S_6 isomorphic line of the pattern. The bipeds grow in this region via dipolar attraction due to the high particle density. Once they have reached the outgrown length (see magenta biped) encoded by our control exit loop, the bipeds topologically change and reinterpret the same control loop as a command to walk away from the S_6 region into the metamorphic $\boldsymbol{\mu}$-direction. The loop $\mathcal{L}_{CW}$ is not visible in the figure but is a mirror image of the loop $\mathcal{L}_{CE}$ mirrored at the isomorphic ι-plane. We show it in Supplementary Video 1, where we record the scheme from different perspectives.

In this work we show that one can apply external field modulations that act in synergy with the metamorphic pattern to synthesize bipeds of a chosen length. The choice of metamorphic pattern and external field modulation must be such that single colloidal particles and bipeds of different length all fall into the wanted topological transport class at each of the different locations.

Metamorphic pattern

We choose a pattern with a thin film of magnetization

$$\mathbf{M} = M\delta(qz)\mathbf{n}\,\mathrm{sign}\left(\frac{1}{2}\cos(3\varphi) + \sum_{i=0}^{2}\cos(\mathbf{q}_i \cdot \mathbf{r}_{\mathcal{A}} - \varphi)\right) \tag{1}$$

where $\mathbf{r}_{\mathcal{A}}$ is the two-dimensional vector in action space $\mathcal{A}$, which is the plane parallel to the pattern where the colloids move. The modulus of the saturation magnetization is denoted by M, $\mathbf{n}$ is the vector normal to the film, the z coordinate runs in the direction of $\mathbf{n}$ and φ is the symmetry phase. If we fix the symmetry phase ($\nabla_{\mathcal{A}}\varphi = 0$) the pattern is a periodic hexagonal pattern of period a (in our experiments $a = 7\,\mu$m). The vectors $\mathbf{q}_i = \frac{2\pi}{a \sin \pi/3}\mathbf{R}^i_{2\pi/3} \cdot \mathbf{e}_x$, $(i = 0, 1, 2)$, are three coplanar reciprocal unit vectors, and $\mathbf{R}_{2\pi/3}$ is a rotation matrix around the normal vector $\mathbf{n}$ by $2\pi/3$. The modulus q of all three in-plane reciprocal unit vectors is the same.

If we render the symmetry phase $\varphi(\mathbf{r}_{\mathcal{A}})$ a function of action space this breaks the discrete translational symmetry. In our case we use a linear variation of the symmetry phase

$$\varphi = \frac{\pi}{3} + \boldsymbol{\mu} \cdot \mathbf{r}_{\mathcal{A}} \tag{2}$$

with a small and fixed morphing reciprocal vector $\boldsymbol{\mu} = -\boldsymbol{q}_0/240$ of modulus $\mu \ll q$. Due to the small value of the morphing reciprocal vector, the lattice adiabatically morphs from one locally periodic pattern shape to the next as we move along the metamorphic $\boldsymbol{\mu}$-direction, see Fig. 1a. At the origin, the local pattern resembles a C_6 symmetric pattern (see magenta region in Fig. 1a, $\varphi \approx 4\pi/12$) with hexagonally arranged downward magnetized domains. When we move in the metamorphic direction, the local pattern morphs into an S_6-symmetric pattern at $\varphi \approx 2\pi/12$ with triangular upward-magnetized domains neighbored by oppositely oriented (cyan) down-magnetized domains. When the symmetry phase decreases to $\varphi \approx 0$, the local pattern resumes a local $\bar{C}_6$-symmetry with hexagonally arranged (white) upward magnetized domains in an extended downward (yellow) surrounding. The bar above the $\bar{C}_6$-symmetry indicates that the pattern is inverted with respect to the C_6-case, i.e., $\varphi \approx 4\pi/12$. At a symmetry phase of $\varphi \approx 6\pi/12$ (not shown), the symmetry is $\bar{S}_6$ with inverted triangles compared to the $2\pi/12$-case. Iso-phase lines run along the isomorphic vector $\boldsymbol{\iota}$, the periodic direction of the pattern with translation symmetry modulo the primitive unit vector $\boldsymbol{a}_1$.

In analogy to the active site of an enzyme, we call the iso-phase line with locally S_6-symmetric pattern at $\varphi = 2\pi/12$ the active line (cyan in Fig. 1a). The active line serves as a polymerization line for monomeric single colloidal particles into polymeric bipeds being rods of several colloidal spheres. The bond between the monomers of the polymerized bipeds is a physical dipolar interaction bond and not a chemical bond. The concentration of colloids outside the active region must be small enough to prevent polymerization reactions outside the active zone; polymerization addition reactions shall only occur in the active zone. There, our modulation loop will ensure that the reaction proceeds toward the wanted outgrown biped length and not toward unwanted longer biped lengths. Juvenile bipeds having lengths below the outgrown length shall not leave the active zone before they are outgrown.

Modulation loop

In Fig. 1b we show the control space $\mathcal{C}$ and the modulation loop controlling the dynamic assembly of single colloidal particles toward an outgrown biped of length $b_{n^*} = b_7 = 7d$, where d is the diameter of a single colloidal particle. The loop $\mathcal{L} = \mathcal{L}_{entry}{}^*\mathcal{L}_{exit}$ is a concatenation of two loops: a (thick) entry loop $\mathcal{L}_{entry}$ and a (thin) exit loop $\mathcal{L}_{exit}$. The entry loop consists of the north-western subloop $\mathcal{L}_{NW}$, the south-western subloop $\mathcal{L}_{SW}$, the north-eastern subloop $\mathcal{L}_{NE}$, and the south-eastern subloop $\mathcal{L}_{SE}$. They wind in the mathematically positive (blue) and the mathematically negative (red) sense. Furthermore, we make use of (green) detour segments that we move along in both directions. The sequence of consecutive segments of the eastern part of the entry loop follows the numbers attached in Fig. 1b to each segment of the loop. The entry loop is an eigen loop $\mathcal{L}_{entry} = \sigma_n(\mathcal{L}_{entry}) = \sigma_\iota(\mathcal{L}_{entry})$ to the mirror operations reflecting at the equatorial $\boldsymbol{n}$- and the isomorphic $\boldsymbol{\iota}$-plane, and the sequence of segments of the western part of $\mathcal{L}_{entry}$ can be inferred from the σ_ι mirror symmetry.

The green loop segments of the concatenated eastern loop $\mathcal{L}_{NE}{}^*\mathcal{L}_{SE}$ correspond to the convex envelope of the eastern loop. The entry loop sequence in Fig. 1b is such that the north-eastern loop $\mathcal{L}_{NE}$ and the south-eastern loop are alternately extended each by one or the other of the (red, blue, green) triangles that, for reasons that will become clear later we call the ratchet triangles.

The exit loop $\mathcal{L}_{exit}$ consists of the two (thin) subloops $\mathcal{L}_{CW}$ and $\mathcal{L}_{CE}$. The exit loop $\mathcal{L}_{exit} = \sigma_\iota(\mathcal{L}_{exit})$ shares the mirror symmetry at the $\boldsymbol{\iota}$-plane with the entry loop (see the loop in the Supplementary Video 1). However, in contrast to the entry loop, its reflection at the $\boldsymbol{n}$-plane yields the inverse (time-reversed) exit loop $\mathcal{L}^{-1}_{exit} = \sigma_n(\mathcal{L}_{exit})$. We use the exit loop to move bipeds of the outgrown length b_{n^*} out of the active zone. In the experiments we use six different exit loops $\mathcal{L}_{exit,n^*}$, with $n^* = 2, 3, 4, 5, 6, 7$, depending on the outgrown biped length b_{n^*} that we intend to synthesize. In Fig. 1b we show the exit loop $\mathcal{L}_{exit,7}$ that is designed to produce bipeds of length b_7. Like the exit loop $\mathcal{L}_{exit,7}$ four of the other exit loops $\mathcal{L}_{exit,n^*}$, with $n^* = 2, 3, 5, 6$, also circle two $\boldsymbol{\iota}$-symmetric centers each. Their centers are, however, at positions on the equator different from that of $\mathcal{L}_{exit,7}$ and their azimuthal width is broader, the smaller the desired length b_{n^*} to be synthesized.

Synthesis of b_3-bipeds

We can design loops to grow bipeds of arbitrary length (for practical size limits see the discussion section). As an illustration, we have depicted four reflection microscopy snapshots in Fig. 2a, showing the colloidal particles on the metamorphic pattern subject to the loop $\mathcal{L} = \mathcal{L}_{entry}{}^*\mathcal{L}_{exit,3}$ of period T at different times. Six red single colloidal particles, one of them not yet in the field of view, are transported consecutively toward the S_6 symmetric region as a result of the loop. Two of these particles hop back and forth until a polymer addition reaction assembles them into an orange juvenile b_2-biped (time $t = 1.2\,T$). The juvenile biped waits in the active zone until a third red single colloidal particle is brought into the reaction zone. One further addition reaction leads to a yellow outgrown $b_{n^*} = b_3$ biped at $t = 2\,T$. The outgrown biped of length b_3 is transported into the metamorphic $\boldsymbol{\mu}$-direction as soon as it reaches its outgrown length. During the entire process (from $t = 0$ to $t = 3.5\,T$) two further single colloidal particles are approaching the active zone and will assemble to a second biped (shown in Supplementary Video 3 but not shown in Fig. 2a). In Fig. 2b and c we plot the tracked metamorphic and isomorphic coordinate of the single colloids respectively the metamorphic and isomorphic coordinate of the northern foot of the bipeds as a function of time. While the isomorphic coordinates in Fig. 2c are purely periodic with the period of the loop (indicated by the shading of the background), the metamorphic coordinates of all single colloids in Fig. 2b are aperiodic and progressively approach the S_6-active line from either side. Once in the active zone, the motion of the colloids switches to

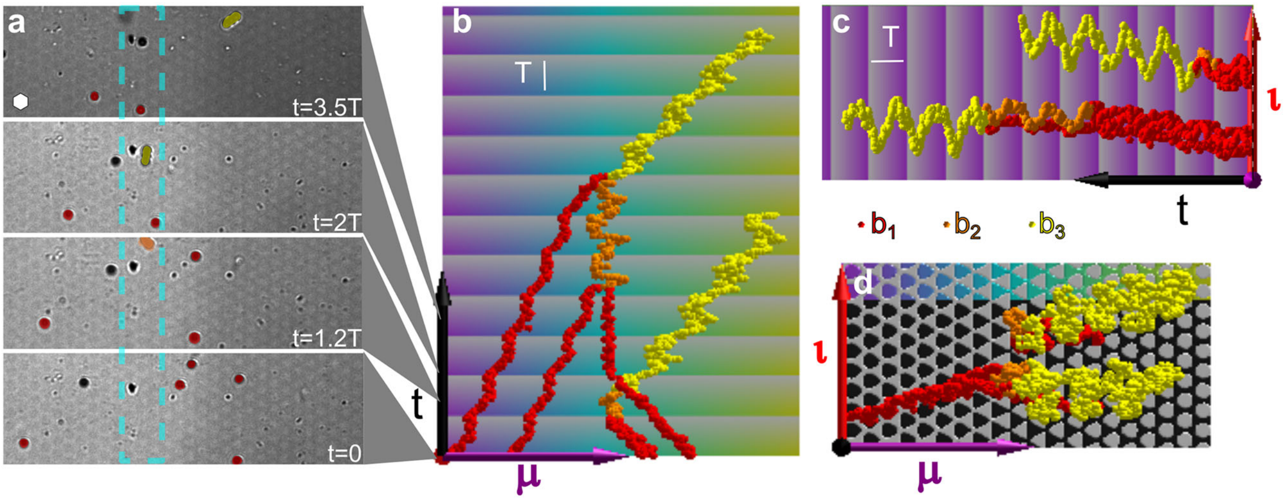

Fig. 2 | b_3-synthesis. a Four reflection microscopy images of the colloidal particles above the pattern subject to the loop $\mathcal{L} = \mathcal{L}_{entry}{}^*\mathcal{L}_{exit,3}$ of period T. The hexagonal unit cell of the pattern (white hexagon) has lattice constant $a = 7$ µm. The images show the synthesis and transport of the first (yellow) b_3 biped as well as the collection of single bipeds (red) in preparation of the second b_3 biped. The active zone is marked in cyan. **b** Trajectories of single colloidal particles and bipeds (colored according to their length b_n) as a function of the time t and the metamorphic coordinate $\boldsymbol{\mu}$. The background is colored according to the symmetry phase in the metamorphic direction, and the brightness of the background is periodic with the period T of the modulation loop. **c** Trajectories of single colloidal particles and bipeds as a function of the time t and the isomorphic coordinate $\boldsymbol{\iota}$. **d** Trajectories of single colloidal particles and bipeds as a function of the metamorphic coordinate and the isomorphic coordinate. The background shows the magnetization pattern of the magnetic thin film. Supplementary Video 3 of the synthesis of two b_3-bipeds is provided with the supplementary information.

periodic until the motion is disrupted by a polymerization addition event. Finally, after the outgrown length b_3 is reached, the b_3-bipeds walk away into the positive metamorphic $\boldsymbol{\mu}$-direction until they leave the field of view of the microscope. The trajectories are depicted above the pattern in Fig. 2d as a function of the isomorphic and metamorphic coordinates. We can see that the active line of polymerization is indeed at the S_6-symmetric line of the pattern. Supplementary Video 3 of the synthesis of two b_3-bipeds is provided with the supplementary information.

Synthesis of b_7-bipeds

In Fig. 3a and b, we show the two reflection microscopy snapshots of the colloidal particles on the metamorphic pattern subject to the loop $\mathcal{L} = \mathcal{L}_{entry}{}^*\mathcal{L}_{exit,7}$ at times $t = 0$ and $t = 7\,T$. In Fig. 3c and d we plot the tracked metamorphic and isomorphic coordinates of the single colloids respectively the metamorphic and isomorphic coordinates of the northern foot of the bipeds as a function of time. Figure 3e shows the trajectories above the pattern for the two in-plane directions. The motion is similar to that in Fig. 2. The only difference is that juvenile bipeds $b_n < b_7$ now remain in the active zone until they have reached their newly set outgrown length of $b_{n^*} = b_7$ before they leave this region and walk away into the metamorphic $\boldsymbol{\mu}$-direction. Figure 3 shows one unsuccessful and two successful synthesis attempts. In the unsuccessful attempt, a b_6-biped (blue) is synthesized in the active zone. The lonely b_6-biped, however, is unsuccessful in attracting a final colloidal particle to reach the outgrown (magenta) $b_{n^*} = b_7$ length that would allow it to exit the active zone. In contrast to its successfully outgrown b_7-bipeds in the neighborhood, the b_6-biped continues its lonely back-and-forth walk inside the active zone without ever being allowed to leave. The topological constraint robustly keeps the b_6-biped inside the active zone. Supplementary Video 7 of the synthesis of one b_6-biped and two b_7-bipeds is provided with the supplementary information.

Synthesis of b_2, b_4, b_5, and b_6-bipeds

We have also used four further exit loops $\mathcal{L}_{exit,n^*}$ to synthesize outgrown bipeds of length b_{n^*} for $n^* = 2, 4, 5, 6$. Four videoclips: Supplementary Video 2, Supplementary Video 4, Supplementary Video 5, and Supplementary Video 6 are provided with the supplementary information. Details of the loops $\mathcal{L}_{exit,n^*}$ are provided in the methods section. For $n^* = 2$ one outgrown b_2-biped already occupies the active zone, a second is synthesized there, both are transported away, and five single colloidal particles remain in the active zone; for $n^* = 4$ two outgrown b_4-bipeds are synthesized in the active zone, transported away, and two single colloidal particles remain in the active zone; for $n^* = 5$ three outgrown b_5-bipeds are synthesized in the active zone, transported away, and one juvenile b_3-biped remains in the active zone; and for $n^* = 6$ one outgrown b_6-biped is synthesized in the active zone, transported away, and three single colloidal particles remain in the active zone. For any biped lengths, there are, in principle exit loops leaving juvenile bipeds in the active zone and transporting outgrown bipeds out of the active zone. The robustness of such loops, however, decreases with the biped length and whenever the biped length becomes commensurate with the lattice. Also, the period T leading to adiabatic behavior increases with the desired outgrown biped length.

Theoretical results

We have experimentally shown that the application of the loop $\mathcal{L}$ in control space to a collection of single colloidal particles on the metamorphic pattern successfully and without external interference collects single colloidal particles at the active line, adds them to juvenile bipeds and finally transports them into the metamorphic direction once they have reached their outgrown length b_{n^*}.

The rest of this work theoretically proves the topological nature of the programmed outgrown synthesis and explains the topology behind the design of the loops as well as the topological response of the colloidal assemblies to those loops in the different regions of action space.

Single colloidal particle response

In Fig. 4 we replot the magnetic pattern in action space $\mathcal{A}$ together with copies of the control spaces of single colloidal particles for the locally periodic regions for seven symmetry phases. The single colloidal

 https://doi.org/10.1038/s41467-024-50023-7

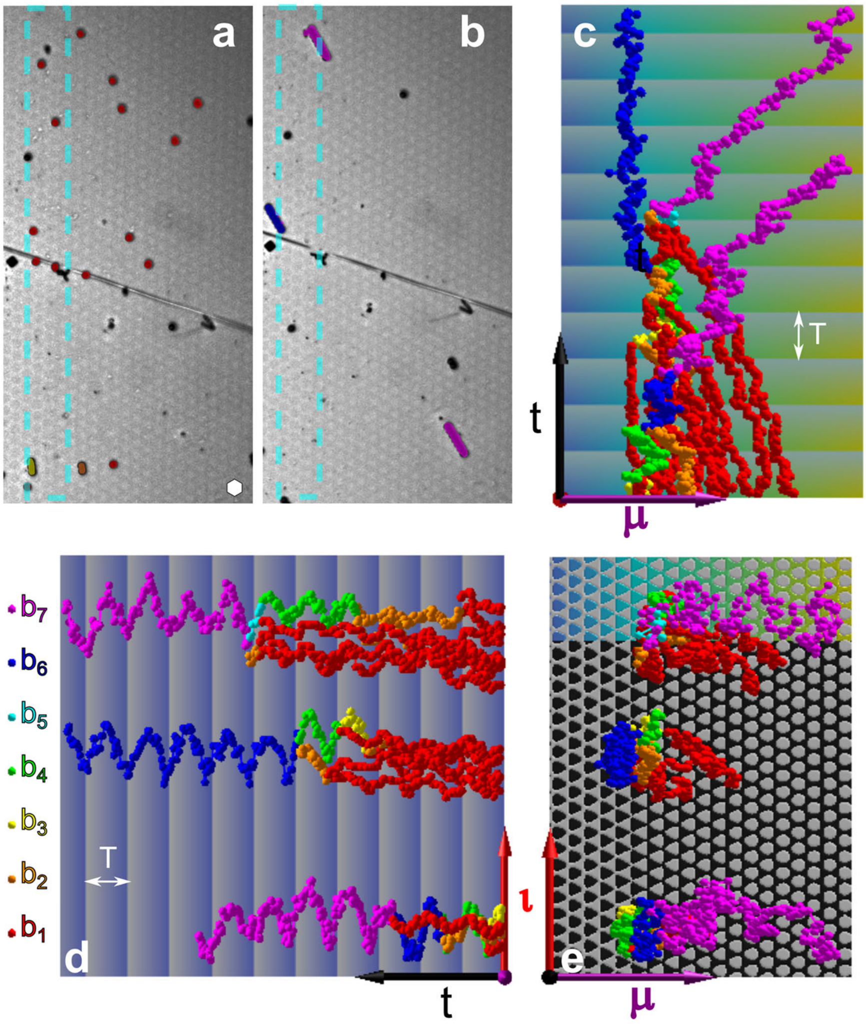

Fig. 3 | b_7-synthesis. Two reflection microscopy images at the beginning $t = 0$ (**a**) and after 7 loops $t \approx 7T$ (**b**) of the colloidal particles (colored according to the biped length) above the pattern subject to the loop $\mathcal{L} = \mathcal{L}_{entry}{}^*\mathcal{L}_{exit,7}$. The hexagonal unit cell of the pattern (white hexagon) has lattice constant $a = 7$ μm. The active zone is marked in cyan. **c** Trajectories of single colloidal particles and bipeds (colored according to their length b_n) as a function of the time t and the metamorphic coordinate. The background is colored according to the symmetry phase in the metamorphic direction, and the brightness of the background is periodic with the period T of the modulation loop. **d** Trajectories of single colloidal particles and bipeds as a function of the time t and the isomorphic coordinate. **e** Trajectories of single colloidal particles and bipeds as a function of the metamorphic coordinate and the isomorphic coordinate. The background shows the magnetization pattern of the magnetic thin film. Supplementary Video 7 of the synthesis of one b_6-biped and two b_7-bipeds is provided with the supplementary information.

particle control spaces are colored according to the location in action space and they are placed right above the corresponding region in action space. A larger gray copy of the control space simultaneously explaining the topologically protected transport anywhere in the pattern is attached as well.

For each symmetry phase, the white and black segmented fence in the control space $\mathcal{C}$ separates colored regions on the concave side of the fence from gray excess regions on the convex side of the fence. External magnetic fields pointing into the colored regions of $\mathcal{C}$ cause a colloidal potential with one minimum per unit cell in $\mathcal{A}$, while fields pointing into the gray excess regions of $\mathcal{C}$ cause a colloidal potential with two minima per unit cell in $\mathcal{A}$. The cusps of the fences where black and white segments meet are $\mathcal{B}_-$-bifurcation points. The cusps of the fences where the same colored segments meet are $\mathcal{B}_0$-bifurcation points. The fence line in $\mathcal{C}$ depends on the symmetry phase φ. For a C_6-like pattern ($\varphi = 60\pi/180$, magenta) there is one polar gray excess region fenced by twelve (white and black) segments of the fence that connect twelve bifurcation points. When decreasing the symmetry phase to $\varphi = 40\pi/180$ (bright blue), three further diamond-shaped excess regions disjoin from this polar excess region and move toward the equator of control space when the symmetry phase reaches the cyan S_6-symmetry. During the same decrease of the symmetry phase the polar excess region shrinks to a point and reappears at the opposite pole beyond the S_6-symmetric phase, recollects the diamond-shaped excess regions ($\varphi = 20\pi/180$, bright green) now in the opposite hemisphere to form a polar twelve segmented three-fold symmetric fence ($\varphi = 10\pi/180$, bright olive) that adopts the full six-fold symmetric polar shape ($\varphi = 0$, yellow) for the $\bar{C}_6$-like region in action space.

Consider an external field pointing toward a point in the colored one minimum region of control space and a colloidal particle occupying this one minimum in a unit cell of action space. When we redirect the external field in control space such that it crosses into the gray excess region, a new non-occupied (less deep) excess minimum and an excess saddle point form in the unit cell of action space. Let us call the two minima a white and a black minimum. If we enter the excess region of control space through a black (white) fence segment, the colloidal particle will occupy the black (white) minimum in action space while the excess minimum of the opposite color remains unoccupied. If one exits the gray excess region to the colored single minimum region of

 https://doi.org/10.1038/s41467-024-50023-7

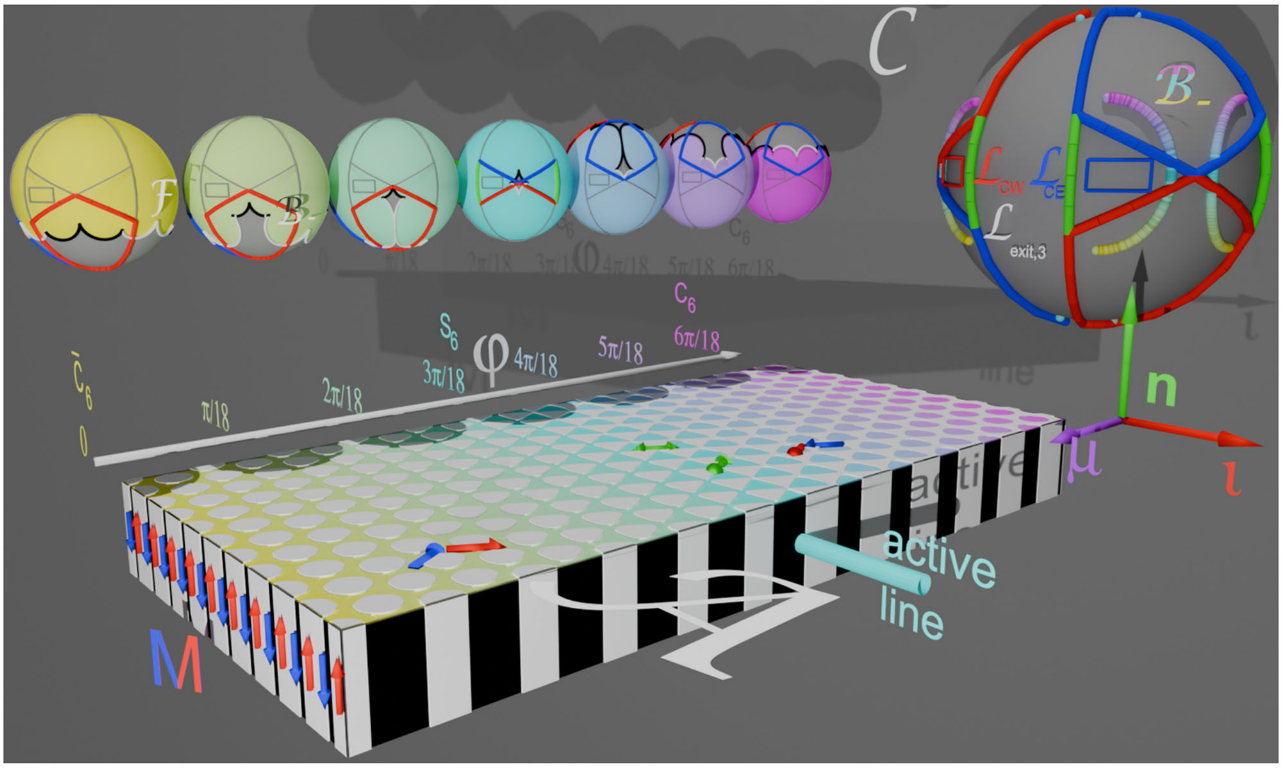

Fig. 4 | Topology of the transport for single colloidal particles. The magnetic pattern (action space $\mathcal{A}$) is colored according to the symmetry phase φ. On top of seven equally spaced regions, we place seven control spaces corresponding to the local symmetry phases in these regions. A larger gray copy of the control space summarizes what we learn from the single symmetry control spaces. It shows the (thicker) entry loop $\mathcal{L}_{entry}$ and the (thinner) exit loop $\mathcal{L}_{exit,3}$ used for the synthesis of b_3-bipeds. Both loops consist of sub-loops revolving in the mathematically positive (blue in the large copy of control space) and negative (red in the large copy of control space) sense. In the colored control spaces we show the positions of the corresponding fences $\mathcal{F}$ (white and black segments) for single colloidal particles of the corresponding symmetry phase. The fences are the external field orientations for which there are marginally stable potential minima in action space. The fences circulate around the gray excess regions where there are two minima per unit cell of the potential in action space. Cusps of the fences are bifurcation points. We distinguish $\mathcal{B}_-$-bifurcation points where black and white segments of the fence meet from $\mathcal{B}_0$-bifurcation points where similarly colored fence segments meet. Loops are colored gray in the small control spaces if they do not wind around $\mathcal{B}_-$-bifurcation points of the particular symmetry phase. These loops are topologically trivial in this region of action space. The transport direction of active topologically non-trivial loops is depicted by arrows in action space $\mathcal{A}$ using the same color as the loop. In the larger gray copy of the control space $\mathcal{B}_-$-bifurcation points join to (thick magenta-cyan-yellow) bifurcation lines when plotted as a function of the symmetry phase φ. The winding of a loop around a set of $\mathcal{B}_-$-bifurcation points determines the induced transport direction for the particular symmetry phase. As one moves through action space in the metamorphic direction $\boldsymbol{\mu}$ one eventually passes through the active (iso-phase) line. At the same time bifurcation points in control space pass from the northern part of the loop revolving in the mathematical positive (negative) sense to the southern part of the loop revolving in the opposite sense. The loops are eigen loops of the σ_ι mirror operation and, therefore, suppress any net motion into the isomorphic $\boldsymbol{\iota}$-direction. The entry loop, therefore transports single colloids and small bipeds toward the active zone on the S_6 isomorphic line of the pattern. The exit loop $\mathcal{L}_{exit,3}$ does not revolve around any of the $\mathcal{B}_-$-bifurcation points and, therefore does not transport single colloids. Supplementary Video 8 shows this figure from various perspectives.

control space via a similarly colored fence segment, the process is adiabatic, and the colloidal particle in action space remains in the same (or an equivalent) minimum as it resided upon entry of the excess region. If we exit the excess region of control space via a fence segment of opposite color, the occupied minimum disappears upon exit, and our colloidal particle performs an irreversible ratchet jump in action space toward the remaining minimum of opposite color in the same or a neighboring unit cell. There are, therefore adiabatic modulation loops that enter and exit the excess region of control space via similarly colored fence segments and irreversible ratchet loops that enter and exit via oppositely colored fence segments[10]. Black and white fence segments join in the control space at the $\mathcal{B}_-$-bifurcation points. An adiabatic (ratchet) loop must encircle an even (odd) number of $\mathcal{B}_-$-bifurcation points. Adiabatic loops that encircle a non-zero number of $\mathcal{B}_-$-bifurcation points are topologically non-trivial. Such non-trivial loops connect the one minimum in one unit cell to the one minimum of a neighboring unit cell. In order to predict the motion of a single colloidal particle it suffices to know the winding numbers of modulation loops in control space around the $\mathcal{B}_-$-bifurcation points. We, therefore, omit the fences in the larger gray copy of the control space and just plot the family of the $\mathcal{B}_-(\varphi)$-bifurcation points, colored according to the symmetry phase of the pattern.

We use one (blue) loop on the northern hemisphere $\mathcal{L}_{NE}$ circling around two $\mathcal{B}_-(\varphi)$-bifurcation points for a subset of symmetry phases $\varphi > 30\pi/180$ (blue-magenta). The loop $\mathcal{L}_{NE}$ is topologically non-trivial for this subset. After completion, the loop transports single colloids from the C_6-like region toward the S_6-symmetric region, provided that we choose the proper sense of circulation. The proper sense of circulation is found by using the rolling wheel rule: Consider a virtual wheel rolling on the pattern. The axis of the wheel is given by the averaged direction of the two $\mathcal{B}_-$ bifurcation points which the loop winds around. The direction of motion of a single colloidal particle is perpendicular to this axis and is provided by the direction that the virtual wheel rolling on the pattern below it would take if spinning around the axis with the same winding number as the loop. In action space $\mathcal{A}$ of Fig. 4 we depict the direction of transport of this loop for $\varphi > 30\pi/180$ by arrows with the same color as the loop. The loop $\mathcal{L}_{NE}$ is topologically trivial for colloids lying on the other side of the S_6-symmetry line in action space $\mathcal{A}$, ($\varphi < 30\pi/180$, yellow-green). The loop, therefore, causes no transport of colloids on this part of the action

https://doi.org/10.1038/s41467-024-50023-7

space. We therefore color $\mathcal{L}_{NE}$ in the single symmetry phase control spaces of this region in gray.

In order to transport single colloidal particles from the other side of the active S_6-symmetry line, we use a second (red) south-eastern, loop $\mathcal{L}_{SE} = \sigma_n(\mathcal{L}_{NE})$ being a mirror image of the north-eastern loop mirrored at the equatorial plane. $\mathcal{L}_{SE}$ lies on the southern hemisphere and circulates in the opposite sense around the $\mathcal{B}\_(\varphi)$-bifurcation points beyond the S_6-symmetry ($\varphi < 30\pi/180$, yellow-green). In the region $\varphi > 30\pi/180$ (blue-magenta) $\mathcal{L}_{SE}$ is topologically trivial (and therefore colored gray in the corresponding control spaces). The southeastern loop therefore, transports single colloids in $\mathcal{A}$ on the other side of the S_6 symmetric active line in the opposite direction. As a result, the double loop transports all single colloids toward the S_6 symmetric line and therefore, increases the density of colloids at this line. Two further western loops $\mathcal{L}_{NW} = \sigma_\iota(\mathcal{L}_{NE})$ and $\mathcal{L}_{SW} = \sigma_\iota(\mathcal{L}_{SE})$ are mirrored at the isomorphic ι-plane (see Fig. 1). Together with the eastern loops they suppress any net motion into the isomorphic $\boldsymbol{\iota}$-direction. Similarly to the other loops in the fixed symmetry phase control spaces, we color the eastern loop with their sense of winding in the regions where they are topologically non-trivial and gray otherwise. We call the concatenation of the four loops the entry loop $\mathcal{L}_{entry} = \mathcal{L}_{NE}{}^*\mathcal{L}_{SE}{}^*\mathcal{L}_{NW}{}^*\mathcal{L}_{SW}$.

The green loop segments of the concatenated eastern loop $\mathcal{L}_{NE}{}^*\mathcal{L}_{SE}$ expand the loop with a ratchet triangle. Instead of using the original loops, we deform one of the diagonals of $\mathcal{L}_{NE}{}^*\mathcal{L}_{SE}$ to take the detour via the green segments and the other diagonal. This extended loop is topologically equivalent to the undeformed loop for symmetry phases far away from the S_6 symmetry but alters the winding numbers around the $\mathcal{B}\_$ bifurcation points for symmetry phases close to the S_6 symmetry. In the experiments we alternately deform one and the other diagonal of the loops in this way such that winding numbers around the $\mathcal{B}\_$ bifurcation points in the (cyan) active zone at the S_6 symmetry line are odd. This ensures that single particles do not come to rest in the S_6 region of the active line in action space $\mathcal{A}$ but hop back and forth in a ratchet motion. We depict this back-and-forth hopping in action space with green double-sided arrows in Fig. 4. We also show figure 4 from various perspectives in our Supplementary Video 8.

For sufficient colloidal density, the probability of dipolar interactions between the colloids polymerizing several colloids to a biped b_n consisting of n single colloids becomes significant. The S_6-symmetry line serves as a polymerization initiation site. Bipeds grow via single colloid addition polymerization but also via the addition of two bipeds. We use a central equatorial exit loop $\mathcal{L}_{exit} = \mathcal{L}_{CE}{}^*\mathcal{L}_{CW}$ consisting of two mirror symmetric loops $\mathcal{L}_{CE}$, and $\mathcal{L}_{CW} = \sigma_\iota(\mathcal{L}_{CE})$ circling around two mirror symmetric points on the equator of control space $\mathcal{C}$ commanding outgrown bipeds of the desired length to walk away from the S_6-symmetry line. The loop is chosen to be trivial for juvenile bipeds and single colloids at any location on the pattern. The walking direction for the outgrown bipeds for each of the loops $\mathcal{L}_{CE}$ and $\mathcal{L}_{CW}$ is perpendicular to the external field vector pointing to the encircled point of each of the loops and the length selection can be made via the proper placement of those points. In Fig. 4, we show the exit loop $\mathcal{L}_{exit,3}$ in control space and it can be seen that it does not wind around any of the $\mathcal{B}\_(\varphi)$-bifurcation points of single colloidal particles. The exit loop is thus trivial with respect to single colloids and does not affect the net motion of single colloidal particles. For understanding the behavior of bipeds b_n consisting of more than one colloidal particle, it is useful to introduce the polydirectional transcription space $\mathcal{T}_p$ that is the vector space of the biped end to end vectors[8].

Juvenile and outgrown bipeds response

The orientation of the (dipolar) biped is locked to that of the external field with the northern foot being a magnetic north pole and the southern foot being a south pole. Let $\mathbf{b}_n$ denote the vector from the northern foot to the southern foot of a biped of length b_n. Because of the locking of the direction of $\mathbf{b}_n$ to the external field $\mathbf{H}_{\text{ext}}$ we can, instead of depicting the fence in control space $\mathcal{C}$, print the same fence on a sphere of radius b_n. If we continuously vary the biped length, the fence lines of different length bipeds join on neighboring concentric spheres to form a fence surface $\mathcal{F}$ in $\mathcal{T}_p$.

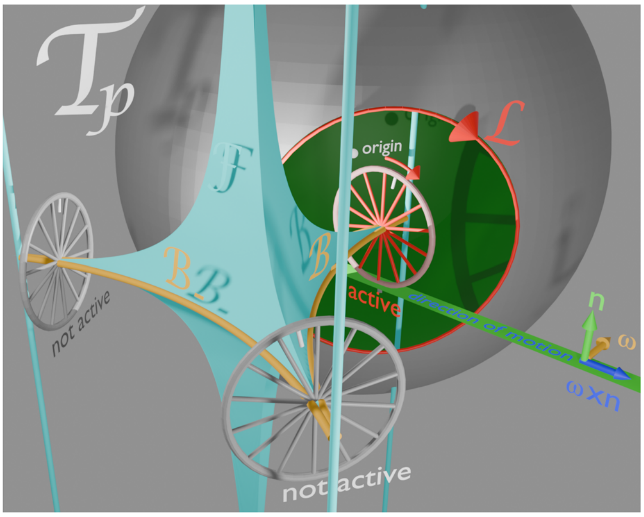

Fig. 5 | Determining the direction of motion by using the rotating wheel rule. Shown in the figure is one cyan fence pocket in transcription space separating biped vectors outside the fence supporting one minimum position of a biped per unit cell from vectors inside the fence supporting two minima. Three pairs of orange $\mathcal{B}\_$ bifurcation lines define the axes of three *virtual* wheels rolling on *virtual* support. One of the wheels, -- the red wheel -- is activated by a red loop circulating one pair of bifurcation lines in the mathematical negative sense. The biped will be transported in the same direction as the activated wheel would roll. The activated wheel shares its winding number ($w = -1$) with the activating loop $\mathcal{L}$. Any loop $\mathcal{L}$ having the same winding number will result in the same transport. The path of the loop is on a sphere of radius of the length b_n of the corresponding biped. The exact path of the loop does not matter. The loop's topological invariant, the winding number, does matter.

In Fig. 5, we outline the rotating wheel rule for bipeds that when applied to the other figures of this section, will tell us the direction of motion of the bipeds of different lengths in one particular region of action space $\mathcal{A}$. The figure shows the transcription space of possible end to end vectors $\boldsymbol{b}$, in which we compute the cyan locations of marginable stable end to end vectors, called the fence $\mathcal{F}$, that consists of concave areas separated by orange bifurcation lines $\mathcal{B}\_$. Two bifurcation lines $\mathcal{B}\_$ define an axis $\boldsymbol{\omega}$ on which we can imagine a virtual wheel. In Fig. 5 three virtual wheels sit on three pairs of $\mathcal{B}\_$ bifurcation lines. A loop circulating around one of the three axes will activate the wheel sharing the same winding number with the activating loop. The direction the wheel would roll on a virtual support below the wheel gives us the direction $\boldsymbol{\omega} \times \boldsymbol{n}$ of motion of the biped. Note that if the biped is not a single colloidal particle, the loop must not wind around the fence in a symmetric way. Sharing the winding number, – a topological invariant – with the wheel is sufficient to drive the virtual wheel forward. The rotating wheel rule is sufficient to allow the reader to predict the direction of motion. The location of the fences and bifurcation lines are computed numerically.

In previous work[8] we have shown that for fixed symmetry phase φ this fence surface is periodic and repeats in transcription space $\mathcal{T}_p$ with the primitive unit vectors of the magnetization pattern in action space $\mathcal{A}$. In Fig. 6 we plot the fence surface inside the Wigner Seitz cell with the origin $\mathbf{b}_n = \mathbf{0}$ in the center. The fence consists of surface

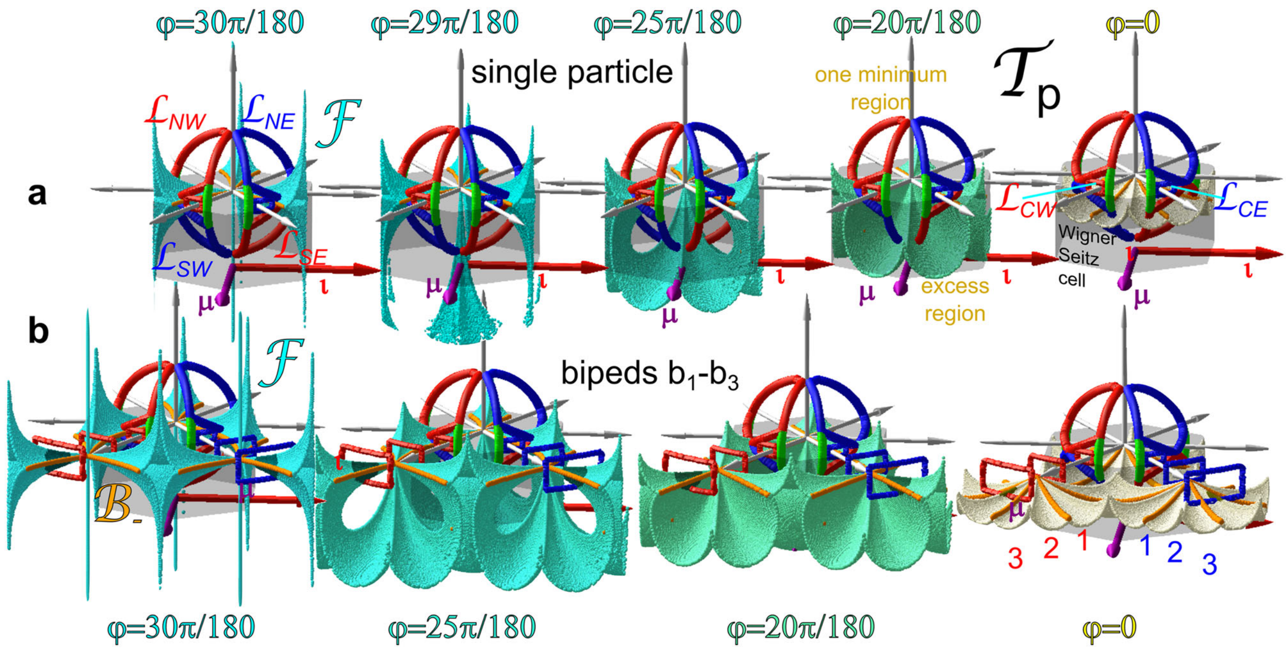

Fig. 6 | Topological character of the loops in transcription space. a Effect of the entry and exit loops $\mathcal{L}_{\text{exit},3}$ for small bipeds including single colloidal particles in the central Wigner Seitz cell of transcription space for different symmetry phases. The southern sub-loops $\mathcal{L}_{SW}$ and $\mathcal{L}_{SE}$ are topologically non-trivial for small symmetry phases and wind around two of $\mathcal{B}_-$ bifurcation lines (orange) of the fences. For larger symmetry phase the loops poke through the fence lobes of trigonal bipyramid fences and wind around none of $\mathcal{B}_-$ bifurcation lines. If one extends the southeastern loop with one ratchet triangle, the extended loop winds around one $\mathcal{B}_-$ bifurcation line and causes non-trivial ratchet jumps of the single colloids in the active zone back and forth into the metamorphic ± $\boldsymbol{\mu}$-direction. The fences for $\varphi > 30\pi/180$ (not shown) are mirror reflections at the $b_z = 0$-plane and cause the northern sub entry loops having opposite sense of revolution to transport single colloids into the opposite direction as the fences for $\varphi < 30\pi/180$. Both exit sub-loops $\mathcal{L}_{CE}$ and $\mathcal{L}_{CW}$ are topologically trivial for the single colloids and do not wind around any of the fences. **b** Periodic continuation of the fences in an extended zone scheme together with exit loops for bipeds of length b_1, b_2, and b_3. Exit loops for $n < 3$ are trivial, while the exit loops for b_3 are topologically non-trivial and wind around (shaded) lobes of the fences for large symmetry phases. For smaller symmetry phases, the exit loops still wind around the same $\mathcal{B}_-$ bifurcation lines (orange), and the loop pokes through equivalent fence facets with the minimum upon entry of the excess volume remaining stable when the loop re-exits into the one minimum volume. The non-trivial exit loop for b_3 causes the b_3-bipeds to walk into the metamorphic direction irrespective of their position on the metamorphic pattern in action space $\mathcal{A}$.

segments of positive Gaussian curvature that join at bifurcation lines of infinite negative Gaussian curvature. We show the fences for the symmetry phase $\varphi = 30\pi/180, 29\pi/180, 25\pi/180, 20\pi/180$, and $0\pi/180$. The fences for $\sigma_n(\varphi) = 60\pi/180 - \varphi$ (not shown) are obtained by taking the mirror image $\mathcal{F}_{60\pi/180-\varphi} = \sigma_n(\mathcal{F}_\varphi)$ of the fence $\mathcal{F}_\varphi$ at the $b_z = 0$ plane. The fence in transcription space $\mathcal{T}_p$ separates regions with one minimum per unit cell in $\mathcal{A}$ of the biped colloidal particle potential on the concave side of the fence in $\mathcal{T}_p$ from excess regions with two minima per unit cell in $\mathcal{A}$ of the pattern on the convex side of the fence in $\mathcal{T}_p$. The fence in $\mathcal{T}_p$ for the S_6 symmetric situation ($\varphi = 30\pi/180$) consists of a trigonal bipyramid pocket located at one of the edges of the Wigner Seitz cell harboring two minima of the potential and a line through the origin in b_z-direction having zero volume just failing to contain two minima (or maxima) since its volume is zero. Three faces of the bipyramid join at the apex located at $b_z \to \infty$ and three faces join at the antapex located at $b_z \to -\infty$ of the bipyramid. When we slightly reduce the symmetry phase to e.g., $\varphi = 29\pi/180$ the apex of the bipyramid retreats to a finite value of b_z. Both the zero volume line and the trigonal bipyramid open at their antapexes and connect to form a surface separating a region below with two minima from the region above with one minimum. The region of one minimum for $30\pi/180 > \varphi > 20\pi/180$, therefore, is not simply connected but there are connections through the holes between the base of the trigonal bipyramid and the lower part of the surfaces. A second topological transition at $\varphi = 20\pi/180$ closes these holes to separate the now simply connected region of one minimum from a simply connected region with two minima. For $\varphi = 0$, the three-fold symmetry of the fence around the origin augments to a six-fold symmetry.

A biped control loop $\mathcal{L}_n = \frac{b_n}{H_{\text{ext}}}\mathcal{L} \subset \mathcal{T}_{\text{p}}$ is the transcription of the loop $\mathcal{L} \subset \mathcal{C}$ from control space $\mathcal{C}$ to a spherical surface in transcription space of radius $b_n = nd$. In the upper part of Fig. 6, we show the transcripted entry and exit loop $\mathcal{L}_{entry}$ and $\mathcal{L}_{exit,3}$ for a single colloid $n = 1$ together with the fence surface. The cut of the sphere of radius b_1 with the fences repeats what has been shown in Fig. 4. The entry loop circulates the fences for the low symmetry phase but pokes through the fences when the symmetry phase comes close to $\varphi = 30\pi/180$. The exit loop does not wind around any fence surface and is topologically trivial for $n = 1$. When we periodically continue the fences into neighboring Wigner Seitz cells, we can infer the effect of the exit loops of bipeds $b_n = nd$ with $n = 1, 2$, and $n = 3$.

The transcriptions of the exit loop $\mathcal{L}_{exit,3}$ for $n = 1$ and $n = 2$ do not wind around any fence surfaces, while for $n = 3$ it winds around two of the (shaded) base handles of the trigonal bipyramids located in unit cells away from the origin and therefore non-trivially transports b_3-bipeds perpendicular to the two fence handles or the surfaces developing from the handle for symmetry phases $\varphi < 30\pi/180$. The symmetry of the two sub-loops of the exit loop is such as to cancel the transport into the isomorphic $\boldsymbol{\iota}$-direction, and only the transport along the metamorphic $\boldsymbol{\mu}$-direction remains. The exit loop remains invariant under reflection at the $b_z = 0$-plane followed by a time reversal operation and therefore, has the same effect in regions of action space $\mathcal{A}$ where $60\pi/180 > \varphi > 30\pi/180$. Bipeds of length b_3 are therefore, globally transported the same way on the entire metamorphic pattern.

Changing the outgrown length

In Fig. 7 we show how repositioning the exit loop $\mathcal{L}_{exit,3} \to \mathcal{L}_{exit,7}$ changes the length of the outgrown biped from b_3 to b_7. The

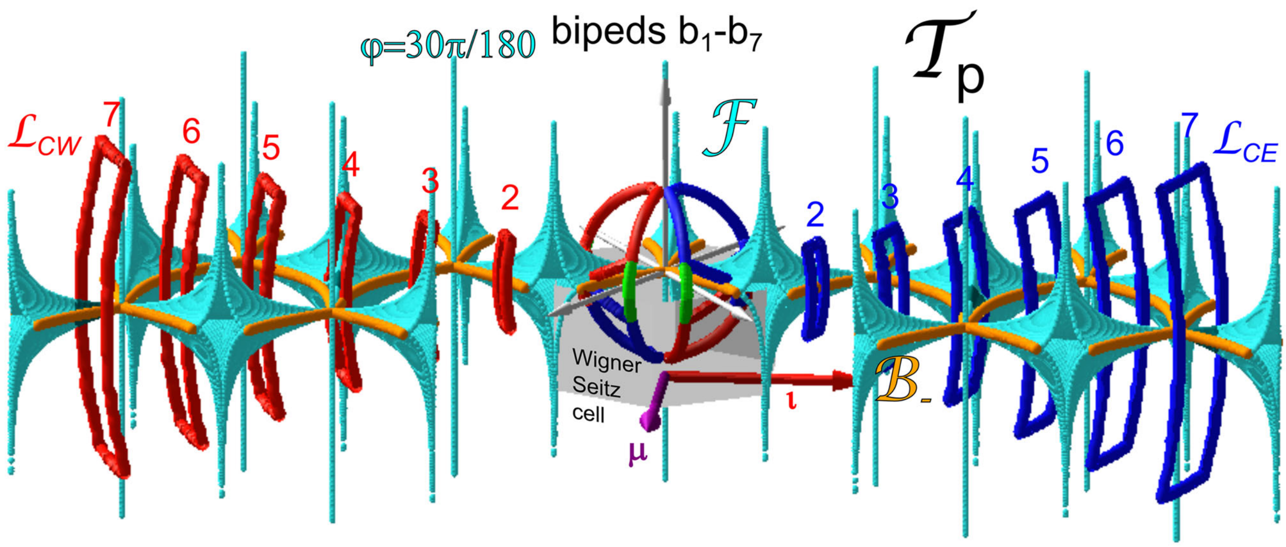

Fig. 7 | Effect of repositioning the exit loop. For an exit loop $\mathcal{L}_{exit,7}$ repositioned with respect to the exit loop $\mathcal{L}_{exit,3}$ of Fig. 6 and a symmetry phase of $\varphi = 30\pi/180$, the loop is trivial for b_1, b_2, b_3, b_5, and b_6. The motion of both sub-loops is non-trivial for b_4, but the motion is canceled by the σ_ι-symmetry of both sub-loops. The first length to be transported into the metamorphic $\boldsymbol{\mu}$-direction is a biped b_7 with the exit loop winding around the shaded lobes of the outermost handles of the periodically extended fence trigonal bipyramids. The effect is topologically robust when the b_7-biped walks into regions of lower symmetry phase φ.

transcribed exit loops $\frac{b_n}{H_{ext}}\mathcal{L}_{exit,7}$ in transcription space $\mathcal{T}_p$ for synthesizing a b_7 biped in Fig. 7 do not wind around any fences for $n = 1, 2, 3, 5$, and 6. For $\varphi = 30\pi/180$ the b_4 transcribed exit loop winds around two handles of two different trigonal bipyramids, both oriented perpendicular to the isomorphic $\boldsymbol{\iota}$-direction. Each winding of the two sub-loops individually transports b_4-bipeds into the isomorphic $\boldsymbol{\iota}$-direction but the two sub-loops cancel out any motion with the winding around the second handle undoing the motion caused by the winding around the first (see also the green experimental b_4-trajectories in Fig. 3d). The first bipeds to experience a non-trivial topological transport are b_7-bipeds. The transcribed exit loop for b_7 winds around the two outermost handles of two different trigonal bipyramids, depicted and shaded in Fig. 7. The orientations of both handles are such that the normal in-plane vectors to both handles have a metamorphic component. The two sub-loops – like for the b_4-case – cancel any motion into the isomorphic $\boldsymbol{\iota}$-direction but they add up to cause motion into the metamorphic $\boldsymbol{\mu}$-direction. The topology of the winding remains robust as the symmetry phase φ changes to lower values as the b_7-biped walks away from the active line.

Discussion

The synthesis or assembly of a product can occur via thermodynamic driving forces, in which case we talk about self assembly[16–18]. The directed assembly[19–21] via an externally controlled addition of components via joining micro fluidic channels on a lab on a chip is an externally enforced alternative to the creation of products that are not necessarily in thermodynamic equilibrium. Our topological synthesis is an example of the latter strategy but using motion[22–24] of the educts that actively self assemble to the final product. In contrast to conventional lab on the chip devices[25], our approach offers the flexibility of using the same pattern imprinted on the device for the production of alternative products. The flexibility arises via the ability to determine the outgrown product length via a smart choice of the applied external modulation. The choice to be an outgrown product, however, is an active and robust choice of the colloidal biped itself allowing the synthesis to be made without external control of its success. The topological nature of the internal decision made by the products of our device is an ingredient shared with many bio-synthetic processes in vivo.

In fact, our device functions like an enzyme in biology. Due to the low concentration of colloids, no polymer addition reactions are supposed to occur outside the active zone. Polymer addition reactions are wanted at the active line, not elsewhere. By topologically transporting single colloids into the active zone, the colloidal concentration is increased there as to increase the reaction rate. The choice of concentration, therefore, is critical for the proper functioning of the device. Since single colloids are kept at the same distance of at least one unit cell, while transporting them to the active zone, polymer addition reactions of single colloids never happened outside the active zone in our experiments. However, once an outgrown biped leaves the active zone, it counter propagates to the single colloids, and unwanted addition reactions can elongate the length of bipeds beyond the outgrown length. It is possible to design more complex metamorphic patterns where outgrown bipeds may avoid further collisions upon exit and use more sophisticated driving loops. The current work just shows the potential of the method. It produces outgrown bipeds without polydispersivity. The kinetics is of a Michaelis-Menten type saturating at a concentration when all active zones are busy. This is the case once one section of the length b_{n^*} of the active line yields roughly one outgrown biped per n^* periods of the loop. Due to the requirement of adiabatic transport, our yield is low, however, our precision is high.

Theoretically, there is no size limit to the production of bipeds of any length. In practice, in the experiments, there is a size limit. The robustness of the process relies on loops encircling the fences by keeping a distance to the bifurcation locations. The number of bifurcation locations in transcription space increases with the number of bipeds (all transcription loops to bipeds with $n < n^*$ have to fulfill the distance requirement, compare Fig. 6 and 7) which becomes increasingly challenging. The adiabatic period $T \propto n^{*3/2}$ becomes longer and longer, and at some point, we would need to reduce the modulus of the morphing reciprocal vectors $\boldsymbol{\mu}$ to avoid a biped having one foot in the S_6 the other in the C_6 region. Moreover, the total cross section of a biped grows proportional to its size, such the concentration of single colloids must be reduced to avoid unwanted collisions of the biped after its exit of the active zone.

Topological length control is a useful strategy for active self-assembly out of equilibrium. Adiabatic external modulation loops can be adapted in a versatile way to let colloidal particles decide their final length by themselves. Here, we have shown the internal active self-assembly of magnetic colloids to a biped for six different outgrown lengths. Of course, the externally applied control loop guides the active motion toward the desired length. Once the external loop is applied, however, no further external quality control, whether the components assemble to the desired structures, is needed.

Methods

Pattern

The pattern is a thin Co/Au layered system with perpendicular magnetic anisotropy lithographically patterned via ion bombardment[26,27]. The metamorphic pattern lattice constant is $a = 7\,\mu$m, and the modulation period is $2\pi/\mu = 280\,\mu$m, see the sketch in Fig. 1a. The magnetic pattern is spin-coated with a 1.6 µm polymer film that serves as a spacer between the magnetic film and the colloidal particles.

External field

The uniform external magnetic field has a magnitude of $H_{\text{ext}} = 4\,kA\text{m}^{-1}$ (significantly smaller than the coercive field of the magnetic pattern), and it is generated by one vertical and four horizontal computer-controlled coils arranged around the sample at ninety degrees.

Modulation loops

The loops consist of connections between points $P_{ij} = (\theta_i, \phi_j)$ given as spherical coordinates in $\mathcal{C}$, with $N = P_{1,j}$ and $S = P_{-1,j}$ the north and south pole. For the entry loop, we use the angles of Table 1, as well as the mirror tilt angles $\theta_{-i} = \sigma_n(\theta_i) = \pi - \theta_i$, mirrored at the equatorial plane, and the azimuthal angles $\phi_{-i} = \sigma_\iota(\phi_i) = -\phi_i$, mirrored at the $\boldsymbol{\iota}$-plane. The exit loop angles are tabulated in Table 2 according to the value n^* of the outgrown biped to be synthesized.

The sequence of points of the concatenations of all but the loops with $n^* = 2$ or $n^* = 4$ loops are:

$$
\begin{gathered}
P_{0,2}P_{-3,3},P_{2,3},P_{2,2},N,P^{n^*}_{4,5},P^{n^*}_{4,4},P^{n^*}_{-4,4},P^{n^*}_{-4,6},P^{n^*}_{4,6},P^{n^*}_{4,5},\\
N,P_{2,-2},P_{2,-1},P_{3,-1},P_{0,-2},P_{-3,-3},P_{-2,-3},P_{-2,-1},\\
P_{3,-1},P_{0,-2},P_{-3,-3},P_{2,-3},P_{2,-2},N,P^{n^*}_{4,-5},P^{n^*}_{4,-4},P^{n^*}_{-4,-4},\\
P^{n^*}_{-4,-6},P^{n^*}_{4,-6},P^{n^*}_{4,-5},N,P_{2,2},P_{2,1},P_{3,1},P_{0,2},P_{-3,3},P_{-2,3},\\
P_{-2,1},P_{3,1},P_{0,2}P_{3,3},P_{-2,3},P_{-2,2},S,P^{n^*}_{-4,5},P^{n^*}_{-4,4},P^{n^*}_{4,4},\\
P^{n^*}_{4,6},P^{n^*}_{-4,6},P^{n^*}_{-4,5},S,P_{-2,-2},P_{-2,-1},P_{-3,-1},P_{-0,-2},\\
P_{3,-3},P_{2,-3},P_{2,-1},P_{-3,-1},P_{0,-2},P_{3,-3},P_{-2,-3},P_{-2,-2},\\
S,P^{n^*}_{-4,-5},P^{n^*}_{-4,-4},P^{n^*}_{4,-4},P^{n^*}_{4,-6},P^{n^*}_{-4,-6},P^{n^*}_{-4,-5},S,P_{-2,2},\\
P_{-2,1},P_{-3,1},P_{0,2},P_{3,3},P_{2,3},P_{2,1},P_{-3,1},P_{0,2}
\end{gathered}
$$

Table 1 | Entry loop angles

θ_0	θ_1	θ_2	θ_3	ϕ_1	ϕ_2	ϕ_3
π/2	0	π/18	7π/18	π/9	π/3	5π/9

Table 2 | Exit loop angles

n^*	$\theta_4^{n^*}$	$\phi_4^{n^*}$	$\phi_5^{n^*}$	$\phi_6^{n^*}$
2	70π/180	140π/180	170π/180	170π/180
3	85π/180	25π/180	35π/180	45π/180
3&4	70π/180	100π/180	100π/180	140π/180
5	75π/180	5π/180	20π/180	35π/180
6	75π/180	125π/180	135π/180	135π/180
7	75π/180	65π/180	75π/180	75π/180

For $n^* = 2$ the effect of $\mathcal{L}_{entry}$ on b_2-bipeds is topologically equivalent to that on single colloidal particles. Therefore the entry loop transports b_2-bipeds toward the active zone. To overcome this transport, we duplicate the winding numbers of the exit loops according to $\mathcal{L}_{exit,2} \to \mathcal{L}^2_{exit,2}$, that makes the exit loop dominant over the entry loop for the b_2-bipeds. For the point sequence one should replace all exit segments according to the scheme $N, P^2_{4,5}, P^2_{4,4}, P^2_{-4,4}, P^2_{-4,6}, P^2_{4,6}, P^2_{4,5}, N \to N, P^2_{4,5}, P^2_{4,4}, P^2_{-4,4}, P^2_{-4,6}, P^2_{4,6}, P^2_{4,5}, P^2_{4,4}, P^2_{-4,4}, P^2_{-4,6}, P^2_{4,6}, P^2_{4,5}, N$ and so forth.

For $n^* = 4$ there are no simple robust exit loops not affecting bipeds b_n with $n < 4$. We, therefore, apply two exit loops and replace a non-robust exit loop (that exists) by a robust one according to $\mathcal{L}_{exit,4} \to \mathcal{L}_{exit,3\&4} {}^*\mathcal{L}^{-1}_{exit,3}$, where the first robust loop $\mathcal{L}_{exit,3\&4}$ transports both, b_3 and b_4, into the metamorphic direction followed by the second loop $\mathcal{L}^{-1}_{exit,3}$ transporting b_3 against the metamorphic direction. For the point sequence one should replace all exit segments according to the scheme $N, P^{n^*}_{4,5}, P^{n^*}_{4,4}, P^{n^*}_{-4,4}, P^{n^*}_{-4,6}, P^{n^*}_{4,6}, P^{n^*}_{4,5}, N \to N, P^{3\&4}_{4,5}, P^{3\&4}_{4,4}, P^{3\&4}_{-4,4}, P^{3\&4}_{-4,6}, P^{3\&4}_{4,6}, P^{3\&4}_{4,5}, N, P^3_{4,5}, P^3_{4,6}, P^3_{-4,6}, P^3_{-4,4}, P^3_{4,4}, P^3_{4,5}, N$ and so forth.

The point sequences for all outgrown bipeds include transfer segments between the eastern and western parts of the entry loop and between the exit and entry loop that we have not shown in the main part of the work. Such transfer segments are topologically trivial and irrelevant to understanding the topological invariants governing the transport. In principle the transfer between loops can be made anywhere, however, the equatorial region should not be used due to increased friction of a biped with the solid support. Our connectors between loops are all via the north $N = P_{1,j}$ or south pole $S = P_{-1,j}$.

The adiabatic nature is ensured by keeping the Mason number of all bipeds below one $\mathcal{M} \ll 1$. The Mason number of an outgrown biped is $\mathcal{M} = 2\pi\eta n^{*3/2}/\mu_0\chi_{\text{eff}}H_{\text{ext}}H_pT_F$ (with η the shear viscosity of the fluid and χ_{eff} the effective magnetic susceptibility of a colloidal particle, and T_F the period of a fundamental loop.). The effect of non-adiabatic driving has been discussed in ref. 15. In our experiments with $n^* = 7$ we used a modulation period of $T_F = 25$ s for a fundamental loop. Our modulation loop consists of twelve fundamental loops such that the largest period used was $T \approx 5$ min for our largest outgrown biped.

Visualization

The colloids and the pattern are visualized using reflection microscopy. The pattern is visible because the ion bombardment changes the reflectivity of illuminated regions as compared to that of the masked regions. A camera records video clips of the single colloidal particles and the bipeds.

Fence equations

A biped is subject to a total potential proportional to $-\int_{\text{biped}} \mathbf{d}^3\mathbf{r}\ \mathbf{H}_{\text{ext}} \cdot \mathbf{H}_{\text{p}}$, which is the integral over the biped volume of the coupling between the external $\mathbf{H}_{\text{ext}}$ and the pattern $\mathbf{H}_{\text{p}} = -\nabla\psi$ fields[11,12]. This coupling leads to an effective biped potential V proportional to the difference in magnetostatic potential at the two feet. That is,

$$V(\mathbf{r}_\mathcal{A} + z\boldsymbol{n}, \mathbf{b}, \varphi) \propto \psi(\mathbf{r}_\mathcal{A} + \mathbf{b}/2, \varphi) - \psi(\mathbf{r}_\mathcal{A} - \mathbf{b}/2, \varphi) \tag{3}$$

with the biped centered at $\mathbf{r}_\mathcal{A}$ and with $\psi(\mathbf{r},\varphi) \propto e^{-qz}\sum_{i=0}^{2}\cos(\mathbf{q_i}\cdot\mathbf{r} - \varphi)$ the magnetostatic potential. Note that V depends explicitly on $\mathbf{H}_{\text{ext}}$ via the one-to-one correspondence between $\mathbf{b}/b$ and $\mathbf{H}_{\text{ext}}/H_{\text{ext}}$. Transport of a biped b_n after completion of one modulation loop $\mathcal{L} \subset \mathcal{C}$ occurs provided that $\mathcal{L}_n = \frac{b_n}{H_{\text{ext}}}\mathcal{L} \subset \mathcal{T}_{\text{p}}$ winds around bifurcation lines, which are the cusps of the fences. The fences are those orientations $\mathbf{b} \in \mathcal{T}_{\text{p}}$ for which the potential is marginally stable[11], i.e., the set of biped orientations for which $\nabla_\mathcal{A}V = 0$ and $\det(\nabla_\mathcal{A}\nabla_\mathcal{A}V) = 0$. For the present metamorphic pattern and for a slowly varying symmetry phase $|\nabla_\mathcal{A}\varphi| \ll q$ both conditions have been numerically determined to be fulfilled along the fence surfaces in $\mathbf{b} \in \mathcal{T}_p$ depicted in Fig 6. For a constant symmetry phase the biped potential is periodic and invariant under the simultaneous transformation $\mathbf{b} \to \mathbf{b} + \mathbf{a}_i$ and $\mathbf{r}_{\mathcal{A}} \to \mathbf{r}_{\mathcal{A}} + \mathbf{a}_i/2$ with $\mathbf{a}_i$, $i = \{0, 1, 2\}$, a lattice vector, cf. Eq. (3). The same periodicity in $\mathbf{b} \in \mathcal{T}_p$ applies, therefore, to the fences.

Data availability

All the data supporting the findings are available from the corresponding author. All trajectories of particles are extracted from Supplementary Videos 2–7. We append the tracked particle files and a maple code in a supplementary dataset called figurerawdata.zip that converts this data into figures 2 and 3. Source data are provided with this paper.

References

1. Matyjaszewski, K. & Xia, J. Atom transfer radical polymerization. *Chem. Rev.* **101**, 2921 (2001).
2. Ogi, S., Sugiyasu, K., Manna, S., Samitsu, S. & Takeuchi, M. Living supramolecular polymerization realized through a biomimetic approach. *Nat. Chem.* **6**, 188 (2014).
3. Ghicov, A. & Schmuki, P. Self-ordering electrochemistry: a review on growth and functionality of TiO_2 nanotubes and other self-aligned MO_x structures. *Chem. Commun.* https://doi.org/10.1039/B822726H, 2791–2808 (2009).
4. Sun, Y., Mayers, B., Herricks, T. & Xia, Y. Polyol synthesis of uniform silver nanowires: a plausible growth mechanism and the supporting evidence. *Nano Lett.* **3**, 955 (2003).
5. Li, X., Hao, C., Tian, C., Wang, P. & Mao, C. Vernier assembly: controlling DNA polymerization via length mismatching. *Chem. Commun.* **50**, 6361 (2014).
6. Marshall, W. F., Qin, H., Rodrigo Brenni, M. & Rosenbaum, J. L. Flagellar length control system: testing a simple model based on intraflagellar transport and turnover. *Mol. Biol. Cell* **16**, 270 (2005).
7. Turck, F., Fornara, F. & Coupland, G. Regulation and identity of florigen: FLOWERING LOCUS T moves center stage. *Annu. Rev. Plant Biol.* **59**, 573 (2008).
8. Mirzaee-Kakhki, M. et al. Simultaneous polydirectional transport of colloidal bipeds. *Nat. Commun.* **11**, 4670 (2020).
9. Loehr, J. et al. Lattice symmetries and the topologically protected transport of colloidal particles. *Soft Matter* **13**, 5044 (2017).
10. Loehr, J., Loenne, M., Ernst, A., de las Heras, D. & Fischer, T. M. Topological protection of multiparticle dissipative transport. *Nat. Commun.* **7**, 11745 (2016).
11. de las Heras, D., Loehr, J., Loenne, M. & Fischer, T. M. Topologically protected colloidal transport above a square magnetic lattice. *New J. Phys.* **18**, 105009 (2016).
12. Loehr, J. et al. Colloidal topological insulators. *Comm. Phys.* **1**, 4 (2018).
13. Stuhlmüller, N. C. X. et al. Simultaneous and independent topological control of identical microparticles in non-periodic energy landscapes. *Nat. Commun.* **14**, 7517 (2023).
14. Mirzaee-Kakhki, M. et al. Gauge invariant and gauge dependent aspects of topological walking colloidal bipeds. *Soft Matter* **17**, 1663 (2021).
15. Mirzaee-Kakhki, M. et al. Colloidal trains. *Soft Matter* **16**, 1594 (2020).
16. McGorty, R., Fung, J., Kaz, D. & Manoharan, V. N. Colloidal self-assembly at an interface. *Mat. Today* **13**, 34 (2010).
17. Mallory, S. A., Valeriani, C. & Cacciuto, A. An active approach to colloidal self-assembly. *Annu. Rev. Phys. Chem.* **69**, 59 (2018).
18. Russo, J. et al. Sat-assembly: a new approach for designing self-assembling systems. *J. Phys. Cond. Mat.* **34**, 354002 (2022).
19. Grzelczak, M., Vermant, J., Furst, E. M. & Liz-Marzán, L. M. Directed self-assembly of nanoparticles. *ACS Nano* **4**, 3591 (2010).
20. Sazan, H., Piperno, S., Layani, M., Magdassi, S. & Shpaisman, H. Directed assembly of nanoparticles into continuous microstructures by standing surface acoustic waves. *J. Coll. Int. Sci.* **536**, 701 (2019).
21. Preger, C., Josefsson, M., Westerström, R. & Messing, M. E. Bottom-up field-directed self-assembly of magnetic nanoparticles into ordered nano- and macrostructures. *Nanotech.* **32**, 195603 (2021).
22. Koumakis, N., Maggi, C. & Di Leonardo, R. Directed transport of active particles over asymmetric energy barriers. *Soft Matter* **10**, 5695 (2014).
23. Schakenraad, K. et al. Topotaxis of active Brownian particles. *Phys. Rev. E* **101**, 032602 (2020).
24. Martinez, R., Alarcon, F., Aragones, J. L. & Valeriani, C. Trapping flocking particles with asymmetric obstacles. *Soft Matter* **16**, 4739 (2020).
25. deMello, A. J. Control and detection of chemical reactions in microfluidic systems. *Nature* **442**, 394 (2006).
26. Chappert, C. et al. Planar patterned magnetic media obtained by ion irradiation. *Science* **280**, 1919 (1998).
27. Kuświk, P. et al. Colloidal domain lithography for regularly arranged artificial magnetic out-of-plane monodomains in Au/Co/Au layers. *Nanotechnology* **22**, 095302 (2011).

Acknowledgements

T.M.F. and D.d.l.H. acknowledge funding by the Deutsche Forschungsgemeinschaft (DFG, German Research Foundation) under project number 531559581 and by the Open Access Publishing Fund of the University of Bayreuth. P.K., M.U., and F.S. acknowledge financial support from the National Science Centre Poland through the OPUS funding (Grant No. 2019/33/B/ST5/02013).

Author contributions

J.E., F.F., D.d.l.H., and T.M.F. designed and performed the experiment, computed the fences and bifurcation points and lines, and wrote the manuscript with input from all the other authors. J.E. and F.F. contributed equally to this work. P.K., M.U., and F.S. produced the magnetic film. S.A., & A.r.E. performed the fabrication of the micromagnetic metamorphic patterns within the magnetic thin film.

Funding

Open Access funding enabled and organized by Projekt DEAL.

Competing interests

The authors declare no competing financial or non-financial interests.

Additional information

Supplementary information The online version contains supplementary material available at https://doi.org/10.1038/s41467-024-50023-7.

Correspondence and requests for materials should be addressed to Thomas M. Fischer.

Peer review information *Nature Communications* thanks Fernando Martínez-Pedrero, Ning Wu, and the other, anonymous, reviewer for their contribution to the peer review of this work. A peer review file is available.

https://doi.org/10.1038/s41467-024-50023-7

Publication 2

Supporting Information

Supplementary Material for Topologically controlled synthesis of active colloidal bipeds

Jonas Elschner,[1] Farzaneh Farrokhzad,[1] Piotr Kuświk,[2] Maciej Urbaniak,[2] Feliks Stobiecki,[2] Sapida Akhundzada,[3] Arno Ehresmann,[3] Daniel de las Heras,[4] and Thomas M. Fischer[1, *]

[1] *Experimentalphysik X, Physikalisches Institut, Universität Bayreuth, D-95440 Bayreuth, Germany*
[2] *Institute of Molecular Physics, Polish Academy of Sciences, 60-179 Poznań, Poland.*
[3] *Institute of Physics and Center for Interdisciplinary Nanostructure Science and Technology (CINSaT), Universität Kassel, D-34132 Kassel, Germany*
[4] *Theoretische Physik II, Physikalisches Institut, Universität Bayreuth, D-95440 Bayreuth, Germany*

(Dated: June 24, 2024)

This PDF file includes:
Description of Movies S1 to S8
Other Supplementary Materials for this manuscript include the following:
Movies S1 to S8

MOVIE FILES

Supplementary Video 1 Videoclip showing a flyby along action space and control space allowing to see all subloops in control space, including $\mathcal{L}_{\mathrm{CW}}$ which is not visible in figure 1.

Supplementary Video 2 Videoclip showing the response of colloidal particles to the application of the loop $\mathcal{L}_{entry} * \mathcal{L}^2_{\mathrm{e}xit,2}$. The clip shows one biped and four single colloids in the active zone right from the start, the transport of two single colloidal particles toward the active zone (colored in cyan), the growth of one further biped to the outgrown b_2 length and the transport of both outgrown bipeds out of the active zone.

Supplementary Video 3 Videoclip showing the response of colloidal particles to the application of the loop $\mathcal{L}_{entry} * \mathcal{L}_{\mathrm{e}xit,3}$. The clip shows the transport of six single colloidal particles toward the active zone (colored in cyan), the growth of two bipeds to the outgrown b_3 length and the transport of outgrown bipeds out of the active zone.

Supplementary Video 4 Videoclip showing the response of colloidal particles to the application of the loop $\mathcal{L}_{entry} * \mathcal{L}_{\mathrm{e}xit,3\&4} * \mathcal{L}^{-1}_{\mathrm{e}xit,3}$. The clip shows the transport of ten single colloidal particles toward the active zone (colored in cyan), the growth of two bipeds to the outgrown b_4 length, the transport of outgrown bipeds out of the active zone and two single colloids remaining in the active zone.

Supplementary Video 5 Videoclip showing the response of colloidal particles to the application of the loop $\mathcal{L}_{entry} * \mathcal{L}_{\mathrm{e}xit,5}$. The clip shows the transport of eighteen single colloidal particles toward the active zone (colored in cyan), the growth of three bipeds to the outgrown b_5 length, the growth of one biped to a juvenile b_3-biped, and the transport of the three outgrown bipeds out of the active zone.

Supplementary Video 6 Videoclip showing the response of colloidal particles to the application of the loop $\mathcal{L}_{entry} * \mathcal{L}_{\mathrm{e}xit,6}$. The clip shows the transport of several single colloidal particles toward the active zone (colored in cyan), the growth of one biped to the outgrown b_6 length, the transport of the outgrown biped out of the active zone, and the remaining of three single colloids in the active zone.

Supplementary Video 7 Videoclip showing the response of colloidal particles to the application of the loop $\mathcal{L}_{entry} * \mathcal{L}_{\mathrm{e}xit,7}$. The clip shows the transport of twenty single colloidal particles toward the active zone (colored in cyan), the growth of two bipeds to the outgrown b_7 length, the growth of one biped to a juvenile b_6-biped, and the transport of the two outgrown bipeds out of the active zone.

Supplementary Video 8 Videoclip showing a flyby along the action space and control space of figure 4, allowing to see all subloops and all northern excess regions in control space.

Publication 3

Magnetic colloidal single particles and dumbbells on a tilted washboard moiré pattern in a precessing external field

Soft Matter, 20, 9312 - 9318 (2024)

Farzaneh Farrokhzad[a1], Nico C. X. Stuhlmüller[a2], Piotr Kuświk[b], Maciej Urbaniak[b], Feliks Stobiecki[b], Sapida Akhundzada[c], Arno Ehresmann[c], Daniel de las Heras[a2], and Thomas M. Fischer[a1]

[a1] Experimental Physics X and [a2] Theoretical Physics II, Department of Physics, University of Bayreuth, 95447 Bayreuth, Germany.
[b] Institute of Molecular Physics, Polish Academy of Sciences, 60-179 Poznań, Poland.
[c] Institure of Physics and Center for Interdisciplinary Nanostructure Science and Technology (CINSaT), University of Kassel, Germany.

This paper shows the different transport modes of single colloidal particles and dumbbells occuring in a twisted pattern inside and nearby the flat channels, when the pattern is inclined with respect to gravity and when the particles are subject to a precessing external magnetic field.

My Contribution

I designed and performed the experiments. I wrote the manuscript together with Daniel de las Heras and Thomas Fischer with input from all the other authors. Nico C. X. Stuhlmüller computed the dithered patterns. Piotr Kuświk, Maciej Urbaniak, and Feliks Stobiecki produced the magnetic film. Sapida Akhundzada, and Arno Ehresmann performed the fabrication of the micromagnetic metamorphic patterns within the magnetic thin film.

Soft Matter

PAPER

Check for updates

Cite this: *Soft Matter*, 2024, **20**, 9312

Magnetic colloidal single particles and dumbbells on a tilted washboard moiré pattern in a precessing external field†

Farzaneh Farrokhzad,[a] Nico C. X. Stuhlmüller,[d] Piotr Kuświk,[b] Maciej Urbaniak,[b] Feliks Stobiecki,[b] Sapida Akhundzada,[c] Arno Ehresmann,[c] Daniel de las Heras[d] and Thomas M. Fischer *[a]

Received 8th October 2024, Accepted 10th October 2024

DOI: 10.1039/d4sm01183j

rsc.li/soft-matter-journal

We measure the dynamical behavior of colloidal singlets and dumbbells on an inclined magnetic moiré pattern, subject to a precessing external homogeneous magnetic field. At low external field strength single colloidal particles and dumbbells move everywhere on the pattern: at stronger external field strengths colloidal singlets and dumbbells are localized in generic locations. There are however nongeneric locations of flat channels that cross the moiré Wigner Seitz cell. In the flat channels we find gravitational driven translational and non-translational dynamic phase behavior of the colloidal singlets and dumbbells depending on the external field strength and the precession angle of the external homogeneous magnetic field.

1. Introduction

Current research focuses on the electric conductivity and transport behavior in twisted hexagonal structures such as twisted bilayer graphene,[1–7] and twisted bilayers of the transition metal dichalcogenide family[8] because of their non-conventional superconductive[9–15] and ferromagnetic[16,17] phase behavior. Information on the physics of these systems can be gained by investigating other twisted systems: The transport of waves in twisted photonic[18–22] or acoustic[23–27] crystals as well as in vortex lattices[28] is based on similar topological transport behaviour.

We have focussed on the transport properties of classical macroscopic magnetic particle systems[29,30] as well as on transport properties of soft matter magnetic colloidal particle systems[31–40] and specifically subject to twisted magnetic patterns.[41–43] The magnetic potential of twisted patterns subject to an external drift force is a special form of a tilted washboard potential.[44–49] Tilted washboard potentials show interesting transitions[50] in their transport properties as a function of their tilt.

Here, we study the motion of single colloidal particles and of colloidal dumbbells above inclined flat channels[41] created by a magnetic moiré pattern being an overlay of two magically twisted hexagonal (or square) generator patterns of alternating magnetization (see Fig. 1). The resulting magnetic moiré pattern creates a magnetic field $\boldsymbol{H}_{\mathrm{p}}$ that is periodic with a hexagonal (square) shaped moiré Wigner Seitz cell. Superposition of an external magnetic field that is much stronger than the pattern field leads to a colloidal potential that consists of mostly localized potential minima and maxima. There are however extended regions of negative interference within the superposition where the potential is almost flat, called the flat channel. A flat colloidal potential channel follows a zig-zag path through the moiré Wigner Seitz cell. The corrugation of the potential above the flat channel is significantly weaker than the modulation of the potential between the localized maxima and minima. We immerse paramagnetic colloidal particles in water above the pattern and let them sediment to an equilibrium position a few nanometers above the pattern. There, they either rest on the pattern as single colloidal particles or self assemble to colloidal dumbbells of two particles held together *via* dipolar interactions.[36–38] When the external magnetic field is not normal to the pattern the flat channel direction and the external magnetic field compete to orient the colloidal dumbbells.

We apply a time dependent homogeneous external magnetic field precessing around the pattern normal at a fixed precession angle. When we sufficiently incline the moiré pattern gravity can drive the colloidal particles and colloidal dumbbells through the flat channels, while colloids in the localized minima always remain immobile. Due to the competition of anisotropic interactions, we distinguish two forms of motion along the flat channels. We find dumbbells slithering along the

[a] *Experimentalphysik X, Physikalisches Institut, Universität Bayreuth, D-95440 Bayreuth, Germany. E-mail: thomas.fischer@uni-bayreuth.de*
[b] *Institute of Molecular Physics, Polish Academy of Sciences, 60-179 Poznań, Poland*
[c] *Institute of Physics and Center for Interdisciplinary Nanostructure Science and Technology (CINSaT), Universität Kassel, D-34132 Kassel, Germany*
[d] *Theoretische Physik II, Physikalisches Institut, Universität Bayreuth, D-95440 Bayreuth, Germany*

† Electronic supplementary information (ESI) available. See DOI: **https://doi.org/10.1039/d4sm01183j**

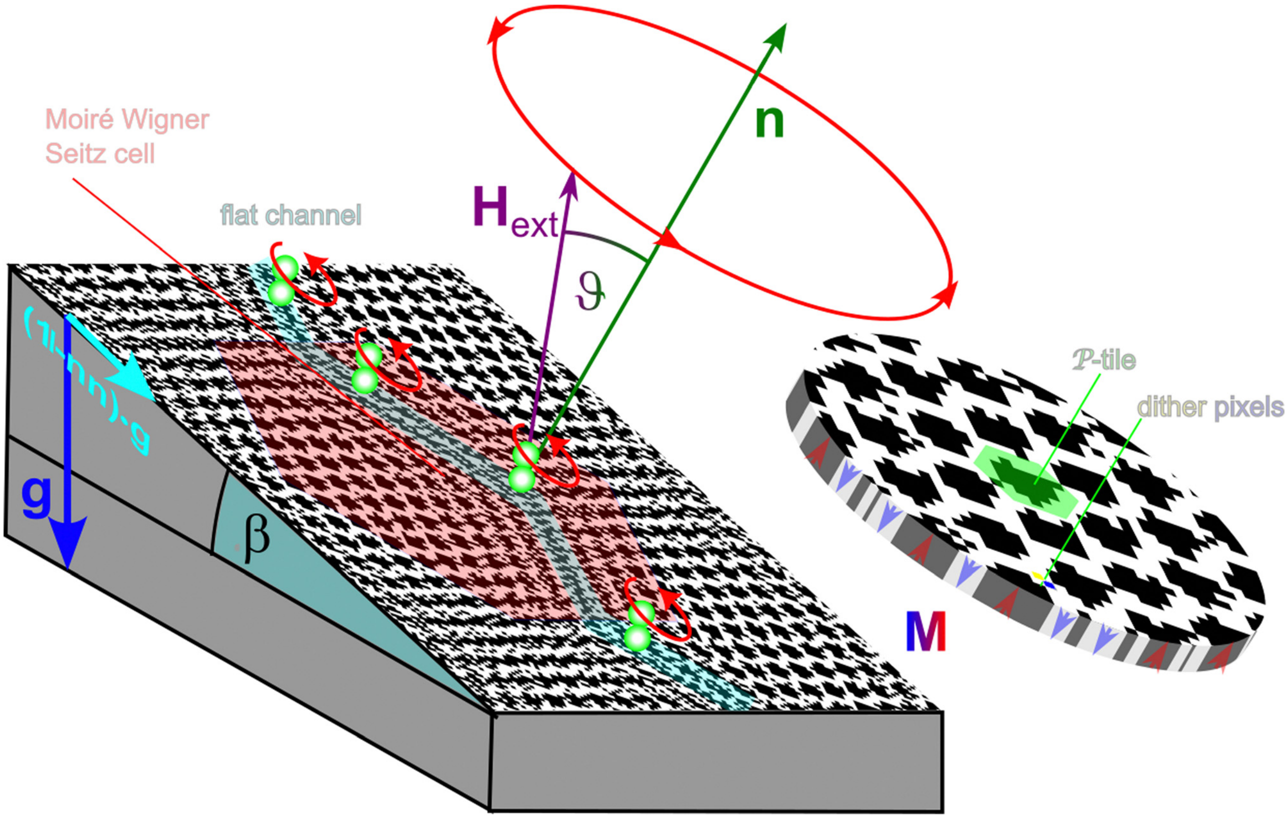

Fig. 1 Scheme of the setup: a magnetic moiré pattern with (black) up and (white) down magnetized dithered domains mathematically computed from two superposed magically twisted periodic magnetic generator patterns and then imprinted. The moiré pattern is a pattern of three different length scales. The moiré pattern is periodic with a hexagonal moiré Wigner Seitz cell. We can dissect the moiré Wigner Seitz cell into smaller hexagonal $\mathcal{P}$-tiles (see the green $\mathcal{P}$-tile in the magnified disk-shaped subregion; the unit vectors of the $\mathcal{P}$-tile are orthogonal to the unit vectors of the moiré Wigner Seitz cell). The generic $\mathcal{P}$-tile contains a localized minimum and maximum of the colloidal potential. The smallest length scale of the pattern is introduced by the dithering procedure (In the diskshaped subregion one white and one black dither pixel are recolored in yellow and blue). There are non generic $\mathcal{P}$-tiles that connect to form a flat channel (cyan) following a zig-zag path through the moiré Wigner Seitz cell. Due to the dithering, the particle-surface potential above the flat channel is corrugated and rough on the scale of the dithers. The moiré pattern is inclined with respect to the direction of gravity $\hat{\boldsymbol{g}}\cdot\boldsymbol{n} = -\cos\beta$ and subject to a precessing homogeneous (angular frequency ω) external field with precession angle $\boldsymbol{H}_{\text{ext}}\cdot\boldsymbol{n} = \cos\vartheta$. Paramagnetic colloidal particles sediment onto the pattern and form colloidal dumbbells *via* dipolar interaction. While colloidal dumbbells in generic $\mathcal{P}$-tiles cannot move, colloidal assemblies (some singlets, mainly dumbbells) that reside within the non-generic flat channels may or may not slide down along them exhibiting different forms of orientational dynamics.

flat channel with the head of the colloidal dumbbell always pointing in direction of the channel and we find precessing colloidal dumbbells sliding along the flat channel and at the same time precessing with the external field. We present a dynamic phase diagram of the various transport modes in both hexagonal twisted and square twisted patterns.

2. Results

We use a magnetic Co/Au multilayer, which has been patterned by keV He^{+}-ion bombardment through a lithographical mask[51,52] in a home-built bombardment stage.[53] Instead of creating a magnetic moiré pattern by twisting two thin film patterns, we lithographically produce the moiré pattern by calculating the magnetization due to superposition of the two generator patterns and imprinting the corresponding magnetization directly into one magnetic thin film. The quasi two dimensional magnetization of our moiré pattern in this single film of thickness t = 5 nm reads[41]

$$M = M_{\text{s}}\mathcal{D}\left(\sum_{p=\pm}\sum_{i=1}^{2n}\left[\cos(\boldsymbol{k}^{i}\cdot\boldsymbol{s}_{\text{p}}(\boldsymbol{r})) + t_{n}\right]\right) \tag{1}$$

with $M_{\text{s}} \approx 1420$ kA m^{-1} the saturation magnetization of Co. The normal component of the pattern magnetic field satisfies the thin film boundary condition $H_z^{\text{p}} = ktM$ right at the film surface. $\mathcal{D}$ denotes a dithering procedure that converts a continuous gray scale image into a dithered image having only the digitized values ± 1 and with pixel size of 1 μm for the square (n = 2) and 2 μm for the hexagonal (n = 3) pattern. The first sum runs over p = + and p = −. Each term creates one of two generator patterns with a generator Wigner Seitz cell of hexagonal (n = 3) or square (n = 2) symmetry and generator lattice constant a = 14 μm. The $\boldsymbol{k}^{i} = \boldsymbol{R}_{\pi/n}^{i-1}\cdot\boldsymbol{k}^{1}$ in the first term of eqn (1) are the $2n$ (i = 1,...,$2n$) primitive reciprocal unit vectors of magnitude $k = 2\pi/a\sin(\pi/n)$ of the non rotated hexagonal (n = 3) or square (n = 2) generator patterns. The matrices $\boldsymbol{R}_{\pi/n}$ are rotation matrices by the angles π/n generating a pattern of the appropriate rotation symmetry. The shift vectors $\boldsymbol{s}_{\pm}(\boldsymbol{r}) = \boldsymbol{R}_{\pm\alpha/2}^{-1}\cdot(\boldsymbol{r}-\boldsymbol{r}_{\text{center},\pm}) \overset{\text{mod}\,\boldsymbol{a}_1,\boldsymbol{a}_2}{=} \boldsymbol{s}_{\pm}(\boldsymbol{0}) + \boldsymbol{R}_{\pm\alpha/2}^{-1}\cdot\boldsymbol{r}$ of both patterns are the vectors from the nearest generator Wigner Seitz cell centers in each of the rotated generator patterns toward the lateral 2D-position of interest $\boldsymbol{r}$, but rotated back into the unrotated generator pattern orientation. Non generic transport behavior is predicted for magic twist angles in smooth twisted colloidal systems.[41] This non generic behavior disappears in magically twisted system including disorder.[43] The $\boldsymbol{R}_{\pm\alpha/2}$ are rotation matrices by $\pm\alpha/2$ which is half of a magic twist angle $\alpha_k^n = 2\arctan[\sin(\pi/n)/(nk+1+\cos(\pi/n))]$. We use $\alpha_7^3 = 4.40846^\circ$ for the hexagonal and $\alpha_{13}^2 = 4.24219^\circ$ for the square pattern. The choice of magic twist angle ensures a minimal size of the final moiré Wigner Seitz cell (with magically twisted moiré unit vectors $\boldsymbol{a}_i^{\mathcal{TW}} = [\sin(\pi/n)/n\sin(\alpha/2)]\{\boldsymbol{a}_i + \boldsymbol{a}_{i+1}\}$). We use shift vectors $\boldsymbol{s}_+(0) = \boldsymbol{0}$ and $\boldsymbol{s}_-(0) = \boldsymbol{a}_1/2$ that centers the resulting flat channel of the colloidal potential to the origin of the moiré Wigner Seitz cell. The abbreviation (mod $\boldsymbol{a}_1$,$\boldsymbol{a}_2$) above the equal sign indicates that the left and right side of the equation are equal up to differences of integer multiples of the primitive generator lattice vectors of one of the unrotated generator patterns. The parameter t_n in (1) is chosen such that the average magnetization of the moiré pattern vanishes. An example of the dithered twisted hexagonal moiré pattern is shown in Fig. 1 with black up- and white down- magnetized domains. We can dissect the moiré Wigner Seitz cell into $\mathcal{P}$-tiles (with primitive tile vectors $\boldsymbol{a}_i^{\mathcal{P}}$)[43] that are a little bit larger ($\boldsymbol{a}_i^{\mathcal{P}} = \boldsymbol{a}_i/2\cos(\alpha/2)$) than one quarter of the generator unit cells (with primitive generator unit vectors $\boldsymbol{a}_i$). The generic hexagonal $\mathcal{P}$-tile harbors one minimum (one black domain) and two maxima (two white extended domain vertices) of the colloidal potential. The generic square $\mathcal{P}$-tile harbors one minimum (one black domain) and one maximum (one white domain) of the colloidal potential. In both hexagonal and square twisted patterns, non-generic $\mathcal{P}$-tiles connect to form a flat channel the corrugation of which is much smaller than the modulation within a generic $\mathcal{P}$-tile. Like other zig-zag paths in colloidal science[54] or in dissipative physics[55] our connected flat channel is chiral. Corners along the zig zag path are generically different from each other for non magic angles, but become equivalent for magic angles.[41] This is the reason why in smooth twisted potentials the transport behavior is very different at magic angles as compared to the generic non-magic twist angles.[43]

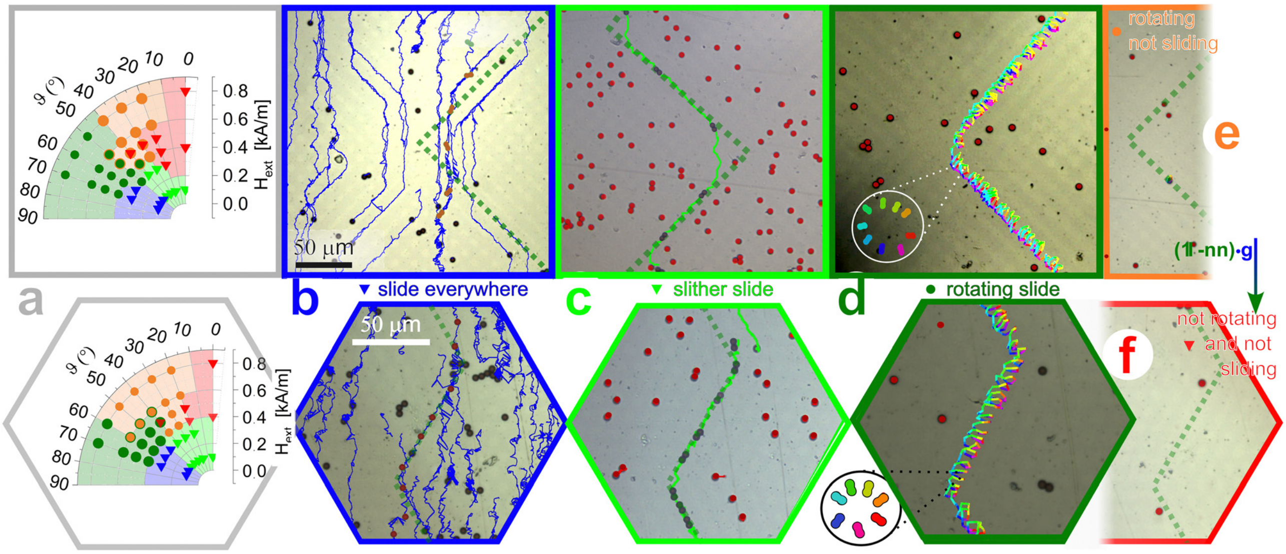

Fig. 2 Transport modes (a) dynamical phase diagrams (polar plot) of the inclined dithered twisted square (top) and hexagonal (bottom) pattern as a function of the precession angle ϑ and the strength of the external magnetic field H_{ext}. Symbols are experimentally measured data points. The color indicates the observed transport mode of the colloidal singlets and dumbbells. The color coded areas in the diagram are a guide to the eye. (b) Overlay of microscope images of the sliding motion in generic and non generic $\mathcal{P}$-tiles of the inclined dithered twisted square (top) and hexagonal (bottom) pattern. The in-plane direction of gravity $(1-\boldsymbol{nn})\cdot\boldsymbol{g}$ in all panels (a)–(f) is from the top to the bottom of the moiré Wigner Seitz cell. The colloidal particles and dumbbells move everywhere. The directions of motion is at an angle $\pm\pi/2n$ with respect to the inclination $(1-\boldsymbol{nn})\cdot\boldsymbol{g}$ direction or along the inclination direction. The flat channel is marked as dark green dotted lines. (c) Overlay of microscope images of the non-moving single colloidal particles inside generic $\mathcal{P}$-tiles and of moving colloidal dumbbells inside the flat channel within one twisted square (top) and hexagonal (bottom) moiré Wigner Seitz cell. The colloidal dumbbells move through the flat channel (trajectory bright green line, flat channel dashed dark green line) with their long axes locked to the flat channel direction. (d) Microscope image of single colloidal particles inside generic $\mathcal{P}$-tiles and of colloidal dumbbells inside the flat channel. The dumbbells move through the flat channel of the square (top) and hexagonal (bottom) moiré Wigner Seitz cell while precessing with their long axes locked to the external field. The trajectory of one colloidal dumbbell is colored according to the period of the precessing external field (see magnified inset). The flat channel is located exactly at the marked trajectory. (e) Overlay of microscope images of the rotating but not sliding motion above the inclined dithered twisted square pattern. The flat channel is marked as dark green dotted lines. (f) Overlay of microscope images of the non rotating and not sliding motion above the inclined dithered twisted hexagonal pattern. The flat channel is marked as dark green dotted lines. The color of the frames in (b)–(f) correspond to the colors of the transport mode in panel (a). Videos of the different transport modes are provided with the Videos S1–S10 (ESI†).

We cover the moiré pattern with photoresist of thickness t = 1 µm, that separates colloids from the magnetic thin film such that only long wave length Fourier modes (wave length of the order of the $\mathscr{P}$-tile lattice constant or more) of the pattern magnetic field is relevant at the location of our colloids. The moiré pattern is surrounded by five computer-controlled coils, four of which create an external in plane field and the other produces an external magnetic field normal to the pattern. The moiré pattern with the coils is mounted to a microscope operating in reflection mode. The microscope itself is mounted to a support with the optical axis along the pattern normal. The patter normal is inclined $\hat{\boldsymbol{g}}\cdot\boldsymbol{n} = -\cos(\beta)$ with respect to gravity with an inclination angle of $\beta = \pi/9$. Paramagnetic colloidal particles of diameter 4.51 µm (Dynabeads M-450) are immersed in a drop of water placed on the pattern.

We apply a time dependent external field

$$\boldsymbol{H}_{\text{ext}}(t) = \boldsymbol{R}(\omega t)\cdot\boldsymbol{H}_{\text{ext}}(0) \quad (2)$$

that rotates with angular frequency $\boldsymbol{\omega} = \omega\boldsymbol{n}$. Here $\omega = 1.5\ \text{s}^{-1}$, and $\boldsymbol{R}(\omega t)$ is a rotation matrix about the pattern normal $\boldsymbol{n}$ and the external field $\boldsymbol{H}_{\text{ext}}$ is tilted with an angle ϑ to the pattern normal ($\boldsymbol{H}_{\text{ext}}\cdot\boldsymbol{n} = \cos\vartheta$). The motion of the external field is thus a precession with angle ϑ around the moiré pattern normal.

Fig. 2 shows two dynamical phase diagrams of the motion above the inclined dithered twisted square and hexagonal patterns together with overlay of tracked video microscopy images of each mode of motion. We find five different transport modes.

The simplest mode occurs for low external magnetic field ($H_{\text{ext}} < 0.2$ kA m^{-1}) oriented close to the equatorial plane ($\vartheta > 50°$, blue triangles in Fig. 2a, microscopy images in Fig. 2b and Video S1 and S6, ESI†). The external field in this case precesses across the marginably stable points of the potential that will flatten the potential to valleys not only above the usual flat channels but also above the generic $\mathscr{P}$-tiles of the pattern. All colloidal particles, no matter where they are located, start to slide down the slope of the inclined plane under these circumstances. Based on the observation of multiple movies we see that in general the sliding direction of the colloidal particles in the flat channels follows an orientation of $\pm\pi/2n$ with respect to the inclination $(\mathbb{1} - \boldsymbol{nn})\cdot\boldsymbol{g}$ direction of the pattern if the particles are far away from the corners of the flat channels, but follow the inclination direction $(\mathbb{1} - \boldsymbol{nn})\cdot\boldsymbol{g}$ in the surroundings of the flat channel corners and in the generic $\mathscr{P}$-tiles. Colloidal dumbbells exhibit the same behavior. Additionally their long axis seems to correlate with the travel direction far away from the corners and seem to be less correlated while traveling in the corner surroundings.

In all other transport modes the external field will immobilize colloidal particles and dumbbells above the generic $\mathscr{P}$-tiles and the only remaining regions of mobility can be found above the flat channels or in the surroundings of the flat channel corners. At low external field, $H_{\text{ext}} < 0.2$ kA m^{-1}, and for precession angles $\vartheta < 50°$ dumbbells consisting of two colloidal particles slide through the flat channels with their long axis $\boldsymbol{d}$ oriented along the channel (bright green triangles in Fig. 2a and microscopy images in Fig. 2c as well as in Videos S2 and S7, ESI†). The trajectories follow the flat channel in the flat channel segments far from the corners, but they follow the in-plane gravity direction $(\mathbb{1} - \boldsymbol{nn})\cdot\boldsymbol{g}$ in the surroundings of the flat channel corners. The orientation of the dumbbell becomes random in the corner surroundings and switches to the new direction of the flat channels once the dumbbell reaches the next flat channel segment (see also Fig. 3a and b). We call this phase the slither sliding phase. Since the external field is weak under these circumstances, the anisotropic moiré pattern potential torque dominates over putative torques due to the external magnetic field.

The long axis of the dumbbells lock to the external field if we use stronger external magnetic fields ($H_{\text{ext}} > 0.2$ kA m^{-1}). For precession angles above $\vartheta > 10°$, the long axis of the dumbbell precesses synchronously with the external field (Fig. 3c and d). The potential generated by the pattern for large precession angles remains weak enough such that gravity drives the precessing dumbbells through the flat channels (dark green circles in Fig. 2a and microscopy images in Fig. 2d as well as in Videos S3 and S8, ESI†). We call this phase the rotating and sliding phase.

The sliding stops for precession angles below $\vartheta < 50°$ as shown in the phase diagrams in Fig. 2a as orange circles. A microscopy image is depicted for half a moiré Wigner Seitz cell of the square pattern in Fig. 2e. Videos S4 and S9 (ESI†) record this mode for both patterns.

For even smaller precession angles $\vartheta < 10°$ (red triangles in Fig. 2a) the dumbbells also stop precessing. A microscope image Fig. 2f of part of a hexagonal moiré Wigner Seitz cell shows the static behavior. Videos S5 and S10 (ESI†) show a short movie of the static mode for both patterns. Presumably

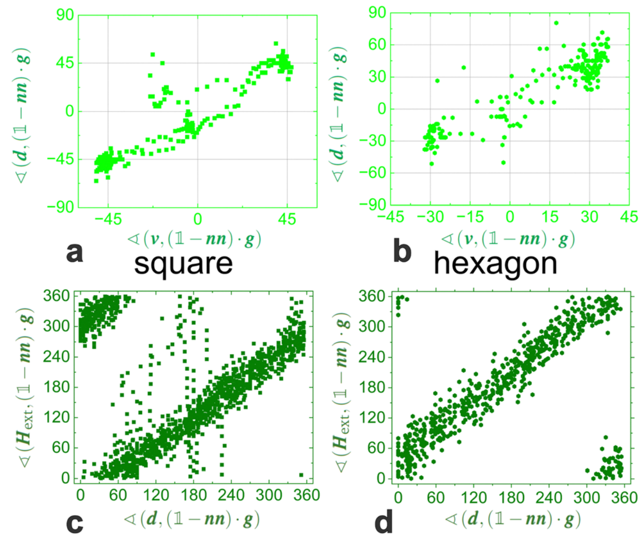

Fig. 3 Angle correlations (a) correlation between the velocity and director orientation in the slither sliding phase of the twisted square pattern. (b) Correlation between the velocity and director orientation in the slither sliding phase of the twisted hexagonal pattern. (c) Correlation between the director and external field orientation in the rotating and sliding phase of the twisted square pattern. (d) Correlation between the director and external field orientation in the rotating and sliding phase of the twisted hexagonal pattern.

the anisotropy in the colloidal potential dominates the behavior and suppresses any motion.

3. Discussion

In previous work[41] we have shown that magic non-generic transport behavior of colloids driven through a smooth twisted magnetic pattern occurs for magic angles due to the periodic nature of the corners of the flat channels. Under non-generic conditions each corner along a flat channel is different and in smooth magically twisted pattern one can avoid the occurrence of blockades at the corners. The transport on non-magically twisted patterns is predicted to stop at corners that block the transport. Smooth magically twisted systems therefore show pronounced non-generic transport behavior at the magic angles.

This is different for perturbed twisted systems: In intentionally heterostrained twisted bilayer graphene[56] the heterostrain can change the electronic flat bands. In experiments on a macroscopic scale we have shown[43] that disorder destroys the non-generic magic behavior such that the character of the transport is no longer decided at the corners but in the flat channel segments connecting the corners.

This is also true in the system studied here because the dithering, a specific form of disorder, of the twisted potential renders the flat channels rough. The roughness introduces obstacles that are harder to overcome and more frequent than those added under non-magical conditions at the corners. Therefore whether the potential is under non-generic twist angles or under magic conditions the transport behavior is decided inside the channels.

Single colloidal particles may travers potential barriers caused by the roughness of the potential inside the flat channels only for conditions that also mobilizes the single colloidal particles inside non-generic $\mathscr{P}$-tiles. Colloidal dumbbells carry double the weight and are long enough to pass over the roughness introduced by the dithering. This explains the slithering sliding of the dumbbells at small external field. Precession of the dumbbells under stronger external field introduces energetic fluctuations of the colloidal dumbbells that are strong enough to let the dumbbells pass over dithering obstacles. Hence the dumbbells perform a rotating sliding motion through the flat channels.

A smooth twisted colloidal potential could be produced by using two square or hexagonal patterns instead of the dithered single pattern. Colloidal particles would be placed between both patterns. However, it is difficult to visualize the colloids between both patterns.

4. Conclusions

In summary, twisted potentials are vulnerable to perturbations that usually destroys the non-generic magic behavior of the transport. However, other equally interesting transport modes that presumably persist whether the twist angle is magic or non-magic can be observed. Two distinct such modes: the slithering sliding and the rotating sliding have been characterized in this work.

Author contributions

FF, DdlH, & TMF designed and performed the experiment, and wrote the manuscript with input from all the other authors. NCXS computed the dithered patterns. PK, MU & FS produced the magnetic film. SA, & ArE performed the fabrication of the micromagnetic metamorphic patterns within the magnetic thin film.

Data availability

The data supporting this article have been included as part of the ESI.†

Conflicts of interest

There are no conflicts to declare.

Appendix

To achieve the observed phenomena we have to set the correct ratio of the relevant interactions. This is done the following way: The dipolar interaction between single colloidal particles scales with H_{ext}^2. We tried to work with external fields that produces singlets and dumbbells but not colloidal triplets, or quadruplets. Therefore we first chose an external field $H_{\text{ext}} < 1\ \text{kA m}^{-1}$. The interaction potential of the particles with the pattern is proportional to $\text{H}_\text{p}{}^2$ for small external field and proportional to $\boldsymbol{H}_{\text{ext}}{\cdot}\boldsymbol{H}_\text{p}$ for large external fields. The inclination angle β sets the driving force. There is a critical angle $\beta_\text{c}(H_{\text{ext}} = 1\ \text{kA m}^{-1}) \approx 30^\circ$. For $\beta > \beta_\text{c}$ the driving force is larger than the largest magnetic potential gradient such that the particles will start to slide in the generic positions of the moiré Wigner Seitz cell. We see that at large H_{ext} increasing β is similar to decreasing H_{ext}. If we do not consider the dithering roughness the phenomenon should only depend on the ratio $H_{\text{ext}}/\sin(\beta)$, however the dithering roughness makes things more complicated. We chose $\beta = 2/3\beta_\text{c}$ to obtain sliding in flat channels only. The frequency of rotation is such that the dumbbell can follow the external field when it is large but cannot follow when the external field is small. There is a non universal pattern potential that holds dumbbells oriented along a flat channel at vanishing or small external field. Reducing the precession frequency has no significant effect. There is a large cut off frequency where the response of the dumbbells is no longer synchronous to the field even without the magnetic pattern. We used frequencies well below this cutoff frequency.

Acknowledgements

T. M. F. and D. d. l. H. acknowledge funding by the Deutsche Forschungsgemeinschaft (DFG, German Research Foundation) under project number 531559581. P. K., M. U., and F. S. acknowledge financial support from the National Science Centre Poland through the OPUS funding (Grant No. 2019/33/B/ST5/02013). S. A. acknowledges funding by a PhD scholarship of Kassel university.

Notes and references

1 Y. Cao, V. Fatemi, A. Demir, S. Fang, S. L. Tomarken, J. Y. Luo, J. D. Sanchez-Yamagishi, K. Watanabe, T. Taniguchi, E. Kaxiras, R. C. Ashoori and P. Jarillo-Herrero, *Nature*, 2018, **556**, 80–84.
2 R. Bistritzer and A. H. MacDonald, *Proc. Natl. Acad. Sci. U. S. A.*, 2011, **108**, 12233–12237.
3 K. P. Nuckolls, M. Oh, D. Wong, B. Lian, K. Watanabe, T. Taniguchi, B. A. Bernevig and A. Yazdani, *Nature*, 2020, **588**, 610–615.
4 E. Suárez Morell, J. D. Correa, P. Vargas, M. Pacheco and Z. Barticevic, *Phys. Rev. B: Condens. Matter Mater. Phys.*, 2010, **82**, 121407.
5 S. Carr, D. Massatt, S. Fang, P. Cazeaux, M. Luskin and E. Kaxiras, *Phys. Rev. B: Condens. Matter Mater. Phys.*, 2017, **95**, 075420.
6 J. M. B. Lopes dos Santos, N. M. R. Peres and A. H. Castro Neto, *Phys. Rev. Lett.*, 2007, **99**, 256802.
7 C. Shen, Y. Chu, Q. Wu, N. Li, S. Wang, Y. Zhao, J. Tang, J. Liu, J. Tian, K. Watanabe, T. Taniguchi, R. Yang, Z. Y. Meng, D. Shi, O. V. Yazyev and G. Zhang, *Nat. Phys.*, 2020, **16**, 520–525.
8 K. Liu, L. Zhang, T. Cao, C. Jin, D. Qiu, Q. Zhou, A. Zettl, P. Yang, S. G. Louie and F. Wang, *Nat. Commun.*, 2014, **5**, 4966.
9 H. Isobe, N. F. Q. Yuan and L. Fu, *Phys. Rev. X*, 2018, **8**, 041041.
10 L. Balents, C. R. Dean, D. K. Efetov and A. F. Young, *Nat. Phys.*, 2020, **16**, 725–733.
11 Y. Saito, J. Ge, K. Watanabe, T. Taniguchi and A. F. Young, *Nat. Phys.*, 2020, **16**, 926–930.
12 L. H. C. M. Nunes and C. M. Smith, *Phys. Rev. B*, 2020, **101**, 224514.
13 P. Stepanov, I. Das, X. Lu, A. Fahimniya, K. Watanabe, T. Taniguchi, F. H. L. Koppens, J. Lischner, L. Levitov and D. K. Efetov, *Nature*, 2020, **583**, 375–378.
14 Y. Cao, V. Fatemi, S. Fang, K. Watanabe, T. Taniguchi, E. Kaxiras and P. Jarillo-Herrero, *Nature*, 2018, **556**, 43–50.
15 M. Yankowitz, S. Chen, H. Polshyn, Y. Zhang, K. Watanabe, T. Taniguchi, D. Graf, A. F. Young and C. R. Dean, *Science*, 2019, **363**, 1059–1064.
16 A. L. Sharpe, E. J. Fox, A. W. Barnard, J. Finney, K. Watanabe, T. Taniguchi, M. A. Kastner and D. Goldhaber-Gordon, *Science*, 2019, **365**, 605–608.
17 X. Lu, P. Stepanov, W. Yang, M. Xie, M. A. Aamir, I. Das, C. Urgell, K. Watanabe, T. Taniguchi, G. Zhang, A. Bachtold, A. H. MacDonald and D. K. Efetov, *Nature*, 2019, **574**, 653–657.
18 Y. Zhao, M. A. Belkin and A. Alù, *Nat. Commun.*, 2012, **3**, 870.
19 S. S. Sunku, G. X. Ni, B. Y. Jiang, H. Yoo, A. Sternbach, A. S. McLeod, T. Stauber, L. Xiong, T. Taniguchi, K. Watanabe, P. Kim, M. M. Fogler and D. N. Basov, *Science*, 2018, **362**, 1153–1156.
20 G. Hu, Q. Ou, G. Si, Y. Wu, J. Wu, Z. Dai, A. Krasnok, Y. Mazor, Q. Zhang, Q. Bao, C.-W. Qiu and A. Alù, *Nature*, 2020, **582**, 209–213.
21 P. Wang, Y. Zheng, X. Chen, C. Huang, Y. V. Kartashov, L. Torner, V. V. Konotop and F. Ye, *Nature*, 2020, **577**, 42–46.
22 G. Hu, C.-W. Qiu and A. Alù, *Opt. Mater. Express*, 2021, **11**, 1377–1382.
23 A. I. Cocemasov, D. L. Nika and A. A. Balandin, *Phys. Rev. B: Condens. Matter Mater. Phys.*, 2013, **88**, 035428.
24 G. Ma, M. Xiao and C. T. Chan, *Nat. Rev. Phys.*, 2019, **1**, 281–294.
25 S. M. Gardezi, H. Pirie, S. Carr, W. Dorrell and J. E. Hoffman, *2d Matter.*, 2021, **8**, 031002.
26 Y. Deng, M. Oudich, N. J. Gerard, J. Ji, M. Lu and Y. Jing, *Phys. Rev. B*, 2020, **102**, 180304.
27 D. Yao, L. Ye, Z. Fu, Q. Wang, H. He, J. Lu, W. Deng, X. Huang, M. Ke and Z. Liu, *Phys. Rev. Lett.*, 2024, **132**, 266602.
28 W. Li, C. J. O. Reichhardt, B. Jankó and C. Reichhardt, *Phys. Rev. B*, 2021, **104**, 024504.
29 A. M. E. B. Rossi, J. Bugase and T. M. Fischer, *Europhys. Lett.*, 2017, **119**, 40001.
30 A. M. E. B. Rossi, J. Bugase, T. Lachner, A. Ernst, D. de las Heras and T. M. Fischer, *Soft Matter*, 2019, **15**, 8543–8551.
31 J. Loehr, M. Loenne, A. Ernst, D. de las Heras and T. M. Fischer, *Nat. Commun.*, 2016, **7**, 11745.
32 D. de las Heras, J. Loehr, M. Loenne and T. M. Fischer, *New J. Phys.*, 2016, **18**, 105009.
33 J. Loehr, D. de las Heras, M. Loenne, J. Bugase, A. Jarosz, M. Urbaniak, F. Stobiecki, A. Tomita, R. Huhnstock, I. Koch, A. Ehresmann, D. Holzinger and T. M. Fischer, *Soft Matter*, 2017, **13**, 5044–5075.
34 J. Loehr, D. de las Heras, A. Jarosz, M. Urbaniak, F. Stobiecki, A. Tomita, R. Huhnstock, I. Koch, A. Ehresmann, D. Holzinger and T. M. Fischer, *Commun. Phys*, 2018, **1**, 4.
35 H. Massana-Cid, A. Ernst, D. de las Heras, A. Jarosz, M. Urbaniak, F. Stobiecki, A. Tomita, R. Huhnstock, I. Koch, A. Ehresmann, D. Holzinger and T. M. Fischer, *Soft Matter*, 2019, **15**, 1539–1550.
36 M. Mirzaee-Kakhki, A. Ernst, D. de las Heras, M. Urbaniak, F. Stobiecki, J. Gördes, M. Reginka, A. Ehresmann and T. M. Fischer, *Nat. Commun.*, 2020, **11**, 4670.
37 M. Mirzaee-Kakhki, A. Ernst, D. de las Heras, M. Urbaniak, F. Stobiecki, A. Tomita, R. Huhnstock, I. Koch, J. Gördes, A. Ehresmann, D. Holzinger, M. Reginka and T. M. Fischer, *Soft Matter*, 2020, **16**, 1594–1598.
38 M. Mirzaee-Kakhki, A. Ernst, D. de las Heras, M. Urbaniak, F. Stobiecki, A. Tomita, R. Huhnstock, I. Koch, A. Ehresmann, D. Holzinger and T. M. Fischer, *Soft Matter*, 2021, **17**, 1663–1674.

39 N. C. X. Stuhlmüller, F. Farrokhzad, P. Kuświk, F. Stobiecki, M. Urbaniak, S. Akhundzada, A. Ehresmann, T. M. Fischer and D. de las Heras, *Nat. Commun.*, 2023, **14**, 7517.

40 J. Elschner, F. Farrokhzad, P. Kuswik, M. Urbaniak, F. Stobiecki, S. Akhundzada, A. Ehresmann, D. de las Heras and T. M. Fischer, *Nat. Commun.*, 2024, **15**, 5735.

41 N. C. X. Stuhlmüller, T. M. Fischer and D. de las Heras, *Commun. Phys.*, 2022, **5**, 48.

42 N. C. X. Stuhlmüller, T. M. Fischer and D. de las Heras, *New J. Phys.*, 2024, **26**, 023056.

43 A. M. E. B. Rossi, A. Ernst, M. Dörfler and T. M. Fischer, *Commun. Phys.*, 2024, **7**, 24.

44 G. Costantini and F. Marchesoni, *EPL*, 1999, **48**, 491.

45 M. Tinkham, J. U. Free, C. N. Lau and N. Markovic, *Phys. Rev. B: Condens. Matter Mater. Phys.*, 2003, **68**, 134515.

46 C. Guarcello, D. Valenti, A. Carollo and B. Spagnolo, *J. Stat. Mech.: Theor. Exp*, 2016, 054012.

47 S. A. Tatarkova, W. Sibbett and K. Dholakia, *Phys. Rev. Lett.*, 2003, **91**, 038101.

48 K. Lindenberg, J. M. Sancho, A. M. Lacasta and I. M. Sokolov, *Phys. Rev. Lett.*, 2007, **98**, 020602.

49 P. Siegle, I. Goychuk and P. Hänggi, *Phys. Rev. Lett.*, 2010, **105**, 100602.

50 C. Reichhardt and C. J. O. Reichhardt, *Phys. Rev. B: Condens. Matter Mater. Phys.*, 2015, **92**, 224432.

51 M. Urbaniak, P. Kuświk, Z. Kurant, M. Tekielak, D. Engel, D. Lengemann, B. Szymański, M. Schmidt, J. Aleksiejew, A. Maziewski, A. Ehresmann and F. Stobiecki, *Phys. Rev. Lett.*, 2010, **105**, 067202.

52 P. Kuświk, A. Ehresmann, M. Tekielak, B. Szymański, I. Sveklo, P. Mazalski, D. Engel, J. Kisielewski, D. Lengemann, M. Urbaniak, C. Schmidt, A. Maziewski and F. Stobiecki, *Nanotechnology*, 2011, **22**, 095302.

53 D. Lengemann, D. Engel and A. Ehresmann, *Rev. Sci. Instrum.*, 2012, **83**, 053303.

54 F. J. Maier, T. Lachner, A. Vilfan, T. O. Tasci, K. B. Neeves, D. W. M. Marr and T. M. Fischer, *Soft Matter*, 2016, **12**, 9314–9320.

55 S. Barthmann and T. M. Fischer, *J. Phys. Commun.*, 2021, **5**, 085003.

56 F. Mesple, A. Missaoui, T. Cea, L. Huder, F. Guinea, G. Trambly de Laissardière, C. Chapelier and V. T. Renard, *Phys. Rev. Lett.*, 2021, **127**, 126405.

Part III

Methods

Chapter 5

Materials and methods

My passion was always to see the theories on paper, in the real world and experiments. It is wonderful to watch your efforts pay off (Hopefully in every aspect of your life!). I used two different setups for my two different projects. One can be tilted, and one is stable. In this chapter I will show which setups I built and used for the experiments, and I will explain the main structure of these setups.

5.1 Setup

I use a polarization microscope from Leica with a camera attached on top of the microscope. To visualize the experiments with the colloidal particles, it is connected to the commercial software StreamPix that can record the experiment. To generate the external magnetic fields five coils are placed on top of the slide table. Two of these generate the $x-$, two of them the $y-$ and one of them the $z-$ component of $\boldsymbol{H}_{ext}(t)$. The coils are connected to three bi-polar amplifiers , which are fed by a programmable wave generator each.

By designing a desired loop in a Matlab program and transferring its $x-$, $y-$ and $z-$ components to the three wave generators, loops with arbitrary waveforms can be generated. To have homogeneous magnetic fields, the magnetic patterns were placed directly on top of the $z-$coil, exactly in centre of the axes of the coils.

For the experiment I used a drop of colloidal suspension on top of lithographic magnetic patterns. I use a magnetic Co/Au multilayer, which has been patterned by keV $He+$- ion bombardment through a lithographical mask in a home-built bombardment stage. To have a universal pattern field, I coated our pattern by the spin coating method with a photo resist layer of the thickness 1μm. I was using spin coating at a speed of 3000 rpm for 150 s. After the spin coating, the resist was baked for 1 min at $115°C$ on a heat-plate. For more persistence of the photo resistant layer, I put it in the oven for about 2 hours under $170°$C, it can be called a soft baking process.

5.1.1 Setup 1: fixed setup

In Fig 5.1 I show the heart of the setup 1. As you can see the coils are fixed to a plate and the microscope is also fixed to the table. I used this setup for the experiments in my first and second publications, for experiments where neither the pattern nor the coils need to be rotated and where there was no inclination of the pattern with respect to gravity. In this setup, the polarization microscope $DM2500P$ from Leica, streampix 5.0 with a resolution of 1392×1040 at 20 frames per second, amplifiers (Kepco BOP $20-50$GL), wave generator (Aim-TTi TGA 1244) are used.

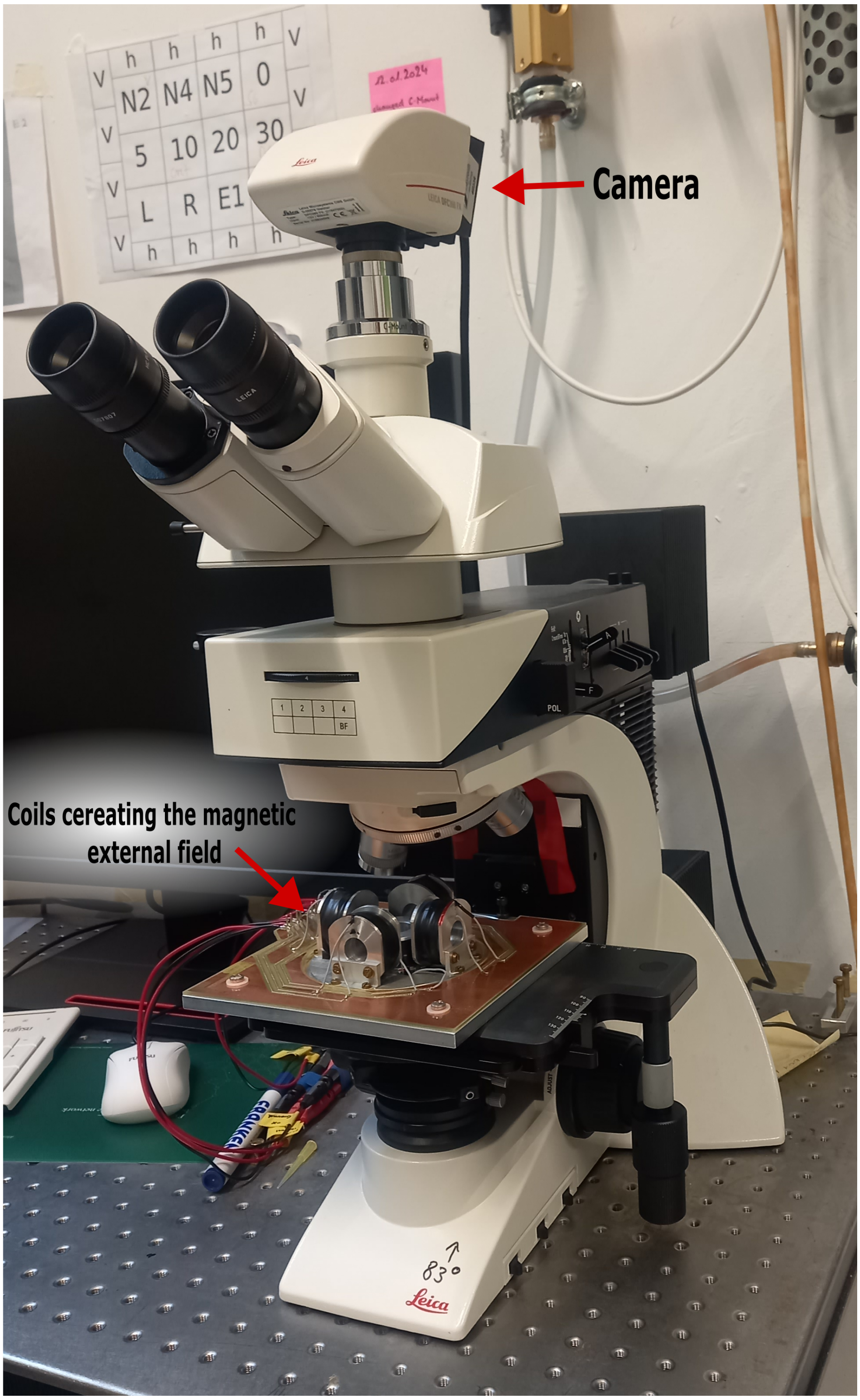

Figure 5.1: Picture of the fixed setup.

5.1.2 Setup 2: rotating stage setup

Setup 2 is shown in Fig. 5.2b. In publication 1, for my experiments for writing letters, I needed to be able to rotate the pattern relative to the coils by specific angles. Therefore, I designed a sample holder shown in Fig. 5.2a consisting of two separate plates that both can be rotated. On one plate I mount the coils the second plate supports the pattern. In this way I can rotate the coils and the pattern independently. As presented in Fig. 5.2a, it is possible to arrest each of these plates. In publication 3, for my project with the twisted patterns, I needed to apply some driving force to particles. The best way to do that in my experiments was by using gravity force. Therefore, I designed the setup (shown in Fig. 5.2c) such that the entire setup can be inclined by rotating a crank handle. In this way, the pattern will be also inclined and the particles can feel a driving force. In this setup, the polarization microscope $DM2500MH$ from Leica, streampix 9.0 with a resolution of $2048{\times}1538$ at 30 frames per second, amplifiers (Kepco BOP $20-50GL$), wave generator (Aim-TTi TGA 1244) are used.

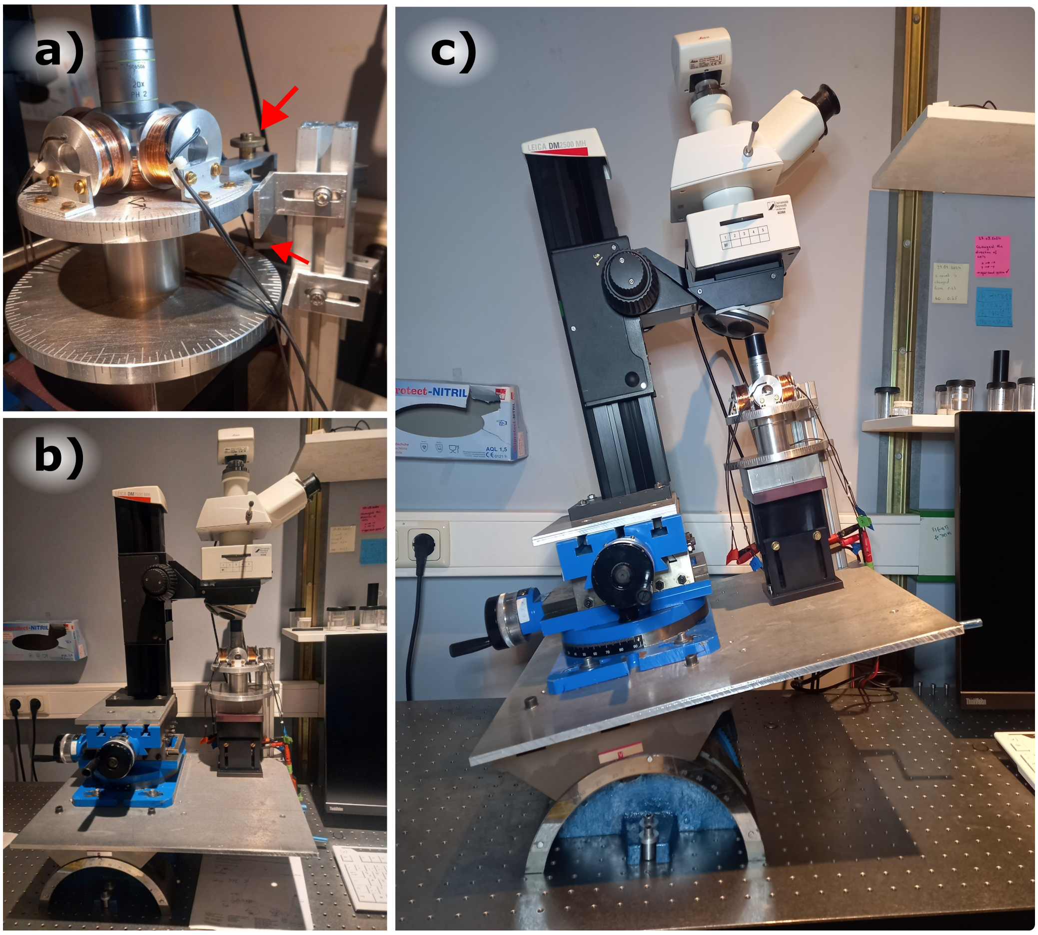

Figure 5.2: Picture of the Rotating stage setup. a) The sample holder with the two rotating stages one holding the coils and one holding the magnetic pattern. The red arrows show the places where each of the plates can be arrested. b) The non-inclined microscope with the sample holder c) The inclined micrsocope with the sample holder.

Part IV

Summary

Summary and outlook

In this cumulative thesis I studied the topological and drift transport of colloidal particles on top of non-periodic patterns. The colloids are placed above a non-periodic magnetic pattern of alternating domains with up and down magnetization. I can apply a homogeneous external magnetic field following a time sequence (a loop) of arbitrary field orientations. The sphere of all possible external field directions is called control space. The control space has special points named bifurcation points, where one stationary point on the pattern bifurcates into three or more stationary points on the pattern. The positions of these points depend on the symmetry of the pattern and the geometric properties of the particles. The control space is punctured in these points and by applying magnetic loops that wind around these points I will have topologically non-trivial protected transport.

In my first publication 1 I used a non-periodic topological locally three fold symmetric defect pattern having a symmetry phase that varies with the location on the pattern. Therefore, the position of bifurcation points in control space for each different symmetry phase of the pattern is different. In this case by designing a loop that winds around different bifurcation points simultaneously, I am able to control the motion of identical single colloidal particles at different locations on the pattern independently. By applying an external magnetic field single paramagnetic colloidal particles can be self assembled due to dipolar interactions and make bipeds with different length. The direction of the biped is locked to the direction of the external magnetic field. Here I introduce another space, transcription space, for bipeds. It is the vector space of the biped end to end vectors which can be decomposed into concentric spheres of the radius of the biped length. For each biped length the control loop in control space is transcribed into a loop onto the appropriate sphere in transcription space. The transcribed bifurcation points then collapse onto bifurcation lines that cuts the spheres of different biped radius in different locations. The winding numbers in transcription space around the bifurcation lines depend on the biped length. Therefore bipeds with different length fall into different homotopy classes and by designing a proper loop I can transport bipeds with different length independently.

In my second publication 2, I used a metamorphic pattern to control the motion of colloidal particles locally. I applied a single magnetic loop to the system and each single colloidal particle or bipeds interpret the loop differently if either their positions on the pattern or their biped length differs. I designed the loop in control space to let single colloidal particles move toward an active line from two sides of the active line to assemble to bipeds in the active zone and when they reach the preprogrammed length of my control loop, they walk away from the active zone. The synthesis is a self healing process and by applying an external loop any mistakes occurring during the synthesis is fixed by the bipeds without the need of external interference.

Finally, I studied the drift transport of the colloidal particles on top of twisted periodic square and hexagonal patterns. In my third publication 3 I investigated how the singlets and dumbbells are transported on top of a dithered moiré pattern. Singlets and dumbbells experience a drift force and are subject to a precessing external magnetic field. I vary the precession angle of the external field and the strength of the magnetic field. Due to the dithering of the moiré patterns the colloidal potential is rough inside flat channels and I found different dynamic phase behaviour of the particles depending on the strength of the field and the precession angle of the external magnetic field. I discovered two different modes in the flat channels: the slithering sliding and the rotating sliding. I call slithering sliding transport when dumbbells slither along the flat channels with its head always pointing in direction of the channel direction. The slithering sliding phase happens at small external field because the channel torque exceeds the torque from the magnetic field and dumbbells carry double the weight of a single colloidal particle and they can pass over the dither roughness of the flat channels. In the rotating sliding, dumbbells synchronously rotate with the external field and they slide simultaneously through the flat channels. The rotation can introduce energetic fluctuations and therefore the dumbbells will be able to overcome the dither roughness fluctuations. Hence they perform a rotating sliding motion through the flat channels.

I believe there are still some useful phenomena in this field to be discovered. One would use the method that I showed in my second paper to sort different length of bipeds in a desired locations. In addition, here I used only paramagnetic particles to have bipeds. By using a mixture of para- and diamagnetic particles, we would have more complicated shapes and the variety of the topological transport can be increased.

Bibliography

1. B. J. Skinner. in *Handbook of Physical Constants* 75–96 (1966).
2. J. Rychlewski. On Hooke's law. *Journal of Applied Mathematics and Mechanics* **48**, 303–314 (1984).
3. A. T. Fomenko and D. B. Fuks. *Homotopical Topology* (Springer, 2016).
4. A. Murugan and S. Vaikuntanathan. Topologically protected modes in non-equilibrium stochastic systems. *Nature Communications* **8**, 13881 (2017).
5. K. v. Klitzing, G. Dorda and M. Pepper. New method for high-accuracy determination of the fine-structure constant based on quantized Hall resistance. *Physical Review Letters* **45**, 494 (1980).
6. S.-Q. Shen. *Topological Insulators* (Springer, 2012).
7. V. Guillemin and A. Pollack. *Differential Topology. Englewood Cliffs, New Jersey: Prentice Hall* 1974.
8. M. Nakahara. *Geometry, Topology and Physics* (CRC press, 2018).
9. L. Fu. Topological crystalline insulators. *Physical Review Letters* **106**, 106802 (2011).
10. R. Carbó-Dorca and E. Besalú. Geometry of n-dimensional Euclidean space Gaussian enfoldments. *Journal of Mathematical Chemistry* **49**, 2244–2249 (2011).
11. S.-Y. A. Chang and P. C. Yang. Prescribing Gaussian curvature on S2 (1987).
12. G. Beltramo, R. Andreeva, Y. Giarratano, M. O. Bernabeu, R. Sarkar *et al.* Euler characteristic surfaces. *ArXiv Preprint ArXiv:2102.08260* (2021).
13. S. Kalyanswamy. Euler Characteristic. *Math 4530 Introduction to Topology, Essay. Cornell University, Ithaca* (2009).
14. F. E. P. Hirzebruch and M. Kreck. On the concept of genus in topology and complex analysis. *Notices of the American Mathematical Society* **56**, 713–719 (2009).
15. H. I. Levine. Homotopic curves on surfaces. *Proceedings of the American Mathematical Society* **14**, 986–990 (1963).
16. Y. Ren, Z. Qiao and Q. Niu. Topological phases in two-dimensional materials: a review. *Reports on Progress in Physics* **79**, 066501 (2016).

17. P. W. Shor. *Algorithms for quantum computation: discrete logarithms and factoring* in *Proceedings 35th Annual Aymposium on Foundations of Computer Science* (1994), 124–134.
18. A. Y. Kitaev. Fault-tolerant quantum computation by anyons. *Annals of Physics* **303**, 2–30 (2003).
19. M. Z. Hasan and C. L. Kane. Colloquium: topological insulators. *Reviews of Modern Physics* **82**, 3045–3067 (2010).
20. S. D. Huber. Topological mechanics. *Nature Physics* **12**, 621–623 (2016).
21. M. den Nijs. Quantized Hall conductance in a two dimensional periodic potential. *Physica A: Statistical Mechanics and its Applications* **124**, 199–210 (1984).
22. E. Orlandini and C. Micheletti. Topological and physical links in soft matter systems. *Journal of Physics: Condensed Matter* **34**, 013002 (2021).
23. J. Loehr, M. Loenne, A. Ernst, D. de Las Heras and T. M. Fischer. Topological protection of multiparticle dissipative transport. *Nature Communications* **7**, 11745 (2016).
24. J. Loehr, D. de Las Heras, M. Loenne, J. Bugase, A. Jarosz *et al.* Lattice symmetries and the topologically protected transport of colloidal particles. *Soft Matter* **13**, 5044–5075 (2017).
25. M. Urbaniak, P. Kuświk, Z. Kurant, M. Tekielak, D. Engel *et al.* Domain-wall movement control in Co/Au multilayers by He+-ion-bombardment-induced lateral coercivity gradients. *Physical Review Letters* **105**, 067202 (2010).
26. P. Kuświk, A. Ehresmann, M. Tekielak, B. Szymański, I. Sveklo *et al.* Colloidal domain lithography for regularly arranged artificial magnetic out-of-plane monodomains in Au/Co/Au layers. *Nanotechnology* **22**, 095302 (2011).
27. D. de las Heras, J. Loehr, M. Loenne and T. M. Fischer. Topologically protected colloidal transport above a square magnetic lattice. *New Journal of Physics* **18**, 105009 (2016).
28. M. Mirzaee-Kakhki, A. Ernst, D. de Las Heras, M. Urbaniak, F. Stobiecki *et al.* Simultaneous polydirectional transport of colloidal bipeds. *Nature Communications* **11**, 4670 (2020).
29. G. Fonnum, C. Johansson, A. Molteberg, S. Mørup and E. Aksnes. Characterisation of Dynabeads® by magnetization measurements and Mössbauer spectroscopy. *Journal of Magnetism and Magnetic Materials* **293**, 41–47 (2005).

30. A. Jarosz, D. Holzinger, M. Urbaniak, A. Ehresmann and F. Stobiecki. Manipulation of superparamagnetic beads on patterned Au/Co/Au multilayers with perpendicular magnetic anisotropy. *Journal of Applied Physics* **120** (2016).

31. R. McGorty, J. Fung, D. Kaz and V. N. Manoharan. Colloidal self-assembly at an interface. *Materials Today* **13**, 34–42 (2010).

32. M. Mirzaee-Kakhki, A. Ernst, D. de Las Heras, M. Urbaniak, F. Stobiecki *et al.* Gauge invariant and gauge dependent aspects of topological walking colloidal bipeds. *Soft Matter* **17**, 1663–1674 (2021).

33. T. A. Nieminen, G. Knöner, N. R. Heckenberg and H. Rubinsztein-Dunlop. Physics of optical tweezers. *Methods in Cell Biology* **82**, 207–236 (2007).

34. D. G. Grier. Optical tweezers in colloid and interface science. *Current Opinion in Colloid & Interface Science* **2**, 264–270 (1997).

35. E. Babichev. Global topological k-defects. *Physical Review D—Particles, Fields, Gravitation, and Cosmology* **74**, 085004 (2006).

36. J. C. Teo and T. L. Hughes. Topological defects in symmetry-protected topological phases. *Annual Review of Condensed Matter Physics* **8**, 211–237 (2017).

37. N. C. Stuhlmüller, F. Farrokhzad, P. Kuświk, F. Stobiecki, M. Urbaniak *et al.* Simultaneous and independent topological control of identical microparticles in non-periodic energy landscapes. *Nature Communications* **14**, 7517 (2023).

38. D. Levine and P. J. Steinhardt. Quasicrystals. I. Definition and structure. *Physical Review B* **34**, 596 (1986).

39. J. Elschner, F. Farrokhzad, P. Kuświk, M. Urbaniak, F. Stobiecki *et al.* Topologically controlled synthesis of active colloidal bipeds. *Nature Communications* **15**, 5735 (2024).

40. A. Nimbalkar and H. Kim. Opportunities and challenges in twisted bilayer graphene: a review. *Nano-Micro Letters* **12**, 1–20 (2020).

41. R. Bistritzer and A. H. MacDonald. Moiré bands in twisted double-layer graphene. *Proceedings of the National Academy of Sciences* **108**, 12233–12237 (2011).

42. S. Lisi, X. Lu, T. Benschop, T. A. de Jong, P. Stepanov *et al.* Observation of flat bands in twisted bilayer graphene. *Nature Physics* **17**, 189–193 (2021).

43. M. Yankowitz, S. Chen, H. Polshyn, Y. Zhang, K. Watanabe *et al.* Tuning superconductivity in twisted bilayer graphene. *Science* **363**, 1059–1064 (2019).

44. N. C. Stuhlmüller, T. M. Fischer and D. de Las Heras. Colloidal transport in twisted lattices of optical tweezers. *Physical Review E* **106**, 034601 (2022).

45. N. C. Stuhlmüller, T. M. Fischer and D. de las Heras. Enhanced colloidal transport in twisted magnetic patterns. *Communications Physics* **5**, 48 (2022).

46. A. M. Rossi, A. Ernst, M. Dörfler and T. M. Fischer. Disorder scattering in classical flat channel transport of particles between twisted magnetic square patterns. *Communications Physics* **7**, 24 (2024).

47. F. Farrokhzad, N. C. Stuhlmüller, P. Kuswik, M. Urbaniak, F. Stobiecki *et al.* Magnetic colloidal single particles and dumbbells on a tilted washboard moir'e pattern in a precessing external field. *Soft Matter* (2024).

Eidesstattliche Versicherung

Hiermit versichere ich an Eides statt, dass ich die vorliegende Arbeit selbstständig verfasst und keine anderen als die von mir angegebenen Quellen und Hilfsmittel verwendet habe.

Weiterhin erkläre ich, dass ich die Hilfe von gewerblichen Promotionsberatern bzw. -vermittlern oder ähnlichen Dienstleistern weder bisher in Anspruch genommen habe, noch künftig in Anspruch nehmen werde.

Zusätzlich erkläre ich hiermit, dass ich keinerlei frühere Promotionsversuche unternommen habe.

Bayreuth, den 17. November 2024

Farzaneh Farrokhzad